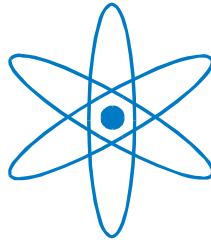PHYSIK–DEPARTMENT

Development of Methods for Scatter Artifact Correction in Industrial X-ray Cone-beam Computed Tomography

Dissertation
von

Karsten Schörner

TECHNISCHE UNIVERSITÄT

MÜNCHEN

TLM

TECHNISCHE UNIVERSITÄT MÜNCHEN
Physik Department E21 (Lehrstuhl für Experimentalphysik III)

Development of Methods for Scatter Artifact Correction in Industrial X-ray Cone-beam Computed Tomography

Dipl.-Phys. Univ. Karsten Schörner

Vollständiger Abdruck der von der Fakultät für Physik der Technischen Universität München zur Erlangung des akademischen Grades eines

Doktors der Naturwissenschaften (Dr. rer. nat.)

genehmigten Dissertation.

Vorsitzender: Univ.-Prof. Dr. Martin Zacharias

Prüfer der Dissertation: 1. Univ.-Prof. Dr. Peter Böni
                           2. Univ.-Prof. Dr. Franz Pfeiffer

Die Dissertation wurde am 29.02.2012 bei der Technischen Universität München eingereicht und durch die Fakultät für Physik am 04.05.2012 angenommen.

Meinen Eltern gewidmet.

Abstract

Scattered radiation represents a major source of image degradation in industrial X-ray cone-beam computed tomography (CBCT) leading to the formation of scatter artifacts in the reconstructed volume. These artifacts include cupping artifacts, streaks between high-contrast details, and a general loss of contrast. They hamper qualitative and quantitative analysis in industrial nondestructive inspection tasks: Reduced contrast decreases detectability of flaws such as cracks and voids while the cupping artifact as well as streaks affect dimensional measurements. This motivates the correction of scatter artifacts in industrial CBCT.

In this work, we investigate two novel experimental methods for *a-posteriori* correction of scatter artifacts in CBCT: first the beam-hole array technique, and second a different approach that is based on temporal primary modulation.

The beam-hole array technique is considered as complementary in experimental practice to the better-known beam-stop array technique: The beam-hole array is manufactured as a sheet of a highly absorbing material such as lead with small apertures for measuring primary signals at a number of sampling points in a first scan. In a second scan without beam-hole array, for each pixel, the total signal is measured. Pixel-wise subtraction of the primary signal from the total signal yields scatter estimates at the sampling points. Subsequently, spline interpolation is used in order to compute entire scatter images which are subtracted from original CT projections.

Comparison measurements between the new beam-hole array and the more established beam-stop array technique generally show good agreement of both techniques. However, they also indicate that with the beam-stop array technique, scatter-to-total ratios are constantly larger by 1-2%-points at object-covered sampling points. This is due to scattered radiation from a support plate which is only to be used in the beam-stop array technique. From this point of view, the beam-hole array is particularly suited for series CT scans whereby scattered radiation, and hence noise can be reduced.

We successfully demonstrate scatter correction by the beam-hole array technique applied to the CT of an industrial, ceramic specimen. In this application, scatter artifacts can be eliminated in certain regions within the reconstructed volume. Furthermore, in contrast to the common assumption that the scatter distribution is of low spatial frequency content, we observe high spatial frequencies contained within the calculated scatter images. We attribute this observation to a strong scatter contribution from detector-internal X-ray scatter and light spread effects. From basic experimental investigations, we deduce that these effects amount to one fifth of the total measured signal in a typical CT situation (220 kVp polychromatic X-ray spectrum).

Scatter correction by temporal primary modulation is the second method which we have developed and experimentally studied. This method offers two important advantages over

other techniques: First, it can be performed without additional scan time, and second, it offers high spatial resolution for sampling scatter data. From a theoretical point of view, the resolution is only limited by the detector.

For scatter estimation, the primary fluence is temporally amplitude-modulated in small pixel clusters which are phase-shifted to each other whereas the total scatter distribution virtually remains constant. This enables a separation of modulated primary signals and unmodulated scatter signals by coherent demodulation afterwards. The assumption of a virtually constant scatter distribution is supported by Monte-Carlo simulations and requirements concerning the spatial modulation pattern are derived in a theoretical analysis.

For modulation of the primary fluence, we use a so-called primary modulator, a spatially repetitive attenuation pattern in front of the object which imprints its pattern on the primary fluence. Temporal modulation is realized by moving the attenuation pattern and recording a number of modulated projections. In our experimental investigations, we employ a checkerboard pattern with 99×99 squares as primary modulator which is shifted or slided, respectively, by one square length within two modulated projections. The proposed method of temporal primary modulation is verified in a comparison measurement with the standard beam-stop array technique. Scatter estimates from both methods are generally in good agreement, i.e. deviations are less than 6% at direct sampling points of the beam-stop array.

Additionally, we demonstrate the application of the proposed method for the correction of scatter artifacts within a single CT scan of an aluminum test phantom. For this scan including scatter correction, no additional scan time is necessary and the scatter images are sampled at 95×95 points within the region of interest. Scatter artifacts are greatly suppressed and almost eliminated compared to a normal CT scan without scatter correction. For example, the contrast of specific slits cut in the test phantom is enhanced whereby deviations of contrast values to ideal contrast values of a simulated CT decrease from about 35% to 10% and less. Furthermore, the cupping artifact is completely removed, i.e. line profiles in the corrected CT slices show an almost perfect rectangular shape.

In summary, we present two novel experimental methods for scatter correction in CBCT whereby scatter artifacts can be greatly suppressed. Particularly, temporal primary modulation has been shown to be a favorable method for scatter correction since it offers high spatial resolution and does not extend scan times.

List of Abbreviations

BHA	Beam-Hole Array
BHC	Beam-Hardening Correction
BHD	Beam-Hardening
BSA	Beam-Stop Array
CBCT	Cone-Beam Computed Tomography
CFRP	Carbon-Fiber-Reinforced Polymer
CT	Computed Tomography
FBP	Filtered Back-Projection (reconstruction algorithm)
FDK	FBP algorithm by Feldkamp, Davis and Kress for 3D cone beam CT
FPD	Flat-Panel Detector
MC	Monte-Carlo (simulation)
NDT	Nondestructive Testing
PSF	Point-Spread Function
ROI	Region Of Interest
SDD	Source-to-Detector Distance
SNR	Signal-to-Noise Ratio
SOD	Source-to-Object Distance
SPM	Spatial Primary Modulation (scatter correction method)
SPR	Scatter-to-Primary Ratio
SSS	Single Scatter Sources
STR	Scatter-to-Total Ratio
TFT	Thin-Film Transistor
TPM	Temporal Primary Modulation (scatter correction method)

Contents

Chapter 1

Introduction

Over the last two decades, X-ray cone-beam computed tomography (CBCT) has become a well-established technique in nondestructive testing (NDT) for the precise visualization of both external and internal structures of a test component. CBCT enables true, isotropic 3D inspection of an object with a spatial resolution down to $1\,\mu\text{m}$ and less. Therefore, it is used in many different fields in industry for defect detection, failure analysis, as well as for dimensional measurements (metrology). Applications include the testing of industrial components, ranging from small parts such as electronic devices to rather big parts such as massive components of gas turbines.

In modern CBCT scanners, digital flat-panel detectors (FPD) are widely used. They provide instantaneous and complete 2D image data acquisition. Developed in the late 1990s, they represent a technological breakthrough in the history of both medical and industrial CT. Looking at the development of medical CT systems starting with pencil-beams and further evolving to scanners with fan-beam geometry, the step to cone-beam geometry represented the next consequent extension. The driving force for that development is the more efficient exploitation of X-rays produced by the X-ray tube. Since pencil-beam and fan-beam scanners use pin-hole and slit collimators, respectively, for reshaping the original beam, they are less efficient in utilizing produced X-ray photons than their cone-beam counterparts. The improved exploitation of the X-ray photon flux which is available with CBCT scanners reduces scanning times and increases the signal-to-noise ratio (SNR) in CT projections, respectively, both of which represent a major advantage of CBCT over other geometries.

However, the advantages of increased volume coverage come along with an increase of artifacts caused by scattered radiation. From scientific work in the past, it is well-known that scattered radiation gives rise to unwanted secondary signals and thereby leads to the formation of scatter artifacts in the reconstructed CT volume. These artifacts were already known to occur with fan-beam scanners where only small volumes are irradiated at a time. With increasing cone angles as in CBCT, and hence, with large irradiated volumes, scatter artifacts become even more significant. Typical scatter artifacts include streaks, inhomogeneities known as cupping artifact, and, in general, a loss of contrast. In industrial CT, all of them hamper the detection of defects such as cracks and voids which naturally are of low-contrast if they are small-sized. Furthermore, dimensional measurements are negatively affected by scatter since it blurs sharp edges and renders flat surfaces curved in the surface detection step. Also in medical CT, scatter artifacts hamper a reliable medical diagnosis: Streaks may lead to misinterpretation, while inhomogeneities cause incorrect readings of attenuation coefficients (CT numbers or Hounsfield units in

medical CT) which serve as basis for interpretation and quantitative analysis. Thus, there is a need for a correction of scatter-related artifacts, both in medical and industrial CT.

Many different techniques and methods for suppression and correction of scatter-related artifacts have been proposed in the past three decades, most of them for medical CT systems. All of them have certain drawbacks in CBCT, e.g. insufficient scatter artifact compensation observed with suppression techniques and analytical correction methods, or too much computational effort in methods relying on Monte-Carlo simulations. On the other hand, in experimental methods such as in the well-known beam-stop method, it may become necessary to perform a second scan implying additional dose and additional scan time. Additional dose is not acceptable in medical CT, and additional scan time is a serious drawback in both medical and industrial CT. For these reasons, the complete correction of scatter artifacts in CBCT is still considered an open problem in scientific research.

Based on these considerations, the motivation for our work is to initially propose, test, and advance methods and techniques suitable for complete correction of scatter artifacts in CBCT. Also, we aim at devising new approaches where the above mentioned limitations are overcome.

The present work focuses on industrial CBCT applications; we are examining three experimental scatter correction methods. First, the beam-stop array (BSA) method is a well-established technique and serves as reference herein. Second, we test a complementary technique which we call beam-hole array (BHA) method and which has not been applied to industrial CBCT to the best of our knowledge. Comparison measurements between BSA and BHA method reveal distinct differences. Successful scatter correction employing the BHA method is demonstrated by a CT of an industrial part.

Third, we present a new scatter correction method which is based upon temporal modulation of primary signals, denoted as temporal primary modulation (TPM) method. We devised the TPM method when experimenting with a similar technique which relies on the spatial modulation of primary signals. Both these methods feature the great advantage that they measure scatter data within the normal CT scan. This renders a second CT scan unnecessary while dose and scanning time remain the same as before. We give a theoretical introduction to TPM scatter correction, as well as a verification for an essential underlying assumption that is made in the derivation of the TPM method. Initial measurements employing the TPM method are compared to scatter data obtained by the BSA method and show excellent agreement with them. Finally, we perform TPM scatter correction in a CT with a test phantom in order to demonstrate its potential to correct for scatter artifacts within the normal CT scan.

Chapter 2

Fundamentals of Computed Tomography

In this chapter, we want to briefly introduce the most important aspects of computed tomography (CT) as a comprehensive basis for the following work. First, in section 2.1, the fundamental physical interactions between X-rays and matter are discussed. They represent the key mechanisms which constitute the underlying principle of absorption CT.

In section 2.2, CT scanners both in medical and industrial applications are presented. From that point on, we will focus on cone-beam CT scanners (CBCT). The most relevant basics of CBCT are discussed consecutively, comprising the hardware components, X-ray tube and flat-panel detector, as well as the reconstruction algorithm on the software side. Finally, the reconstructed CT volume can be visualized by displaying CT slices, or further processed for 3D rendering and tasks in nondestructive testing (NDT) such as dimensional measurements.

We will conclude this chapter in section 2.3 with an overview of (i) beam-hardening artifacts, (ii) ring artifacts, and (iii) scattered radiation artifacts. Although there exist other commonly encountered CT artifacts, we limit our discussion to these three since they occur in the experiments performed in this work, and hence, are the most relevant for our considerations.

2.1 Physics of X-Radiation

Even though X-radiation is known for its strong capability of penetrating matter and thereby irradiating objects, it still gets attenuated in this process. In fact, radiation intensity decreases exponentially while X-ray photons travel through matter. This is due to the fact that some of the photons interact with the atoms within this material, either by the process of absorption or by the process of scattering. In this section, first we want to explain the general law of attenuation, i.e. the Beer-Lambert law. Second, the underlying physical interaction processes between X-ray photons and matter that are relevant to our work, i.e. the photoelectric absorption process, Rayleigh scattering, and Compton scattering, are discussed briefly. The following sections dealing with the physical aspects that occur in computed tomography are inspired by the illustrations given in the textbooks of Buzug [Buz08], Evans [Eva55], and Podgorsak [Pod10]. Especially the latter offers a very detailed derivation and discussion of the following topics.
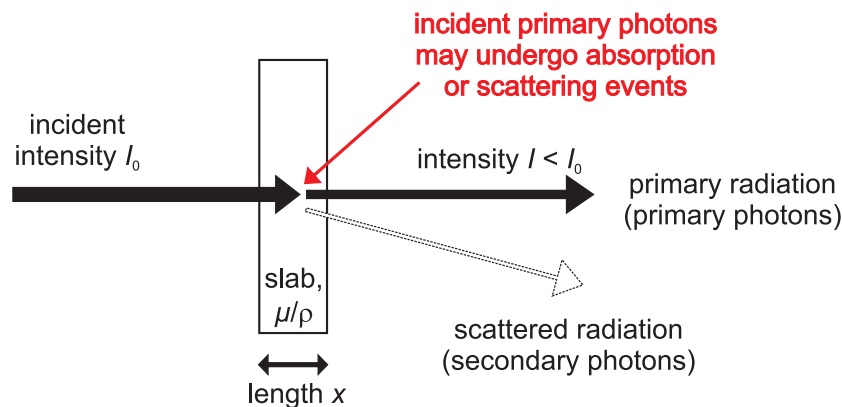
Figure 2.1: Schematic illustration of attenuation of incident radiation intensity I_0 through a thin slab of homogeneous material with the mass attenuation coefficient μ/ρ. Different interaction mechanisms such as absorption and scattering may alter the state of incident photons. Photons that do not interact are left unaltered and are called primary photons or primary radiation. Scattered photons have a different direction of propagation and/or different energy.

2.1.1 X-Ray Attenuation and Beer-Lambert Law

Let us consider a very narrow and monochromatic X-ray beam passing through a thin slab of homogeneous material as illustrated in Fig. 2.1. The X-ray beam may be seen as a stream of particles, namely photons. While passing through the material, each individual photon has a certain probability to interact with the material by one of the interaction processes described in the following sections 2.1.2, 2.1.3, and 2.1.4. Each of the interaction processes fundamentally alters the photon state, e.g. by changing its energy and/or momentum or it completely eliminates the photon. As soon as a photon has undergone an interaction process with the material, we do not call it a primary, unaltered photon any more. While this represents interactions of individual photons in the corpuscular sense, altogether it corresponds to loss of primary photons, and thereby, to attenuation of the X-ray beam.

The attenuation of intensity of the monochromatic, narrow X-ray beam is described by an exponential attenuation law called Beer-Lambert law:

$$I(x) = I_0 \cdot \mathrm{e}^{-\mu(E,Z) \cdot x} \quad . \tag{2.1}$$

Here, I_0 denotes the incident X-ray intensity, $I(x)$ the intensity of the X-ray beam after having passed a penetration length x within the slab, and $\mu(E, Z)$ is the energy- and material-dependent linear attenuation coefficient. Instead of the linear attenuation coefficient $\mu(E, Z)$, in present tabulations, we frequently find the mass attenuation coefficient μ/ρ, with ρ being the density of the absorber material. In the context of cross sections describing the probability of interaction, the mass attenuation coefficient is also given as

$$\mu/\rho = \sigma_{\mathrm{tot}}/uA \,, \tag{2.2}$$

where u is the atomic mass unit, A is the relative atomic mass of the target element, and σ_{tot} is the total cross section for an interaction by the photon. Referring to the

corpuscular image described above, the total cross section can be expressed as the sum over contributions from the principal photon interactions,

$$\sigma_{\text{tot}} = \tau_{\text{PE}} + \sigma_{\text{coh}} + \sigma_{\text{incoh}} \underbrace{\left(+ \sigma_{\text{pair}} + \sigma_{\text{trip}} + \sigma_{\text{ph.n.}} \right)}_{\text{omitted}}, \tag{2.3}$$

where τ_{PE} is the cross section for the atomic photoelectric effect, and σ_{coh} and σ_{incoh} are the coherent Rayleigh and the incoherent Compton scattering cross sections, respectively. In this equation, we may ignore other interaction mechanisms such as pair and triplet production as well as the photonuclear effect. They are omitted as pair production processes only occur at energies at least twice as high as the rest mass energy of an electron, $2m_ec^2 = 1.02\,\text{MeV}$; triplet production only at $E > 4m_ec^2$; and photonuclear effects also have thresholds of the order of a few MeV. As we consider standard X-ray tubes in this work, only photon energies well below $1\,\text{MeV}$ occur.
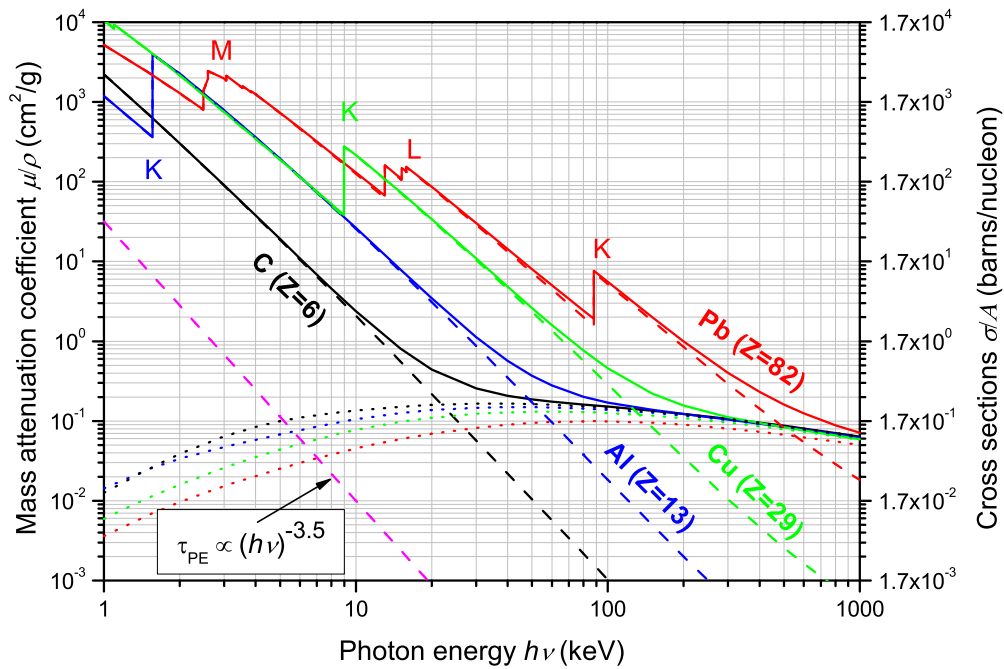
As indicated by Eq. (2.3) there are three interaction mechanisms that are relevant to our work: the photoelectric effect, Rayleigh scattering (coherent) and Compton scattering (incoherent). These are to be discussed separately in sections 2.1.2, 2.1.3, and 2.1.4. Figure 2.2 shows how the individual contributions together give rise to the mass attenuation coefficient μ/ρ and, according to Eq. (2.2), to the total cross section σ_{tot}. Mass attenuation coefficients are displayed for the elements carbon (black solid curve), aluminum (blue), copper (green), and lead (red). As we can deduce from Fig. 2.2, they are governed by the contribution from the photoelectric effect (dashed curves) for lower energies in the range of $1-10\,\text{keV}$ (hydrogen), and $1-200\,\text{keV}$ (lead), respectively. For higher energies in the range of about $100-1000\,\text{keV}$, the Compton interaction (dotted curves) dominates. This explains the inflection point observed in mid-regions of the solid curves where dominance changes from photoelectric effect to Compton scattering. In general, solid curves displayed in Fig. 2.2 for elements with lower Z, e.g. carbon ($Z=6$), exhibit smaller mass attenuation coefficients than those with higher Z, e.g. lead ($Z=82$). Data displayed in Fig. 2.2 are provided by NIST database XCOM [Ber+10]. In this database, we also find that Rayleigh scattering is typically less dominant in the energy range that is of interest to our work, i.e. $30-225\,\text{keV}$. Thus, Rayleigh scattering is not shown explicitly in Fig. 2.2.

2.1.2 Photoelectric Effect

The photoelectric effect is an interaction between an incident photon of energy $h\nu$ and a tightly bound orbital electron of the absorber atom. Figure 2.3 shows a schematic illustration of the photoelectric effect, colloquially often referred to as photoeffect. During this interaction the photon is completely absorbed and the orbital electron is either excited or it is ejected from the atom as a so-called photoelectron with kinetic energy E_{kin}. Thus, the photoelectric effect represents an ionization process. Its energy balance reads

$$h\nu \rightarrow E_{\text{ion}}(\text{atom}^+) + E_{\text{kin}}(e^-). \tag{2.4}$$

Equation (2.4) implies that the photoelectron leaves the atom with the kinetic energy $E_{\text{kin}} = h\nu - E_{\text{B}}$, where E_{B} denotes the binding energy of the electron to the atom. The described energy uptake by the photoelectron may be insufficient for its complete

Figure 2.2: Total mass attenuation coefficients (solid curves) for carbon, aluminum, copper, and lead. The contributions of principal photon-matter interactions are displayed as dashed curves for the photoelectric effect (absorption) and as dotted curves for the incoherent scattering (Compton scattering). Data are taken from NIST database XCOM [Ber+10]. $1\,\text{barn} = 10^{-24}\,\text{cm}^2$.
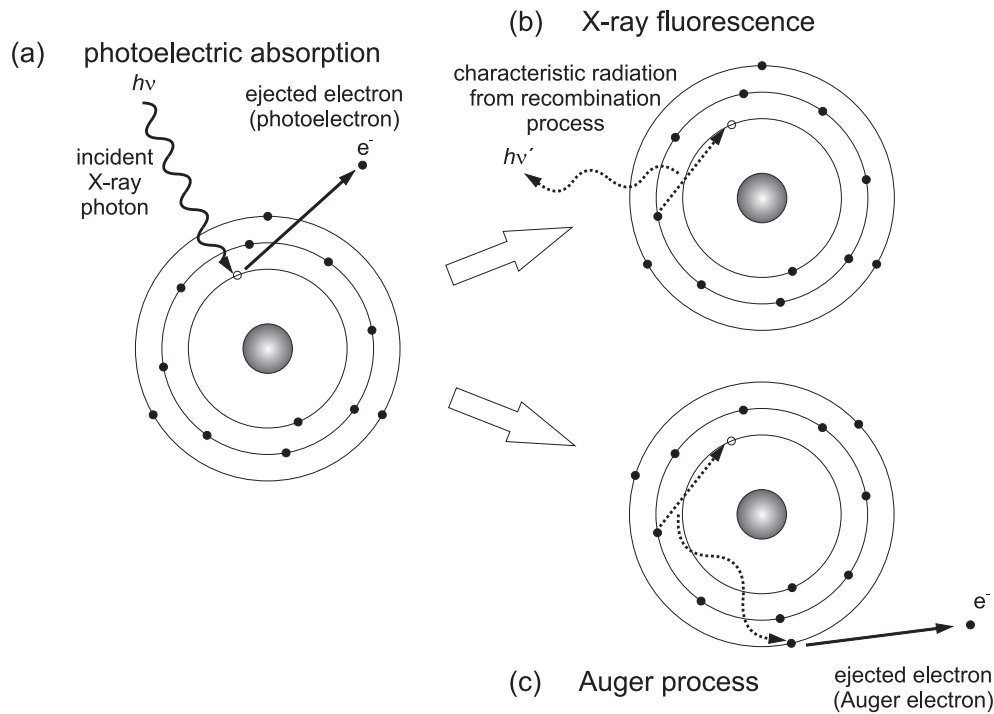
Figure 2.3: Schematic illustration of the photoelectric effect. (a) An incident X-ray photon is absorbed and its energy $h\nu$ is transferred completely, to both the electron, which mostly is an inner-shell electron, and to the lattice. The so-called photoelectron is ejected. Its vacancy is filled by a higher orbit electron whereas either a characteristic fluorescence photon is emitted (b) or another photoabsorption process occurs, known as Auger process (c).

ejection from the atom (atomic ionization process), but it may be sufficient to raise the photoelectron to a higher orbit (atomic excitation process). The vacancy left by the photoelectron when it gets emitted is filled by an electron from a higher shell. As a result of this recombination process, the transition energy will be emitted either as characteristic X-ray fluorescence photon (Fig. 2.3(b)) or as an Auger electron (Fig. 2.3(c)), respectively. Auger electrons are created if the radiation energy of the recombination process for the electron vacancy is sufficient for a subsequent photoabsorption by another electron from an outer shell. Sometimes this process is referred to as radiation-free transition or internal conversion.

For incident photon energies between $1\,\text{keV}$ and $1\,\text{MeV}$, the dashed curves in Fig. 2.2 display the atomic cross section for the photoelectric effect τ_{PE} (absorption coefficient) for a number of different elements ranging from $Z=6$ (carbon) to $Z=82$ (lead). The curves exhibit a sawtooth-like profile with sharp discontinuities, which are called absorption edges and which appear whenever the incident photon energy corresponds to the binding energy of one of the electron shells. The highest absorption edge coincides with the K-shell electron binding energy.

Occurrence of these absorption edges can be explained by the fact that, if the energy of the incident photon is smaller than the binding energy related to a certain electron shell, the energy is not sufficient to lift the electron to an excited, quantum mechanically

allowed state. Thus, this photon cannot induce photoelectric absorption processes with electrons from this specific shell. On the other hand, incident photons with energies equal or greater than the binding energy are able to induce the photoelectric effect, thereby causing a steep increase in the cross section. For greater wavelengths, i.e. smaller energies, the occurrence of absorption edges for L and M shells is explained analogously. The fine structure of shells above the K-shell is due to LS coupling and jj coupling (for heavy atoms) and gets reproduced in the absorption spectrum (Fig. 2.2).

A complete theoretical prediction concerning the atomic cross section for the photoelectric effect (absorption coefficient) τ_{PE} is complex [Eva55, p. 696], particularly in the vicinity of absorption edges. However, a useful approximation is given as follows [Pod10]:

$$\tau_{\mathrm{PE}} = \alpha^4 (_{\mathrm{e}}\sigma_{\mathrm{Th}}) Z^n \sqrt{\frac{32}{\varepsilon^7}} \ , \tag{2.5}$$

where $\varepsilon = h\nu/m_{\mathrm{e}}c^2$ is the normalized photon energy, α is the fine structure constant, Z the atomic number of the absorber, $_{\mathrm{e}}\sigma_{\mathrm{Th}}$ the Thomson *electronic*[1] cross section, cf. Eq. (2.7), and n the power for the Z dependence ranging from $n = 4$ at relatively low photon energies to $n = 4.6$ at high photon energies. For comparison, in Fig. 2.2, we have added a plot of the rough approximation $\tau_{\mathrm{PE}} \propto (h\nu)^{-3.5}$ given by Eq. (2.5). Note that in general there is a good agreement between approximation and measured data of absorption coefficients. The strong increase of the probability of photoelectric absorption with atomic number Z of the absorber, also expressed in Eq. (2.5), is a primary criterion for the usage of lead (Z=82) or tungsten (Z=74) as absorber material employed for X-ray shielding or as lamellae in anti-scatter grids, cf. section 3.3.1.

2.1.3 Rayleigh Scattering

The process of Rayleigh scattering is of elastic and coherent nature, i.e. energies of the incident and scattered X-ray photon are the same, $h\nu = h\nu'$, and their phases are correlated. However, they have different directions of propagation, which is expressed through a scattering angle θ. Before describing the Rayleigh scattering process involving the entire atom with its strongly bound electrons, we first discuss Thomson scattering, which is a form of elastic scattering on quasi-free electrons shown in Fig. 2.4.

In a non-relativistic classical picture, the process of Thomson scattering can be described by an incident electromagnetic wave with wavelength λ and associated energy $h\nu$ which passes an atom with quasi-free electrons. As depicted in Fig. 2.4, the oscillating electrical field of the incident wave sets each of the quasi-free electrons into a forced resonant oscillation. This represents an induced dipole oscillation of the electrons and leads to re-emission of electromagnetic radiation which can be calculated by classical theory of electrodynamics, cf. [Pod10, pp. 291–295]. In this model, the differential electronic cross section per unit solid angle for Thomson scattering $\mathrm{d}_{\mathrm{e}}\sigma_{\mathrm{Th}}/\mathrm{d}\Omega$ is derived as

$$\frac{\mathrm{d}_{\mathrm{e}}\sigma_{\mathrm{Th}}}{\mathrm{d}\Omega} = \frac{r_{\mathrm{e}}^2}{2} \left(1 + \cos^2\theta\right) \ , \tag{2.6}$$

---

[1]Here and in the following, the pre-subscript indicates whether the cross section refers to the electronic (*e*) or atomic (*a*) cross section.
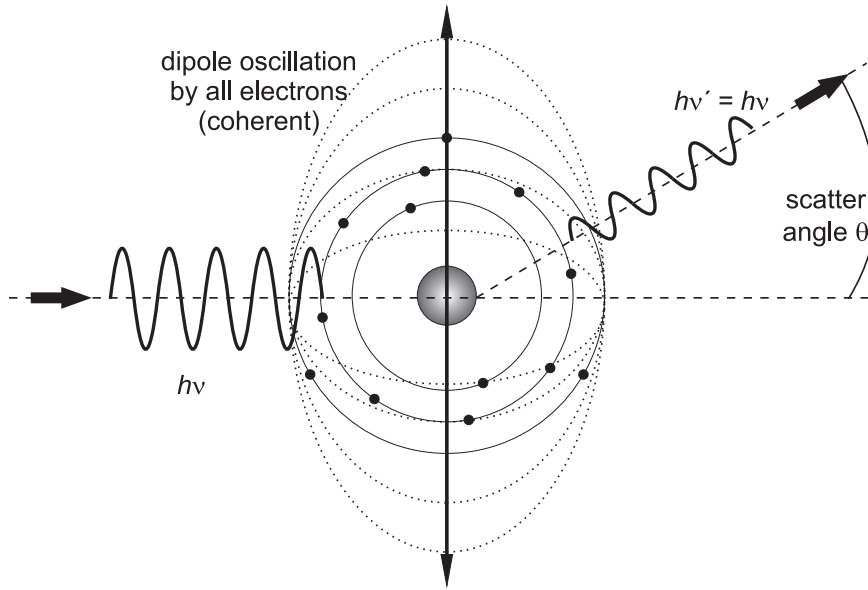
Figure 2.4: Schematic illustration of elastic scattering: By classical theory, the field of the incident X-ray induces a dipole oscillation by coherently driving quasi-free electrons of the atom up and down (Thomson scattering). One can calculate the cross section for re-emission of electromagnetic radiation.

where r_e denotes the electron radius.

The total electronic cross section $_e\sigma_{Th}$ for Thomson scattering can then be simply obtained by integration over the whole solid angle Ω:

$$_e\sigma_{Th} = \int \frac{d_e\sigma_{Th}}{d\Omega}\,d\Omega = \frac{8\pi}{3}r_e^2\;. \tag{2.7}$$

This is a remarkable result as the classical Thomson cross section for quasi-free electrons does not contain energy-dependent terms, i.e. it yields a constant value regardless of the incident photon energy.

Returning to Rayleigh scattering and the correct calculation of its cross section, one has to take into account that the electrons are not quasi-free, but bound to the atom with distinct binding energies. Therefore, the differential Thomson cross section from Eq. (2.6) is weighted by an atomic form factor yielding the differential Rayleigh atomic cross section per unit solid angle:

$$\frac{d_a\sigma_R}{d\Omega} = \frac{d_e\sigma_{Th}}{d\Omega}\{F(q,Z)\}^2 = \frac{r_e^2}{2}\left(1 + \cos^2(\theta)\right)\{F(q,Z)\}^2\;, \tag{2.8}$$

where $F(q,Z)$ is the atomic form factor for Rayleigh scattering with the atomic number Z of the absorber, and the momentum transfer[2] is given by $\hbar q$, where

$$q = \frac{4\pi}{\lambda}\sin(\theta/2)\;, \tag{2.9}$$

---

[2]In the scattering process, the momentum transfer to the electrons is given by $\hbar\boldsymbol{q} = \hbar(\boldsymbol{k'} - \boldsymbol{k})$, where $\hbar\boldsymbol{k}$ is the momentum of the incident photon and $\hbar\boldsymbol{k'}$ of the emitted photon. $\boldsymbol{k}$ and $\boldsymbol{k'}$ are the wave vectors of incident and emitted wave, $|\boldsymbol{k}| = |\boldsymbol{k'}| = 2\pi/\lambda$.
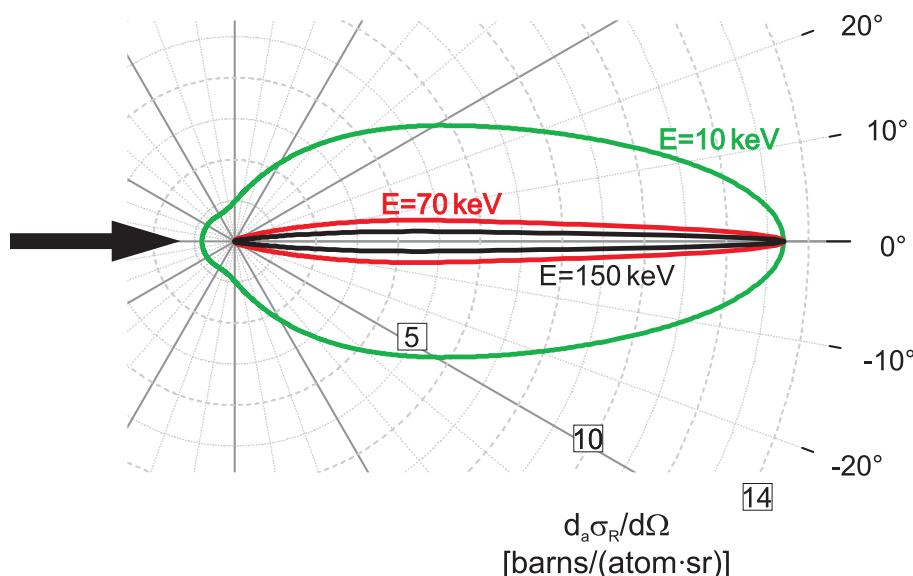
Figure 2.5: Angular distribution $\mathrm{d_a\sigma_R/d\Omega}$ of Rayleigh scattering on an aluminum atom (Z=13) for three different incident photon energies in a polar plot. Scatter distributions are strongly forward peaked and become even more so as the photon energy increases. $1\,\mathrm{barn} = 10^{-24}\,\mathrm{cm^2}$.

where θ is the scattering angle, and λ is the wavelength of the incident photon in angstrom (Å). Atomic form factors $F(q, Z)$ are based on atomic wave functions and can be calculated analytically only for the hydrogen atom. For all other elements, approximations and atomic models, such as the Thomas-Fermi, Hartree and Hartree-Fock model are used for calculation of $F(q, Z)$. Tabulations of the atomic form factor can be found in several publications using different models, e.g. [Sch+83].

Using Eq. (2.8) and the form factors tabulated in [Sch+83], Fig. 2.5 exemplarily shows the angular distribution of Rayleigh scattering on an aluminum atom (Z=13) for three different energies in a polar plot. As we can see, scatter distributions are strongly forward peaked and become even more so as the photon energy increases. Compared to Compton scattering, scattering angles for Rayleigh scatter events are relatively small. Thus, although Rayleigh scattering is less probable to occur than the other two interaction mechanisms as it was concluded from the discussion regarding Fig. 2.2, it is yet relevant to our considerations since a great amount of photons with Rayleigh interaction will be scattered onto the detector, cf. section 2.3.3.

By substitution of $\mathrm{d}\Omega = 2\pi \sin\theta\,\mathrm{d}\theta$ in Eq. (2.8), we obtain the Rayleigh differential atomic cross section per unit scattering angle as

$$\frac{\mathrm{d_a\sigma_R}}{\mathrm{d}\theta} = \frac{\mathrm{d_a\sigma_R}}{\mathrm{d}\Omega}\frac{\mathrm{d}\Omega}{\mathrm{d}\theta} = \pi r_{\mathrm{e}}^2 \sin\theta \left(1 + \cos^2\theta\right) \{F(q, Z)\}^2 \,. \tag{2.10}$$

The Rayleigh atomic cross section σ_{coh} from Eq. (2.3) is either given by the area under the appropriate curve shown in Fig. 2.5 (for the example of aluminum) or, in general, it
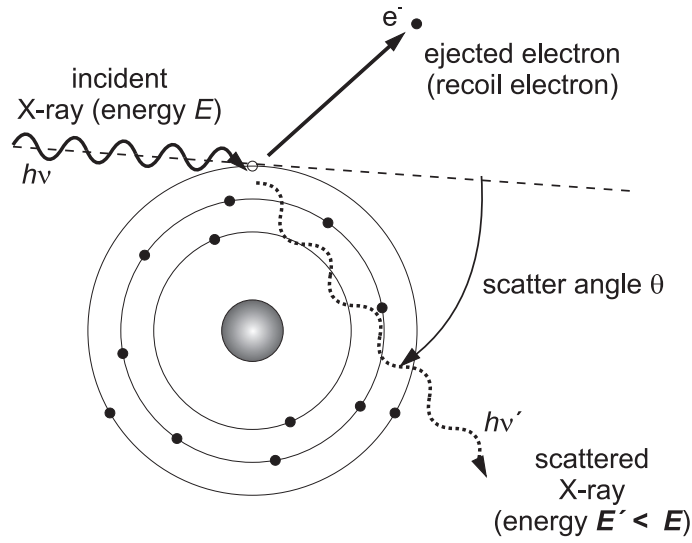
Figure 2.6: Schematic illustration of a Compton scattering process. The incident X-ray photon transfers a part of its energy to an orbital electron. The photon is scattered with a scattering angle θ and carries less energy than before, $h\nu' < h\nu$. The remaining energy is transferred to the Compton recoil electron, which typically gets ejected from the atom.

may be calculated by integration of Eq. (2.10) over all possible scattering angles θ from 0 to π:

$$\sigma_{\mathrm{coh}} = \pi r_{\mathrm{e}}^2 \int_0^\pi \sin\theta \left(1 + \cos^2\theta\right) \{F(q, Z)\}^2 \,\mathrm{d}\theta \;. \tag{2.11}$$

2.1.4 Compton Scattering

The third important interaction mechanism between X-ray photons and atoms that we want to discuss is the process of Compton scattering, which is also known as incoherent scattering. It is schematically illustrated in Fig. 2.6. In a Compton scattering process, an incident X-ray photon collides with a quasi-free, i.e. loosely bound, orbital electron of the absorber material. The incident photon of energy $h\nu$ is scattered on the weakly bound electron under a certain scattering angle denoted as θ. During this collision event, the photon transfers not all of its energy to the electron as in the photoelectric absorption process, but only a part of it. Thus, the energy balance for Compton scatter processes reads as follows:

$$h\nu \rightarrow E_{\mathrm{kin}}(\mathrm{e}^-) + h\nu' \;. \tag{2.12}$$

The right-hand side of Eq. (2.12) indicates that Compton scattering has two outcomes: First, a scattered photon with energy $h\nu'$ that is less than that of the incident photon, and second, a Compton recoil electron that carries the transferred energy $E_{\mathrm{kin}} = h(\nu - \nu')$ which usually is large enough to eject the electron from the atom. Subsequent ionization and scattering processes involving the scattered photon and/or the Compton electron are possible.

2.1.4.1 Compton Wavelength-Shift Equation

A relationship between the wavelength of the incident and the scattered photon was derived by Compton[3] in 1923 [Com23]. In his work, he assumed corpuscular nature of the photon and applied conservation laws of energy and of momentum as well as the relativistic energy-momentum relation $E = mc^2$ to arrive at the well-known Compton wavelength-shift equation:

$$\Delta\lambda = \lambda' - \lambda = \frac{h}{m_{\mathrm{e}}c}\left(1 - \cos\theta\right) . \tag{2.13}$$

Here, λ' is the wavelength of the scattered photon, λ is the wavelength of the incident photon and θ denotes the scattering angle for the photon. The Compton equation states that the shift in wavelength depends solely on the scattering angle θ and does not depend on the energy of the incident photon.

2.1.4.2 Klein-Nishina Formula

In 1928, Otto Klein and Yoshio Nishina derived a formula for the differential cross section of Compton interactions. The Klein-Nishina formula was one of the first results obtained from the studies of quantum electrodynamics. It takes into account relativistic and quantum mechanical effects and accurately describes the experimentally observed X-ray scattering from a single free electron. The differential Klein-Nishina electronic cross section per unit solid angle for Compton effects is given as follows [Pod10, p. 309]:

$$\frac{\mathrm{d}_{\mathrm{e}}\sigma_{\mathrm{C}}^{\mathrm{KN}}}{\mathrm{d}\Omega} = \frac{r_{\mathrm{e}}^2}{2}\left(\frac{\nu'}{\nu}\right)^2\left\{\frac{\nu'}{\nu} + \frac{\nu}{\nu'} - \sin^2\theta\right\} = \frac{\mathrm{d}_{\mathrm{e}}\sigma_{\mathrm{Th}}}{\mathrm{d}\Omega}F_{\mathrm{KN}}(h\nu, \theta), \tag{2.14}$$

where ν is the frequency of the incident photon and ν' the frequency of the scattered photon. In the last equation, the differential electronic cross section for Thomson scattering from Eq. (2.6) is inserted. Hereby, one obtains the Klein-Nishina form factor $F_{\mathrm{KN}}(h\nu, \theta)$ as:

$$F_{\mathrm{KN}}(\varepsilon, \theta) = \frac{1}{[1 + \varepsilon\left(1 - \cos\theta\right)]^2}\left\{1 + \frac{\varepsilon^2(1 - \cos\theta)^2}{[1 + \varepsilon(1 - \cos\theta)]\left(1 + \cos^2\theta\right)}\right\}, \tag{2.15}$$

where $\varepsilon = h\nu/(m_{\mathrm{e}}c^2)$ is the normalized energy of the incident photon. Figure 2.7 shows a polar plot of the differential cross section $\mathrm{d}_{\mathrm{e}}\sigma_{\mathrm{C}}^{\mathrm{KN}}/\mathrm{d}\Omega$ for Compton scattering on a single target electron as a function of scattering angle θ. This represents a number-versus-angle distribution of scattered photons. Plots are given for five different ε, $\varepsilon_i = \{0, 0.1, 0.5, 1, 5\}$, which corresponds to energies $E_i = \{0, 51, 255, 511, 2555\}\,\mathrm{keV}$.
For very small energies $\varepsilon \sim 0$, i.e. for $F_{\mathrm{KN}} \sim 1$, the differential Compton cross section approximates the differential Thomson cross section as we can deduce from Eq. (2.15). As shown in Fig. 2.7, this case encompasses the largest area under the curve $\mathrm{d}_{\mathrm{e}}\sigma_{\mathrm{C}}^{\mathrm{KN}}/\mathrm{d}\Omega$, which exhibits two maxima at scattering angles of $\theta = 0°$ and $\theta = 180°$. With increasing energy, the area under the curve $\mathrm{d}_{\mathrm{e}}\sigma_{\mathrm{C}}^{\mathrm{KN}}/\mathrm{d}\Omega$ decreases while the curve itself becomes increasingly asymmetrical and only exhibits a single maximum in forward direction. Corresponding

---

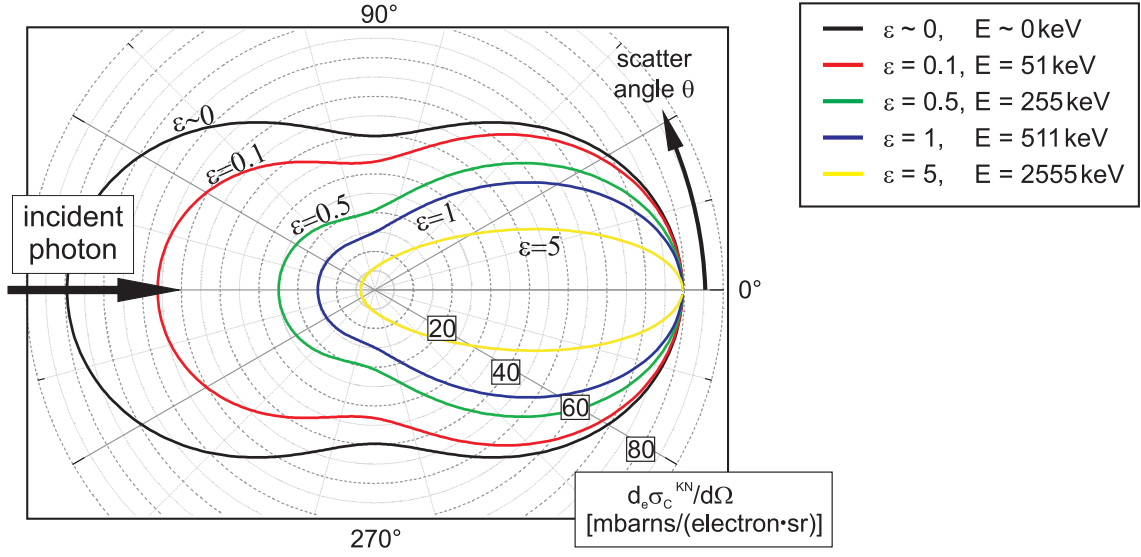[3]Compton was awarded the Nobel Prize in Physics for his discovery in 1927.

Figure 2.7: Angular distribution of photons that are Compton scattered on a single free elec-
tron, given for five different normalized energies ε of the incident photon, and given
by the differential electronic cross section per unit solid angle, $\mathrm{d_e}\sigma_C^{KN}/\mathrm{d}\Omega$. Comp-
ton scatter cones are relatively broad for energies relevant in the present work,
i.e. $30 - 225\,\mathrm{keV}$. $1\,\mathrm{mbarn} = 10^{-27}\,\mathrm{cm^2}$.

plots for angular energy distribution would even be more sharply peaked due to the
variation of $h\nu'$ with θ [Eva55, p. 690], as implied by the Compton wavelength-shift
equation (2.13).

In order to arrive at the total atomic cross section for Compton interaction $\sigma_{\mathrm{incoh}} = {}_a\sigma_C^{KN}$,
one has to consider two steps.

First, one can integrate Eq. (2.14) over the whole solid angle yielding the total electronic
cross section for Compton scattering on a free electron, ${}_e\sigma_C^{KN}$. This is equivalent to
determining the area under one of the curves in Fig. 2.7 for a specified energy. Assuming
a linear relationship between the cross sections for single free electron and whole atom,
one obtains:

$$
{}_a\sigma_C^{KN} = Z \cdot \left({}_e\sigma_C^{KN}\right) . \tag{2.16}
$$

While this is in good agreement with experimental data for very high photon energies,
for smaller photon energies discrepancies occur due to electronic binding effects. These
have to be taken into account in the next step.

Second, electronic binding effects are incorporated into the model by a multiplicative
correction with the incoherent scattering function $S(q, Z)$ which has been developed by
John Hubbell (National Institute of Science and Technology, USA). The application of
this binding energy correction method involves multiplying the differential electronic cross
section from Eq. (2.14) with the incoherent scattering function $S(q, Z)$ [Hub+75]:

$$
\frac{\mathrm{d_a}\sigma_C^{KN}}{\mathrm{d}\Omega} = \frac{\mathrm{d_e}\sigma_C^{KN}}{\mathrm{d}\Omega} S(q, Z) , \tag{2.17}
$$

where the momentum transfer is given by $\hbar q$, $q = 4\pi/\lambda \cdot \sin(\theta/2)$, see Eq. (2.9) above.

With this correction the total Compton atomic cross section $\sigma_{\mathrm{incoh}} = {}_a\sigma_C^{\mathrm{KN}}$ from Eq. (2.3) is given by integration of Eq. (2.17) over the whole solid angle:

$$\sigma_{\mathrm{incoh}} = \int S(q, Z)\frac{\mathrm{d}_e\sigma_C^{\mathrm{KN}}}{\mathrm{d}\Omega}\,\mathrm{d}\Omega\ . \tag{2.18}$$

In analogy to Eq. (2.11), for Rayleigh scattering, by substitution of $\mathrm{d}\Omega = 2\pi\sin\theta\,\mathrm{d}\theta$, one obtains the total Compton atomic cross section σ_{incoh}:

$$\sigma_{\mathrm{incoh}} = \pi r_e^2 \int\limits_0^\pi \sin\theta\left(1 + \cos^2\theta\right) S(q(\theta), Z)F_{\mathrm{KN}}(h\nu, \theta)\,\mathrm{d}\theta\ . \tag{2.19}$$

Compton scattering is the dominant interaction for photon energies used in industrial CT and for many of the materials under study, see Fig. 2.2. Furthermore, from the scatter cones shown in Fig. 2.7, we deduce that Compton scatter leads to a broad spatial distribution of scattered photons. It is for these two reasons that Compton scattering plays a key role in the formation of scatter artifacts that may severely degrade CT image quality, as we will see in chapter 3.

2.1.5 Small-angle X-ray Scattering (SAXS)

Besides the atomic scattering interactions described in sections 2.1.2, 2.1.3 and 2.1.4, also interference phenomena such as X-ray diffraction and small-angle X-ray scattering at larger structures (e.g. pores, macromolecules etc.) exist.

Small-angle X-ray scattering (SAXS) is a technique which builds on the elastic scattering of X-rays into a small angular range (typically $0 - 10°$) by mesoscopic (nanometer range) structures within the sample. SAXS is used in various fields such as materials science, metallurgy, biophysics, and polymer science for probing the size of grain boundaries, precipitations in alloys, micro defects and pores [Hau92; Gui94].

Figure 2.8 schematically illustrates the principle of SAXS: An incident plane wave with wave vector $\boldsymbol{k}$, $k = 2\pi/\lambda$, is elastically scattered by the atoms of the sample. The scattered wave with wave vector $\boldsymbol{k'}$ is detected under a small scattering angle θ and the measured intensity I is proportional to the differential cross section $\mathrm{d}\sigma_{\mathrm{SAXS}}/\mathrm{d}\Omega$ describing SAXS.

In section 2.1.3, we have derived that the differential Thomson cross section of a single electron that scatters the incident wave elastically is given by Eq. (2.6). For small angles θ, $\theta \to 0$, it approaches

$$\frac{\mathrm{d}_e\sigma_{\mathrm{Th}}}{\mathrm{d}\Omega}(\theta \to 0) = r_e^2 = 7.94\cdot 10^{-30}\,\mathrm{m}^2\ . \tag{2.20}$$

Analogous to Eq. (2.8) describing the differential cross section for elastic Rayleigh scattering of one atom, in order to derive the differential cross section for SAXS, here we consider an ensemble of N identical atoms (or, more generally, N identical atomic sets: molecules, cells, or particles) which coherently scatter the incident wave, cf. Fig. 2.8:

$$\frac{\mathrm{d}\sigma_{\mathrm{SAXS}}}{\mathrm{d}\Omega} = r_e^2 \cdot \left|\sum_{n=1}^N F_n(q, Z)\cdot\exp(i\boldsymbol{q}\boldsymbol{r_n})\right|^2\ . \tag{2.21}$$
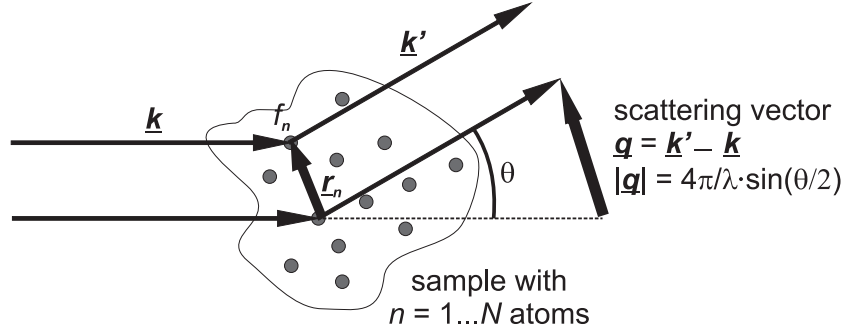
Figure 2.8: Schematic illustration of the elastic scattering of X-rays incident on an ensemble of $n = 1 \ldots N$ identical atoms (or, more generally, N identical molecules, cells, or particles). The incident wave with wave vector $\boldsymbol{k}$ is scattered at a small scattering angle θ which lends its name to this technique called small-angle X-ray scattering (SAXS).

Equation (2.21) represents the summation of all N single atomic scatter contributions, each given by its atomic form factor $F_n(q, Z)$, cf. Eq. (2.8). The phase factor $\exp(i\boldsymbol{q}\boldsymbol{r_n})$ takes account of the topological structure of the ensemble distribution by atom (or particle) positions $\boldsymbol{r_n}$. Here, the scattering vector $\boldsymbol{q}$ is given by

$$\boldsymbol{q} = \boldsymbol{k'} - \boldsymbol{k}; \quad q = \frac{4\pi}{\lambda} \sin(\theta/2). \tag{2.22}$$

For obtaining a substantial SAXS contribution, i.e. constructive interference in Eq. (2.21), it is necessary that the sample under study contains structures with dimensions R of the order of $R \approx 2\pi/q$.

Considering the X-ray CT setup used for the experiments described in this work, in typical applications we encounter a mean X-ray photon energy of $100\,\mathrm{keV}$ and a minimum detectable scattering angle $\theta_{\min} \approx 10^{-4}\,\mathrm{rad}$, if we assume a pixel pitch of $200\,\mu\mathrm{m}$ and a distance between scattering site and detector pixel of $1\,\mathrm{m}$. For these specific values, we can estimate $q_{\min} \approx 10^8\,\mathrm{m}^{-1}$, as well as a maximum structure size that is detectable as it scatters into the nearest neighboring pixels:

$$R_{\max} = \frac{2\pi}{q_{\min}} \approx 60\,\mathrm{nm}. \tag{2.23}$$

Of course, it depends on the sample under study whether its topology contains structures of the specified dimension $R_{\max}$ or smaller. However, from this estimation and assuming a sample that contains these very small structures, we can deduce that SAXS will be limited to a small pixel range surrounding the direct-beam (pencil-beam). Since large volumes are irradiated at once in the cone-beam X-ray CT setup described in section 2.2, the central diffraction peaks of SAXS are not separable from direct beams; it is rather a convolution that is recorded of each of the many incident single pencil-beams with a diffuse, but narrow SAXS scatter contribution. Furthermore, the polychromatic nature of the X-ray spectrum will lead to a superposition of SAXS diffraction patterns of individual scattered photon energies.

2.2 Basics of CT

In the history of computed tomography, different scanner generations have been developed. From a very general point of view, systems have evolved from pencil-beam geometry in the early days, to fan-beam and then to cone-beam geometries, both of which are employed nowadays. Figure 2.9 gives an overview of modern, commercially available CT scanners used for applications in the medical field, on the left-hand side, and for industrial applications on the right-hand side. The systems are also grouped in fan-beam geometry, found in the top row, and cone-beam geometry in the bottom row. Cone-beam CT scanners represent the logical extension of fan-beam CT scanners providing isotropic magnification as well as shorter scan times. In the clinical field, they are used for interventional imaging in angiography and surgery (Fig. 2.9(b)) since they provide better patient access than the fan-beam CT scanner (helical CT, Fig. 2.9(a)). Furthermore, in radiation therapy they are used for guiding, cf. Fig. 2.9(c). In industrial applications, they prove to be advantageous as they enable CTs with very high magnification (micro-tomography, Fig. 2.9(e)) and also reduce scan time.

For the considerations in the present work, the distinction between cone-beam geometry and fan-beam geometry is of greater importance than the distinction of the application fields, i.e. medical or industrial. Thus, from here on we want to focus on cone-beam CT (CBCT) systems as they are more affected by impinging scattered radiation than their fan-beam counterparts, see chapter 3 also. All experiments presented in this work were performed on the industrial lab CBCT scanner that is shown in Fig. 2.9(e).

We briefly summarize the most important parameters relevant to imaging with a CBCT scanner. For this purpose, Fig. 2.10 schematically illustrates the CBCT setup from a top view. The X-ray source emits X-radiation in the form of a cone-beam. The X-rays irradiate the test component that is located on the rotation stage with its center of rotation at a s̲ource-o̲bject-d̲istance, denoted as SOD. X-rays passing the test component are subsequently detected by the f̲lat-p̲anel d̲etector (FPD) behind, which is located at a s̲ource-d̲etector-d̲istance called SDD. The sample is rotated equiangularly and a sequence of 2D projection images is recorded within the full revolution. As can be deduced from Fig. 2.10, details of the test component are projected with a magnification M that is given by

$$M = \frac{\text{SDD}}{\text{SOD}} \ . \tag{2.24}$$

From this, it follows that, at the object plane, details can be resolved with a spatial resolution Δx_{Obj} given by

$$\Delta x_{\text{Obj}} = \frac{\Delta x_{\text{Det}}}{M} \ , \tag{2.25}$$

where Δx_{Det} denotes the pixel resolution of the detector. Equation (2.25) also indicates the nominal resolution of the three-dimensional CT volume. In order to achieve a high magnification M with CBCT, also a small focal spot size of the X-ray source is required due to the penumbra blurring effect, cf. section 2.2.1.

After the acquisition of the CT projections, a reconstruction algorithm is used for calculation of the CT volume based on the projection data. Finally, the reconstructed CT volume may be displayed as cross sections, also known as CT slices, or it can be further
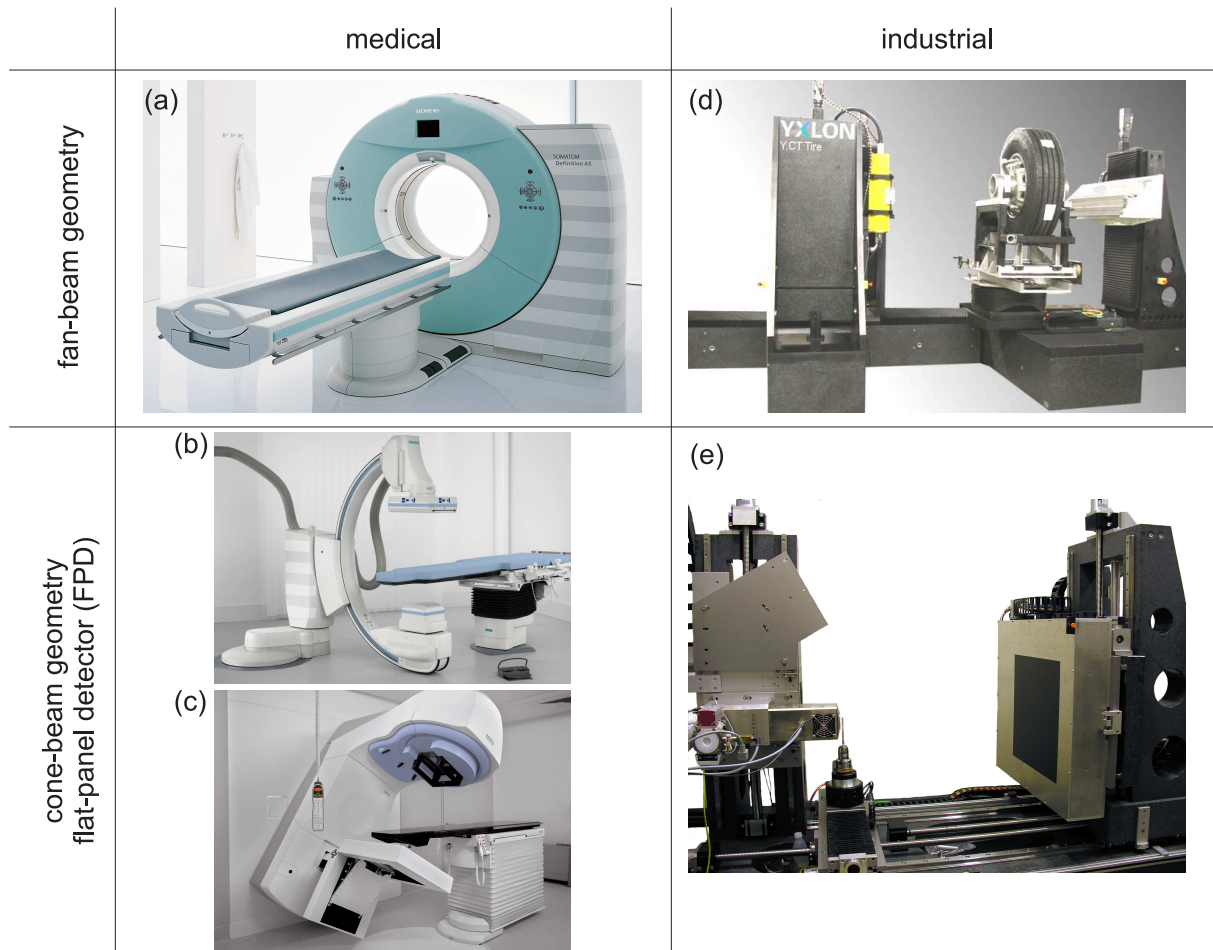
Figure 2.9: Overview of different CT scanners used in the medical and industrial field (see columns). Further distinction is made by the scanner geometry, i.e. fan-beam geometry in the top row versus cone-beam geometry for scanners shown in the bottom row. (a) Helical CT scanner with multi-slice arced detector. (b) C-arm scanner for angiography. (c) Radiation therapy system including mega-voltage CBCT imaging. (d) Industrial CT scanner with line detector. (e) Industrial CBCT scanner used for experiments throughout this work. Left-hand side photographs (a)–(c) by courtesy of Siemens AG. Photograph (d) by courtesy of YXLON International GmbH.
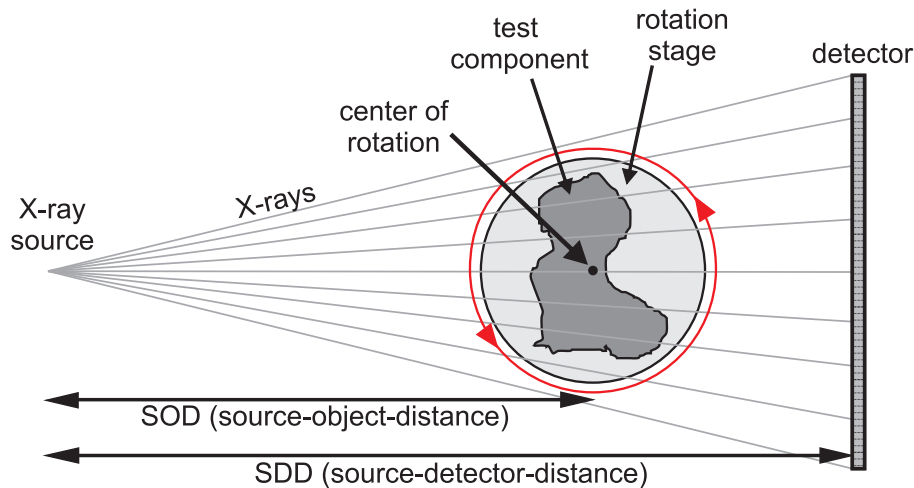
Figure 2.10: Schematic illustration of the cone-beam CT scanner geometry (top view).

processed by rendering algorithms and may be displayed as virtual 3D object. Dimensional measurements are possible once the component's surface has been detected within the 3D CT volume by appropriate algorithms.

The following sections will briefly explain the working principle and the most important parameters of the key elements in the acquisition and reconstruction chain of a CBCT setup, i.e. the X-ray tube, the flat-panel detector, the reconstruction process, and finally the step of visualization and of dimensional measurements.

2.2.1 X-Ray Source

X-radiation is part of the electromagnetic spectrum with energies ranging roughly from $0.1\,\mathrm{keV}$ to a few MeV. Furthermore, it is a form of ionizing radiation, i.e. it is capable of ionizing matter, which may be harmful, particularly to living tissue. Gamma radiation is also a form of electromagnetic radiation and equivalent to X-radiation at the same energies. Gamma- and X-rays are distinguished by their origin: X-rays are generated by high-energetic electrons outside the nucleus, while gamma rays are emitted by the nucleus.

For the generation of gamma radiation, different sources are available. Radioactive isotopes such as Cobalt-60 or Iridium-192 which emit gamma rays are also used in NDT applications. X-rays can be produced by acceleration and deceleration processes of electrons according to classical electrodynamics. Exploiting this fact, large-scale synchrotrons produce synchrotron light up to $100\,\mathrm{keV}$, while linear accelerators (short: linac) and X-ray tubes generate polychromatic X-ray spectra of the order of $1-15\,\mathrm{MeV}$ and $30-800\,\mathrm{keV}$, respectively. The latter two belong to the class of electron impact X-ray sources where mainly *bremsstrahlung* from the deceleration of electrons in a target contributes to the emitted X-ray flux. Only X-ray tubes are relevant to the work presented in this thesis. In the following, we will focus on them and briefly describe their working principle.

Modern X-ray tubes originate from the design of Coolidge tubes from 1913, also called hot cathode tubes. Here, in a vacuum tube, free electrons are generated through the
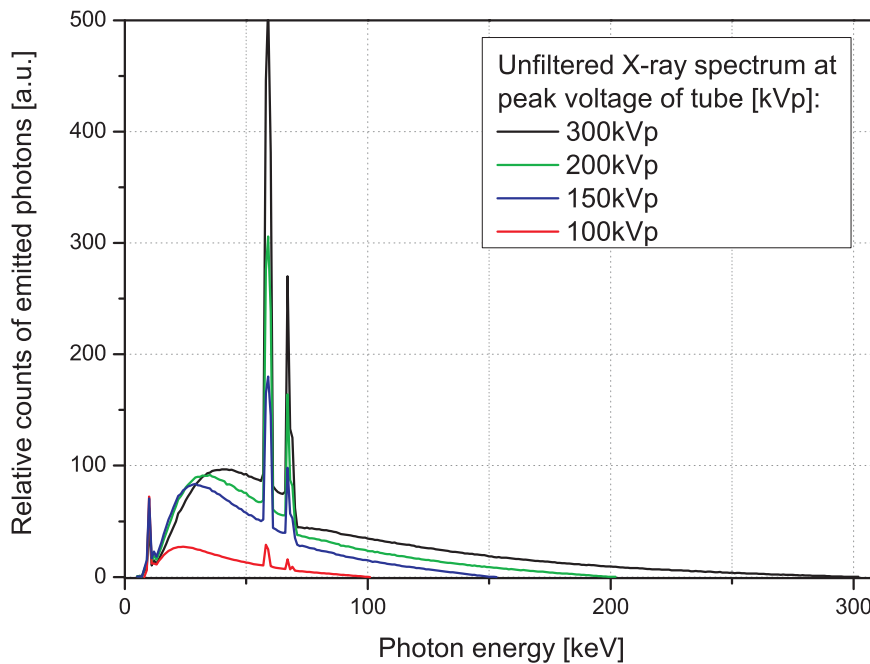
Figure 2.11: Measured X-ray spectra for four different acceleration voltages, data taken from
[Ank00]. The continuous bremsstrahlung spectrum is superimposed by discrete
lines originating from characteristic radiation (see text for details).

thermionic effect by heating a tungsten filament, the cathode. By applying a high voltage
potential between cathode and anode, the electrons get accelerated by the electrical field.
Their velocity, and hence, their kinetic energy increases. The maximum energy $E_{\max}$
they may gain is given by the potential U of the electrical field applied, $E_{\max} = e \cdot U$
with e being the electronic charge. Strongly accelerated electrons hit the anode target
and interact with the atoms of the target material. Essentially, most of the energy the
electrons impart is converted into heat, whereas only about 1% of the energy is converted
into X-rays. Electrons may be slowed down by Coulomb interaction when they are close
to an atomic nucleus or orbital electrons. This deceleration produces bremsstrahlung,
a continuous spectrum of X-radiation shown in Fig. 2.11. The highest energy of an
X-ray photon present in this spectrum is given by the maximum energy which can be
transferred from an electron in a single process, i.e. $E_{\max}$. Thus, the acceleration voltage
determines the upper energetic limit of emitted X-ray quanta, as can be deduced from
the four different spectra in Fig. 2.11. Measured X-ray spectra are provided by the
Physikalisch-Technische Bundesanstalt (PTB) in [Ank00].

The continuous bremsstrahlung spectrum is superimposed by characteristic radiation
which is emitted when an incident electron collides with an inner orbital electron from
an atom in the target material and liberates it. The hole which is left by the orbital
electron is filled by an electron from an outer shell whereby characteristic radiation is
emitted. This explains the characteristic X-ray line spectrum shown for a tungsten target
in Fig. 2.11. The characteristic X-ray lines are material specific, i.e. they are found at
energies which correspond to the differences of binding energies of electrons from different

shells. In Fig. 2.11 this is 59 keV for an electron from the tungsten L-shell filling a hole in the K-shell (Kα line), and 67 keV for an electron from the M-shell (Kβ line).

Ideally, the X-ray tube's focal spot size would be infinitely small and, at the same time, the X-ray photon flux could be adjusted arbitrarily high. From a technical point of view, this poses the problem that all electrons deposit their energy in a very small area of the target whereby they generate heat which soon exceeds a critical limit, i.e. the melting point of the target material. Thus, a tradeoff between focal spot size and photon output of the X-ray tube has to be achieved. Technically, we distinguish between two different X-ray tube designs: On the one hand, the transmission target design, and on the other hand, the side-window tube design. The first is mainly used for NDT applications requiring high magnification whereby high resolutions in the reconstructed CT volume are realized (CBCT micro-tomography of small parts, see above). The latter often employs a rotating anode (for heat load distribution) and is very common in the medical field, but also for NDT applications that do not require extremely small focal spot sizes.

In the experiments described in this work, we employ a micro-focus tube particularly designed for high-resolution NDT applications. Built in transmission target design, it features a thin target (5 µm of tungsten) which allows for focal spot sizes of down to about 2 µm. While enabling high-resolution imaging, such tubes are limited in their electrical power which is of the order of 100 W, and consequentially, in their X-ray photon flux.

2.2.2 Detector

X-ray detection has evolved from the beginnings more than 100 years ago when simple photographic plates and films were used to modern digital flat-panel detectors (FPD) used nowadays. FPDs employ either a photoconductor for direct conversion of X-rays to electrical charge, or a scintillator for indirect conversion from X-rays to visible wavelength photons which are subsequently converted into electrical charge. In both the direct and indirect detection form, initially energetic photoelectrons are produced by the interaction mechanisms described in section 2.1 that initially produce energetic photoelectrons. In direct conversion, the photoelectrons cause further ionization and, thereby, create electron-hole pairs on their passage through matter. Subsequently, these charge carriers are detected, e.g. by an active matrix array (thin-film transistor technology, TFT) coupled to the photoconductor.

Here, we want to describe FPDs with scintillation screens for indirect conversion in more detail since it is a FPD that is used in the experiments carried out in this work. Moreover, it is the most common type of detector employed in industrial CBCT. In Fig. 2.12(a), the working principle of a FPD using a scintillator is illustrated schematically. As with direct conversion, incident X-rays are interacting with the lattice of the scintillator material in a multi-step process, mainly featuring photoelectric absorption and Compton scattering events. As a consequence, many electron-hole pairs arise and thermalize in the conduction and valence bands. They migrate through the scintillation material for a short distance before they recombine at so-called luminescence centers, i.e. dopants specifically added to the lattice of the crystal as activator. In this recombination process, visible light is emitted. A typical value is that for a 60 keV absorbed X-ray photon only about 3300 green-light quanta ($E = 2.4$ eV) are released in a CsI:Tl scintillator [Beu00], for example. The rest of the photon energy is converted in non-radiative energy loss mechanisms.
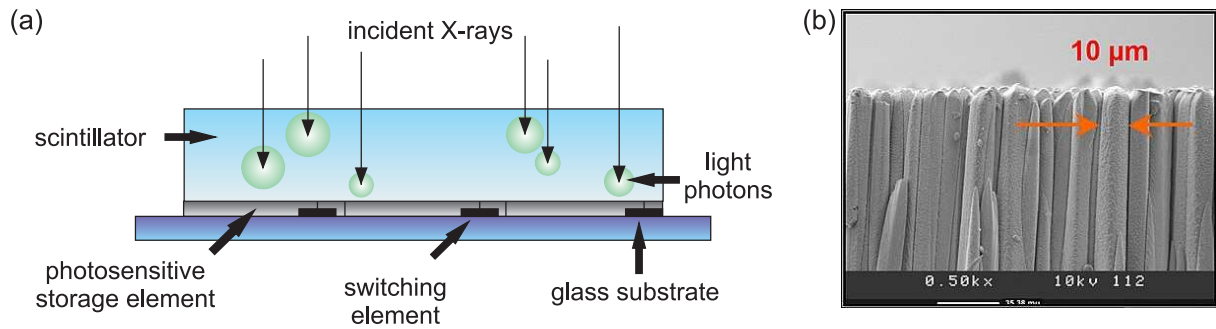
(a)

incident X-rays

scintillator

light photons

photosensitive storage element

switching element

glass substrate

(b)

10 µm

0.50kx   10kv 112

Figure 2.12: (a) Schematic cross-section of a flat-panel detector that employs a scintillation screen for indirect conversion of X-ray photons to visible wavelength photons. These are detected by a TFT active matrix array coupled to the scintillator. Figure adapted from Ref. [Beu00]. (b) Scanning electron microscope (SEM) micrograph of microcolumnar CsI:Tl scintillator (thallium-doped cesium iodide). Photograph by courtesy of Radiation Monitoring Devices, Inc. (RMD).

As shown in Fig. 2.12(a), the scintillator is in close contact to the underlying active matrix array with its photosensitive storage elements. Emitted light photons are detected here and generate electrical charge whose magnitude is proportional to the detected light intensity, and hence, to X-ray intensity absorbed in the close neighborhood of the pixel. By TFT technology, switching elements enable a line-by-line scanning for read-out of the photosensitive storage elements. Electrical signals are amplified and digitized for further processing.

A critical aspect we mention here briefly, concerns the tradeoff between light spread within and X-ray stopping power of the scintillation material. Most generally, a thick scintillation layer is desirable in order to have a high X-ray stopping power, and hence, efficient visible light output yields. However, this is in conflict with the demand of high spatial resolution since a thicker scintillation layer consequentially leads to a greater lateral spread of light. This can be remedied by microstructured materials, such as CsI:Tl, which is shown in a SEM micrograph in Fig. 2.12(b). Here, the CsI:Tl is grown in a columnar structure where the needles act similar to fiber-optic light guides and prevent photons from passing on to adjacent pillars. Micro-structuring is available only for a few scintillation materials with their own drawbacks, e.g. long and persistent afterglow [Kno89, p. 242]. Thus, it does not represent a universal solution. It rather depends on the type of application and its requirements concerning X-ray detection which scintillation material is the most appropriate and best choice. Besides the mentioned columnar-grown CsI:Tl, other widely used scintillation materials are powders, such as e.g. Gd_2O_2S:Tb (called Gadox or GOS), which feature a high refraction index and are incorporated within a non-radiative, but optically transparent binder layer of lower refraction index. Thereby, light photons tend to get reflected at neighboring grain surfaces due to the mismatch between the index of refraction between the binder and the phosphor grains [Beu00].

As we will see in chapter 3, light spread and other diffusion mechanisms within the detector play a key role in the measurements of secondary signals. In fact, they are the cause for high spatial frequencies detected within the scatter images, cf. section 3.1.3

and 4.3. Even if they are not directly avoidable, a comprehensive understanding of these effects is worthwhile.

2.2.3 Reconstruction Algorithms

In this section, we want to review the step of reconstruction of the CT volume, which follows CT data acquisition. The theory of tomographic data reconstruction is extensively covered in scientific literature and many different approaches exist. Most generally, one can classify reconstruction algorithms to be either Fourier-transform based [KS88], algebraic [Kac37; GBH70], or statistical [SV82]. Here, we want to focus on the Fourier-transform based filtered back-projection (FBP) method, which is most common and also used throughout the experiments and simulations described in this work. FBP methods owe their popularity to the fact that they can be performed with much less computational effort than algebraic or statistical algorithms. However, the latter two may reduce certain artifacts that occur with FBP, e.g. beam-hardening artifacts, cf. section 2.3.1. In the future, those methods might become more widely used as computational power is continuously growing.

The brief introduction to FBP reconstruction presented here is only meant to describe the most important aspects of the underlying mathematical foundation. It follows the line of similar, but more detailed treatments in the textbooks by Kak and Slaney [KS88] and by Buzug [Buz08]. Thorough presentations and discussions also concerning the variety of other available reconstruction algorithms and implications to their computational implementation can be found in these textbooks.

2.2.3.1 Radon Transform and Fourier Slice Theorem

In order to illustrate the process of FBP reconstruction, let us consider an ideal situation with parallel-beam geometry and only a single two-dimensional slice of an object for the moment, as shown in Fig. 2.13(a). Let us assume that the X-ray source is monochromatic, and thereby, $\mu = \mu(E=\text{const.})$ in Eq. (2.1). Furthermore, we assume that scattered radiation does not exist. Instead of a thin slab as in section 2.1.1, we here consider an arbitrary object with initially unknown distribution of material, i.e. attenuation coefficient μ. In this situation, the Beer-Lambert law may be rewritten to

$$I(n) = I_0 \, e^{-\int_L \mu(l)\,dl} \,, \tag{2.26}$$

where L represents one of the parallel rays in Fig. 2.13(a), I_0 the incident intensity, and I the measured intensity in the corresponding detector pixel n. We express Eq. (2.26) as a line-integral measurement by normalization $(I(n)/I_0)$ and subsequent application of the negative logarithm:

$$p(n) = -\ln\left(\frac{I(n)}{I_0}\right) = \int_L \mu(l)\,dl \,. \tag{2.27}$$

Since ideal conditions without beam-hardening effects and without scattered radiation are assumed, Eq. (2.27) yields a linear relationship between projection integral p and the measured beam attenuation.
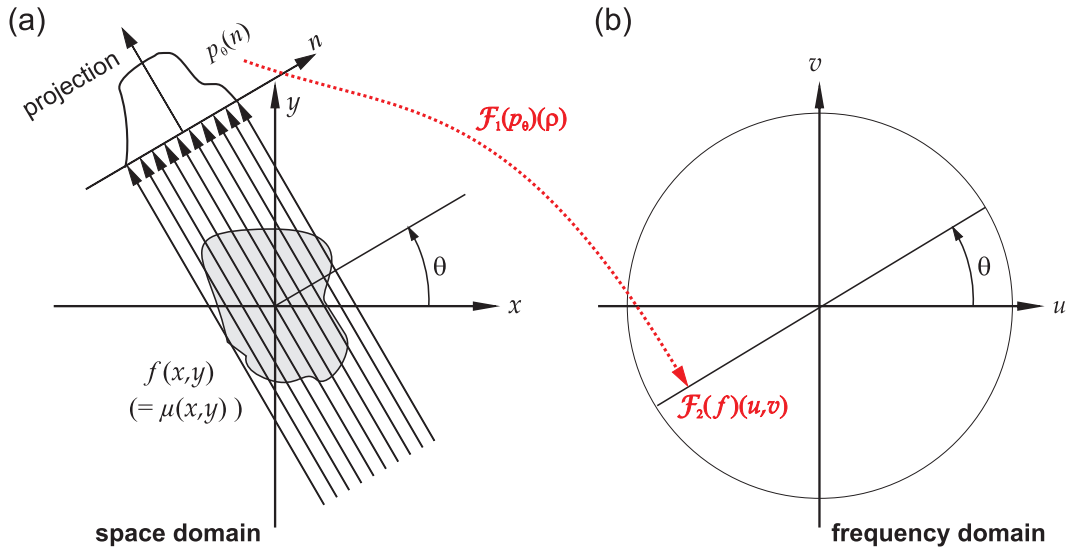
Figure 2.13: Illustration of the Fourier slice theorem, adapted from Ref. [Wie07].

The tomographic data acquisition scan provides us with a set of $\theta = 1 \ldots N_\theta$ angular projections, each consisting of $n = 1 \ldots N_{\text{pix}}$ individual line-integral measurements of the scanned object. For a more general discussion, let us rewrite Eq. (2.27) formally by replacing the distribution of attenuation values $\mu(x, y)$ by a general function $f(x, y)$, and by expressing the integration over beam path L through an equivalent delta function:

$$p_\theta(n) = \int\limits_{-\infty}^{\infty} \int\limits_{-\infty}^{\infty} f(x, y) \delta(x \cos \theta + y \sin \theta - n) \, \mathrm{d}x \, \mathrm{d}y \; . \tag{2.28}$$

Here, the subscript θ enumerates the different angular steps, and n represents the distance from the projected center of rotation, as can be seen in Fig. 2.13(a). $p_\theta(n)$ is called the *Radon transform* of the function $f(x, y)$ and is a first important result in the derivation. The complete 2D set of measured data, i.e. projection integrals $p_\theta(n)$ with $\theta = 1 \ldots N_\theta$ and $n = 1 \ldots N_{\text{pix}}$, represents the so-called *Radon space*.

However, it is the inverse problem that has to be solved as one is interested in finding the original function $f(x, y) = \mu(x, y)$ based on the measurement data $p_\theta(n)$. This problem is solved by the *Fourier slice theorem* that states: The one-dimensional Fourier transform of the (parallel) projection profile, $\mathcal{F}_1(p_\theta)(\rho)$, can be identified with a radial line in the two-dimensional Cartesian Fourier space of the object, $\mathcal{F}_2(f)(u, v)$, drawn at the angle of the corresponding measurement [Buz08], cf. Fig. 2.13:

$$\mathcal{F}_1(p_\theta)(\rho) = \mathcal{F}_2(f)(u, v)\big|_{\substack{u = \rho \cos \theta \\ v = \rho \sin \theta}} \tag{2.29}$$

This represents the most important result for all Fourier-transform based reconstruction methods. The relationship also implies that Fourier transforms of parallel projections from an angular interval of length π cover the two-dimensional Fourier space of the object completely. Taking the two-dimensional inverse Fourier transform of Eq. (2.29),

$f(x, y) = \mathcal{F}_2^{-1}(\mathcal{F}_2(f))(x, y)$, and expressing the volume element in $\mathbb{R}^2$ as $\rho \, \mathrm{d}\rho \, \mathrm{d}\theta$ using polar coordinates instead of Cartesian $\mathrm{d}u \, \mathrm{d}v$, one obtains

$$f(x, y) = \int_0^{2\pi} \int_0^\infty \mathcal{F}_1(p_\theta)(\rho) e^{2\pi i \rho (x \cos \theta + y \sin \theta)} \rho \, \mathrm{d}\rho \, \mathrm{d}\theta \;, \tag{2.30}$$

and after some simplifications (see e.g. [Tur01]):

$$f(x, y) = \int_0^\pi \underbrace{\underbrace{(p_\theta * g)}_{\text{filtering}} (x \cos \theta + y \sin \theta) \, \mathrm{d}\theta}_{\text{back-projection}} \;. \tag{2.31}$$

Here, g denotes the so-called ramp filter [Buz08]:

$$g(n) = \int_{-\infty}^\infty |\rho| e^{2\pi i \rho n} \, \mathrm{d}\rho \;. \tag{2.32}$$

Equation (2.31) is the solution to the initial problem. Giving rise to the name of this method, filtered back-projection (FBP), the process can be divided into two steps: first the filtering of each set of projection data, and second, a back-projection of the filtered projection data over all projection angles. Sometimes, the last step is colloquially also perceived as 'smearing back' the filtered projection values over the entire image plane along corresponding beam paths.

The mathematical derivations so far have been for two-dimensional slices of an object scanned in a setup with parallel beam geometry. In the case of fan-beam geometry, certain geometric adoptions have to be performed, leading to a weighted reconstruction, cf. section 3.4 in [KS88]. As long as the projection data covers an angular interval of π + fan-beam angle, this method is still exact.

2.2.3.2 Three-dimensional Reconstruction Algorithms

For cone-beam geometry and three-dimensional object data to be reconstructed as it is the case for the experiments described in this work, one has to switch to three-dimensional reconstruction algorithms. Here, a major distinction concerning the type of data acquisition and reconstruction comes into play. Within the variety of different Fourier-based approaches that exist, cf. chapter 8 in [Buz08], one distinguishes *approximate* from *exact* 3D volume reconstruction methods.

In this work, the CT experiments and simulations are performed as circular trajectories of X-ray source and detector, or equivalently, as full rotation of the sample whereas source and detector are stationary. For this kind of data acquisition, only approximate reconstruction is possible due to the fact that data sampling in Radon space (for definition, see above) is incomplete[4], cf. [Buz08, p. 366]. This also becomes obvious if one considers

---

[4]Data sampling with a circular scan trajectory can only fill a torus-shaped region within the 3D Radon space. Thus, so-called shadow zones along the axis of rotation, z, exist which make an exact reconstruction of the 3D object impossible.

the *Tuy-Smith sufficiency condition* [Tuy83] which states that exact reconstructions of an object are possible if all surfaces intersecting the object intersect the trajectory of the X-ray source at least once. Only for the central axial plane where the inclination angle is zero, this condition is met and exact reconstruction is feasible. For all other object points in off-centered axial planes with inclination angles $\neq 0$, so-called cone artifacts arise. In this scenario, where the acquisition provides insufficient Radon data, only an approximate reconstruction of the object volume is achievable.

The most frequently used method for approximate reconstruction of 3D object volumes based on cone-beam projections taken with a planar detector is the algorithm proposed by Feldkamp, Davis, and Kress [FDK84]. This state-of-the-art method, which is also often referred to as FDK method, is used throughout the CT experiments described in this work. Related to our simple derivations above describing the principle nature of filtered back-projection, the FDK method represents its extension to the 3D situation. As mentioned, its main shortcoming is the rise of cone artifacts.

Referring to exact methods, a number of different acquisition protocols are available that fulfill the Tuy-Smith sufficiency condition. For example, appropriate trajectories are provided by a helical acquisition [Kat03], or by a short-scan circle plus line [Kat04] or plus arc [Kat05].

2.2.4 Visualization and Dimensional Measurements

After the reconstruction process, the 3D CT volume can be viewed by appropriate software, e.g. VGStudio MAX for industrial CT data [RGP11]. The reconstructed CT volume essentially is a 3D cuboid of single volume elements, called voxel (in analogy to pixel), representing the local attenuation coefficients. Therefore, three orthonormal cross-sectional views of the CT volume, also called CT slices, are a common viewing presentation as illustrated in Fig. 2.14(a). Visualization of the CT volume enables most of the NDT tasks, i.e. one can visually evaluate detected cracks, pores, voids, etc. in the CT slices.

Besides qualitative visual inspection, several other quantitative evaluation tools are available, such as dimensional measurements, wall thickness analysis, porosity analysis, and nominal-actual comparison. For these, first, the object surface has to be detected by gray-value thresholding routines such as e.g. the marching cubes algorithm. Once the surface is detected, further processing and 3D rendering of the CT volume is possible. Figure 2.14(b) shows an example of a nominal-actual comparison displayed in the rendered 3D model. Dimensional measurements may be achieved with an accuracy of about 1/10 of the voxel size [RGP11].

2.3 CT Artifacts

2.3.1 Beam-hardening Artifacts

X-ray tubes used in industrial CT as well as in medical CT are electron-impact X-ray sources as described in section 2.2.1. They exhibit a continuous spectrum of bremsstrahlung and several characteristic emission lines, as shown in Fig. 2.11. For this reason, in our derivations of the line-integral and the mathematical process of reconstruction in
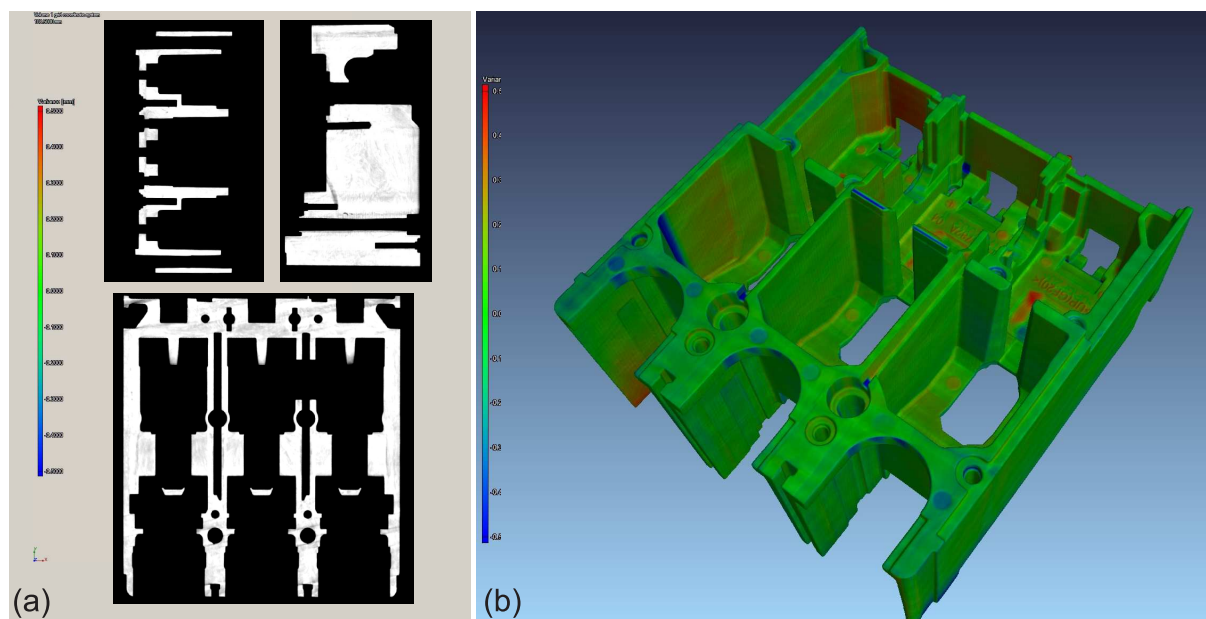
Figure 2.14: (a) Three orthonormal views of a reconstructed CT volume called CT slices, from top left to bottom: axial/transverse, sagittal, and frontal/coronal plane. (b) 3D visualization of CT volume by rendering the detected surface within the CT volume. Colors encode nominal-actual comparison.

section 2.2.3, considering the X-ray source being monoenergetic has been a simplification. The X-ray tube rather features a polychromatic X-ray spectrum $\widetilde{I}_0(E)$ which has to be taken into account in our derivations. When integrated over the maximum energy range, $\widetilde{I}_0(E)$ yields the total incident intensity I_0:

$$I_0 = \int_0^{E_{\max}} \widetilde{I}_0(E)\,\mathrm{d}E \ . \tag{2.33}$$

Furthermore, in section 2.1 we discussed that the radiation attenuation does not only depend on the path length, but also on the physical interaction processes (photoelectric effect, Rayleigh and Compton scattering) with the material which in turn are energy-dependent. Regarding the polychromatic nature of the X-ray sources and the fact that attenuation coefficients are energy-dependent, Eq. (2.1) is no longer valid. It has to be replaced by the following relationship that also incorporates the energy-dependence:

$$I(s) = \int_0^{E_{\max}} \widetilde{I}_0(E)\,e^{-\int_0^s \mu(l,E)\,\mathrm{d}l}\,\mathrm{d}E \ . \tag{2.34}$$

Consequentially, the projection integral from Eq. (2.27) has to be extended to

$$p(n) = -\ln\left(\frac{1}{I_0}\int_0^{E_{\max}} \widetilde{I}_0(E)\,e^{-\int_L \mu(l,E)\,\mathrm{d}l}\,\mathrm{d}E\right) \ . \tag{2.35}$$
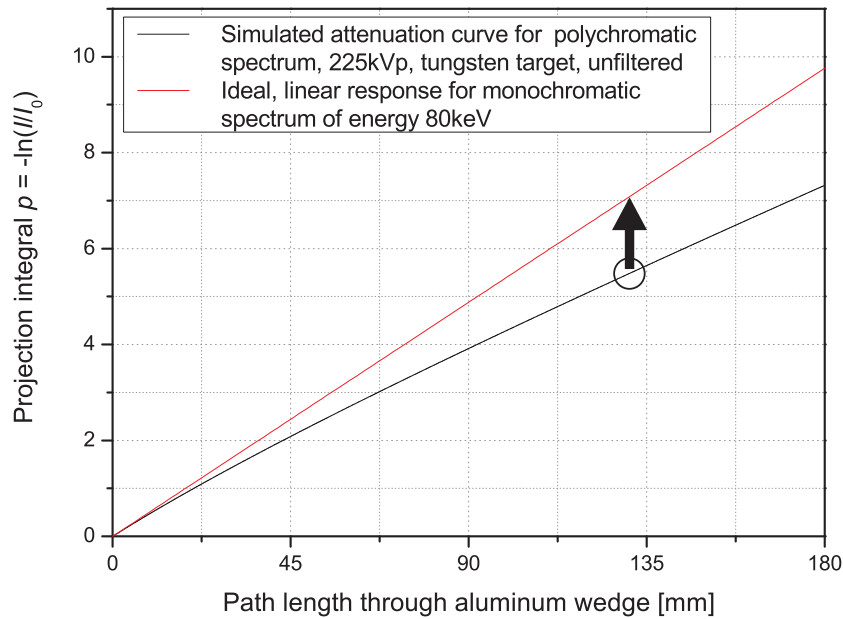
Figure 2.15: Simulated attenuation curves using a monochromatic spectrum of 80 keV (red curve) and a 225 kVp polychromatic spectrum for a tungsten target (black curve). An aluminum wedge as object sample is simulated and attenuated signals I are registered behind. The polychromatic spectrum leads to a non-linear attenuation curve due to the effect of beam hardening. If left uncorrected, this leads to artifacts in the reconstructed CT volume. The linearization approach corrects projection integrals that are measured with polychromatic spectra by mapping them onto the monochromatic case (see arrow).

Equation (2.35) implies that the measured projection integral p and the path length of the material have no longer a linear relationship as in Eq. (2.27). So-called beam-hardening artifacts are a consequence of this non-linearity. The name of beam hardening originates from the following consideration: The polychromatic incident X-ray spectrum changes along the beam path while it penetrates material. More specifically, low-energy photons are more likely to be absorbed or scattered than high-energy photons due to their different attenuation characteristics, as illustrated in Fig. 2.2. As a consequence, the X-ray photon flux loses more low-energy than high-energy photons while penetrating the material. Hence, the X-ray spectrum changes as its mean energy increases. Thereby, it becomes more penetrating in the following – or in other words, the X-ray spectrum gets hardened.

As the mean energy of radiation increases due to the beam-hardening (BHD) effect in the course of X-rays passing the material, the probability of interaction will decrease. Obviously, the strength of this effect depends on penetration lengths. As shown in Fig. 2.15, the longer the penetration length, the greater the non-linearity becomes. As a consequence, the measured intensities for the individual projections are not consistent from different angular directions. Out of this inconsistency beam-hardening artifacts arise. They include streaks in the CT volume at strongly attenuating structures as well as a so-called *cupping* artifact, where homogeneous regions of material appear inhomogeneous,

i.e. a line profile across these regions shows a sagged line. Several techniques exist in order to reduce or correct beam-hardening effects.

First of all and very common in most modern CT scanners, a reduction of BHD effects is reached by beam filtration when the X-rays leave the X-ray tube. A thin plate of aluminum or copper (a few millimeters, at most) may be used for filtering out soft X-ray photons whereby the spectrum is effectively narrowed and hardened before it reaches the sample or the patient, respectively. In practice, a tradeoff between sufficient filtering and large enough dose rate has to be found if scan times are not to exceed a certain level. Second, a theoretically exact and complete correction of BHD effects for single material objects is possible through the so-called linearization approach. As shown in Fig. 2.15, this approach aims at mapping the measured signals (represented by black curve) to signals one would measure in an ideal, monoenergetic case for the same path lengths (red curve). Therefore, a linear relationship between corrected signals and measured path lengths is restored. The mapping function can either be found experimentally [Her79] or by simulations with polychromatic spectra [HM98], as it was done in Fig. 2.15. In the medical field, this approach is also known under the name of water correction [Hsi03; Buz08]. As mentioned before, this pre-processing method (applied before reconstruction) can be correct only for single material objects, since, for objects composed of multiple materials, measured projection integrals represent unknown mixtures of attenuation contributions from the different materials of the sample passed by the beam.

Third, in order to avoid the problem of multi-material samples, a number of iterative schemes incorporating forward-projectioning exist as post-processing methods [JS78; MMS90; Hsi+00].

Fourth and last, the dual-energy approach represents theoretically the most elegant BHD correction [AM76] but it requires two scans with different X-ray tube voltages.

2.3.2 Ring Artifacts

Defect detector channels or a gain miscalibration of detector pixels may cause the formation of ring artifacts in the CT volume. Since X-ray source and detector are installed stationary relative to each other in medical CT, and completely stationary in industrial CT, a pixel with non-linear response causes a wrong signal at the same location in each CT projection. During the back-projection step in the reconstruction process, cf. section 2.2.3, this consistently erroneous reading will form concentric rings in axial planes in the CT volume due to the circular sampling process. Figure 2.16 shows typical ring artifacts encountered in an axial CT slice from a CT where detector calibration is insufficient. Besides issues with imperfect detector behavior, also stationary objects in the projections, other than the test component under study which is rotated, may lead to the formation of ring artifacts as we will investigate in chapter 5. Suppression of ring artifacts in CT is possible by several different post-acquisition algorithms [SP04; KPK09; Tit+09].

2.3.3 Scattered Radiation Artifacts

Scattered radiation is another well-known source of severe CT artifacts, but – in contrast to the above mentioned artifacts – it is still considered an unresolved problem in CBCT [Yan+10; WMS10; ZBF06; ZSF05; PLB08].
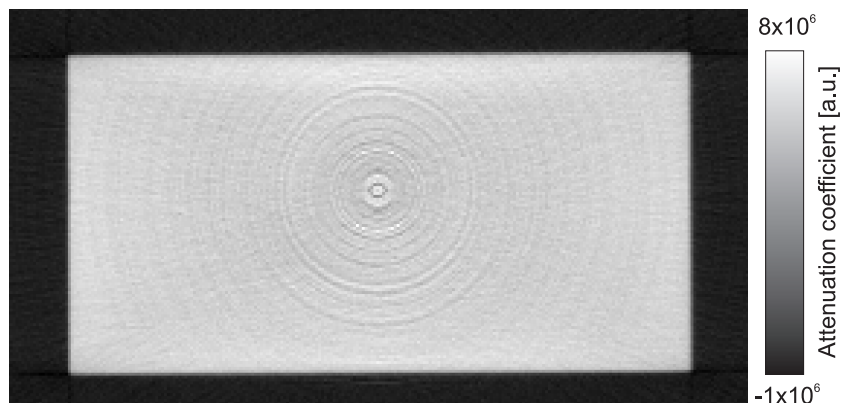
Figure 2.16: Ring artifacts in an axial CT slice arising due to insufficient detector calibration.
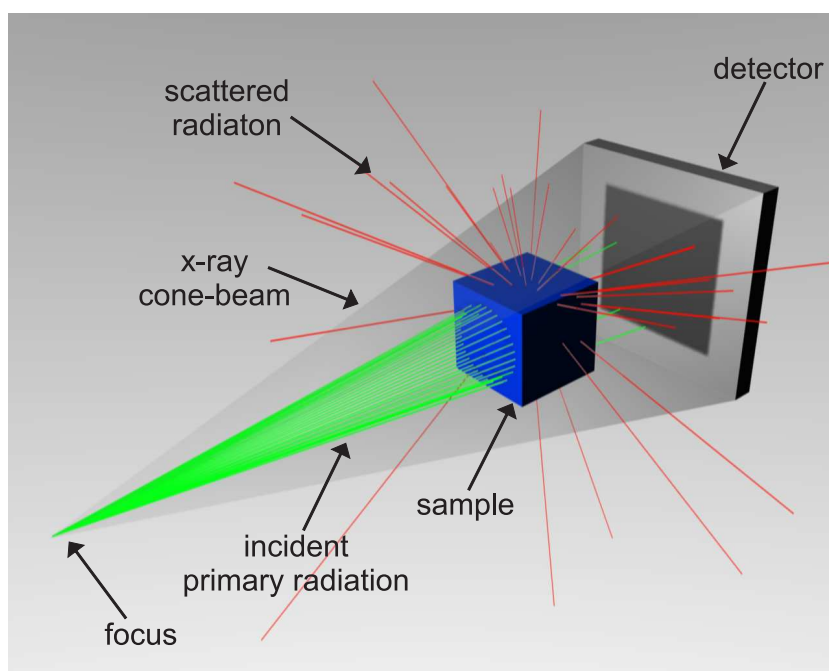
Figure 2.17: Schematic illustration of a cone-beam CT setup where incident primary radiation (green) partially is scattered by the sample. A part of this scattered radiation (red) reaches the detector where it gives rise to scatter signals. Representing an additional signal contribution that is uncorrelated with the attenuation of straight primary X-rays, scatter signals lead to the formation of scatter artifacts in reconstructed CT volumes.

Figure 2.17 schematically illustrates the origin of scatter artifacts: Primary radiation is attenuated by the sample, either by complete absorption (cf. section 2.1.2) of primary photons or by Rayleigh (section 2.1.3) or Compton scattering (section 2.1.4). In fact, as we discussed in section 2.1, for energies used in industrial CT, a great part of the incident X-ray photons is scattered. After interaction, they still exist (as scattered photons) and exhibit a different travel direction and possibly different energy as before. Scattered photons that reach the detector plane give rise to scatter signals. These represent an additional signal contribution which does not correlate with the attenuation of straight primary X-rays and thereby violates Eq. (2.27) by the nonlinearity it introduces to the scan process. As a result, scatter artifacts arise in the CT volume. Although different in its physical origin, the appearance of scatter artifacts is similar to artifacts caused by beam-hardening, e.g. streaks and cupping, as described above in section 2.3.1.

Since the subject of the formation of scatter artifacts and of its contributing sources is extensive, we leave a more detailed discussion of these topics to the next chapter.

Chapter 3

Origin and Correction of Scatter Artifacts in Cone-Beam CT

In both medical and industrial cone-beam CT scanners (CBCT), modern flat-panel detectors are used. They provide instantaneous and complete 2D data acquisition while maintaining a high isotropic spatial resolution. Compared to fan-beam CT scanners, the extended volume coverage reduces the scan time significantly and makes much better usage of the X-ray flux produced by X-ray tubes. However, it also leads to an increased contribution of scattered radiation to the total detected signal. It is generally accepted knowledge [JY82; JS82; Glo82; Kan+85; SJ01] that scattered radiation represents a major source of image degradation in cone-beam CT systems, resulting in artifacts such as cupping in homogeneous regions of material, reduction of contrast, and streaks between regions of high contrast. Additionally, image noise increases when scattered radiation is detected. Dimensional measurements performed in industrial CT are negatively affected in the surface detection step since scatter blurs sharp edges and renders flat surfaces curved.

In section 3.1, we will study the sources of scatter that contribute to the total detected signal through different mechanisms. This is important for the understanding of the experimental results described in chapter 4. Section 3.2 will then give an overview of different scatter artifacts by demonstration of a simulated, ideal CT where we can 'switch on and off' scatter contribution in addition to the desired and correct primary signals. Finally, in section 3.3, we will give a brief review of the most important existent methods and techniques to avoid scatter artifacts that are found in the literature. Some of them are also accepted standards and implemented in commercially available medical CT scanners.

3.1 Sources of Scatter

Reconstruction algorithms, as we introduced them in section 2.2.3, are based on the assumption that only primary radiation I_{prim} reaches the detector and thus, ideally, $P(n)$ is the only contribution to the total detected signal $T(n)$:

$$T(n) = P(n) = c \cdot I_{\text{prim}}(n) \ . \tag{3.1}$$

Here, c is a linear conversion factor between the incident radiation intensity and the output signal. For simplicity's sake, here, we only consider a one-dimensional detector with $n = 1...N_{\text{pixels}}$. Further detector rows can be treated analogously.

Besides the primary signals P, also several secondary events S contribute to the total detected signal at each pixel n of the detector:

$$T(n) = P(n) + S(n) \ . \tag{3.2}$$

$S(n)$ comprises all secondary signals registered at pixel n, consisting of scattered X-ray and fluorescence radiation, as well as non X-ray scatter and spread effects in the detector (detector internal effects), termed $S_{\text{Det}}(n)$. Scattered radiation contributions may stem from different scatter mechanisms and consist of components originating from the object, from the environment and from detector internal scatter events:

$$S(n) = c \cdot (I_{\text{Obj}}(n) + I_{\text{Env}}(n) + I_{\text{Det}}(n)) + S_{\text{Det}}(n) \ . \tag{3.3}$$

Here, I_{Obj}, I_{Env}, and I_{Det} represent scattered X-radiation (Compton and Rayleigh scatter events) caused by the sample, by environmental structures within the CT lab, including the mechanical CT system structure, and by the internal mountings within the detector, respectively. $S_{\text{Det}}(n)$ signifies an additional signal at pixel n originating from adjacent pixels which may contribute by non X-ray scatter mechanisms such as optical light spread in the detector. This additional signal is also related to I_{Obj}, I_{Env}, and I_{Det} from other pixels. To list in a formal way all different sources of secondary signals, here we have strictly distinguished between their origins. In the sections 3.1.1, 3.1.2, and 3.1.3, we will discuss in more detail the three different sources of scatter, i.e. sample, environment, and detector.

3.1.1 Scattered Radiation from the Sample

The scatter contribution originating from the sample is the most manifest and the first we want to discuss here. Incident X-rays coming from the X-ray tube may interact with the atoms in the sample by one of the interaction mechanisms discussed in section 2.1, i.e. the photoelectric effect, Rayleigh and/or Compton scattering. Scattered photons have new directions of propagation and those that reach the detector plane give rise to secondary signals usually at locations that are uncorrelated with the primary photon's beam path. In general, the amount of scattered radiation from the sample that actually is detected and that contributes to total signals, is dependent on *(i)* the atomic number Z and on *(ii)* the size of the sample, as well as on *(iii)* the distance between the scattering sample and the detector plane (air gap, cf. section 3.3.1). Referring to *(i)* the atomic number Z, Compton scattering dominates over Rayleigh scattering for photon energies relevant in industrial CT, as described in section 2.1.1. Figure 2.2 illustrated that in this energy range elements with lower atomic numbers typically show greater cross sections for Compton scattering than higher Z elements, which is due to the incoherent scatter function $S(x, Z)$ describing electronic binding effects (cf. section 2.1.4).

Regarding *(ii)* and *(iii)*, the size of the sample and its distance to the detector are solely geometric parameters. As predicted, it is found by Monte-Carlo simulation [Kal81; Kan+85] and experimental investigation [JY82] that scatter-to-primary ratios (SPR) increase with bigger samples and also by decreasing the distance between sample and detector.
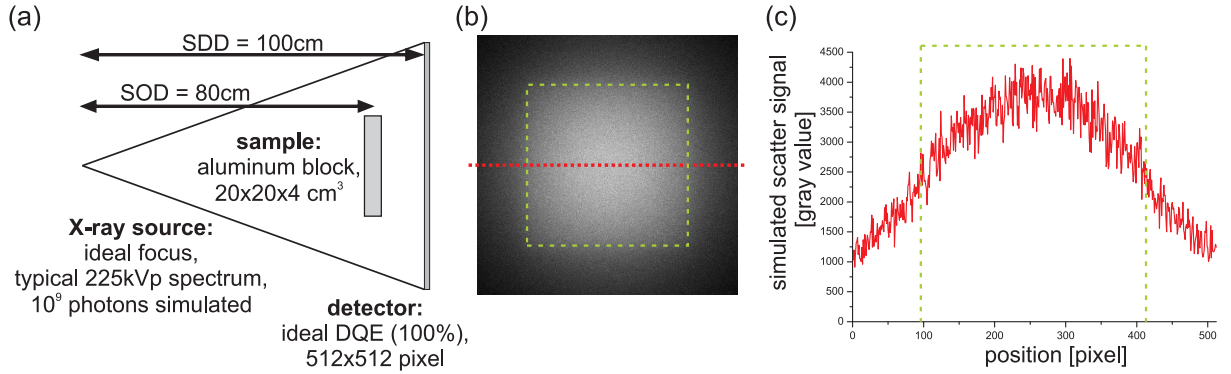
Figure 3.1: (a) Setup for Monte-Carlo simulation stating the simulation parameters and settings. (b) Simulated scatter image formed by object scatter, and (c) corresponding line profile. Cast object shadows are indicated in (b) and (c).

Precise knowledge of the signal contribution due to scattered radiation from the sample, also termed object scatter I_{Obj}, has been the objective of many research activities in the past decades [Kal81; CD83; BS88; HKK91; CB04; NTC04; Mal+05; KRK06; ZB06; ZBF06; Mic+07; PLB08; WMS10; Yan+10]. In fact, since scattered radiation from the sample is the dominating part of total scatter signals in many CT systems, in the literature, object scatter often is the only source of scatter considered. A well-established method to simulate object scatter is given by the Monte-Carlo method [Kal81; CD83]. In Monte-Carlo simulations, the repeated computation of random flight paths of individual photons on their passage through a scattering medium is performed. For each simulated photon trace, the type of interaction, scattering parameters etc. are chosen according to the physical properties of the simulated matter. This yields expectation values of scattered photons on the virtual detector plane as soon as the desired number of hits has been registered.

Representing a typical situation found in industrial CT, Fig. 3.1 exemplifies a Monte-Carlo simulation for a radiographic projection of a rectangular solid made of aluminum that scatters X-rays incident in cone-beam geometry. In Fig. 3.1(a), the simulation scenario is schematically depicted, in (b), the simulated scatter image at the detector plane is given, while in (c), the corresponding line profile for a horizontal line across the mid-plane in the scatter image is shown. Besides the noise due to the statistical distribution of simulated photon tracks, the scatter image contains low spatial frequencies which is a common assumption of object scatter found in the literature [Glo82; BS88; NTC04; ZBF06].

The circumstance that the sample under investigation is scattering incident radiation is unavoidable. However, even if unavoidable, at least there exist techniques to reduce the amount of detected scatter fluence which we will briefly discuss in section 3.3.1.

3.1.2 Scattered Radiation from the Environment

Besides scattered radiation from the sample, we also expect a certain contribution from the CT scanner surroundings, i.e. mechanical structures nearby, that we term environ-

mental scatter contribution I_{Env}. Only in an idealized scenario, within a Monte-Carlo simulation, conditions can be defined such that solely the sample is scattering incident radiation. In real-world experiments, however, it is difficult to eliminate environmental scatter completely as the CT scanner unit, the lab structures and even the detector itself are made of scattering material.

First, we want to examine the environmental scatter contribution in our standard CT setup. Second, we demonstrate a few techniques that reduce detected scatter from the environment. For this purpose, a simple experiment is carried out which yields the approximate ratio of scatter contribution from environmental structures normalized to the total signal in (unobstructed) direct-beam regions:

$$\mathrm{STR} := \frac{S_{\mathrm{Env}}}{T_{\mathrm{direct\text{-}beam}}} \, . \tag{3.4}$$

This quantity shall be termed scatter-to-total ratio (STR). Figure 3.2(a) schematically presents the experimental setup. We use a micro-focus X-ray tube operated at 220 kVp with a 4 mm copper filtering, as well as a flat-panel detector with a $40.96 \times 40.96 \,\mathrm{cm}^2$ scintillation layer of $Gd_2O_2S{:}Tb$ (cf. section 2.2.2). A 10 mm thick lead block is positioned at different source-object-distances (SOD) consecutively and the signal is measured as mean within two regions-of-interest (ROIs) in the projected shadow of the lead block, see marked regions in the projection shown in Fig. 3.2(b). Since the primary radiation, i.e. the direct-beam is absorbed by the lead block here, we only measure secondary signals I_{Env} and I_{Det}.

In a first series, the measurement is conducted with the CT scanner in its standard setup, i.e. without collimating aperture, with the X-ray tube, sample, and detector in a lower position, i.e. their centers 32 cm above the scanner base, and with a 0.4 mm thick carbon-fiber-reinforced plastic (CFRP) plate in front of the detector for protective shielding. The detector is at SDD = 120 cm. Starting with the lead block positioned right in front of the CFRP-shielding at SOD = 117 cm, we decrease SOD and measure signals behind the lead block. Measurement results are given as black curves in Fig. 3.2(c) where the box-markers indicate ROI 1 and the bullet-markers ROI 2 measurements. Decreasing SOD from 117 cm to 100 cm, note the leap in the measured STR from about 1.5% to more than 5%. This can be explained by an increasing accessibility of the ROIs to scattered radiation particularly coming from the granite scanner base below and sideways. In this setting, without collimating aperture, the X-ray cone-beam is covering an area larger than the detector area and radiation is incident on the scattering scanner base, too.

When further decreasing SOD, the measured STR starts to decrease again. This is explained by increasingly larger portions of incident radiation absorbed by the lead block as its enclosing cone angle becomes larger.

The situation may be greatly improved by a proper collimating aperture that limits the cone-beam to the detector plane as well as by an elevated scanner position where X-ray tube, sample and detector are 50 cm above the scattering scanner base (upper position). We conduct the same measurement by moving the lead block to vary SOD and obtain the measurement results shown as red curves in Fig. 3.2(c). In this setting, measured STRs are close to 1.5% for all SODs.

Finally, we have identified the CFRP plate mounted right in front of the detector as protective shielding to be another source of environmental scatter. The third series
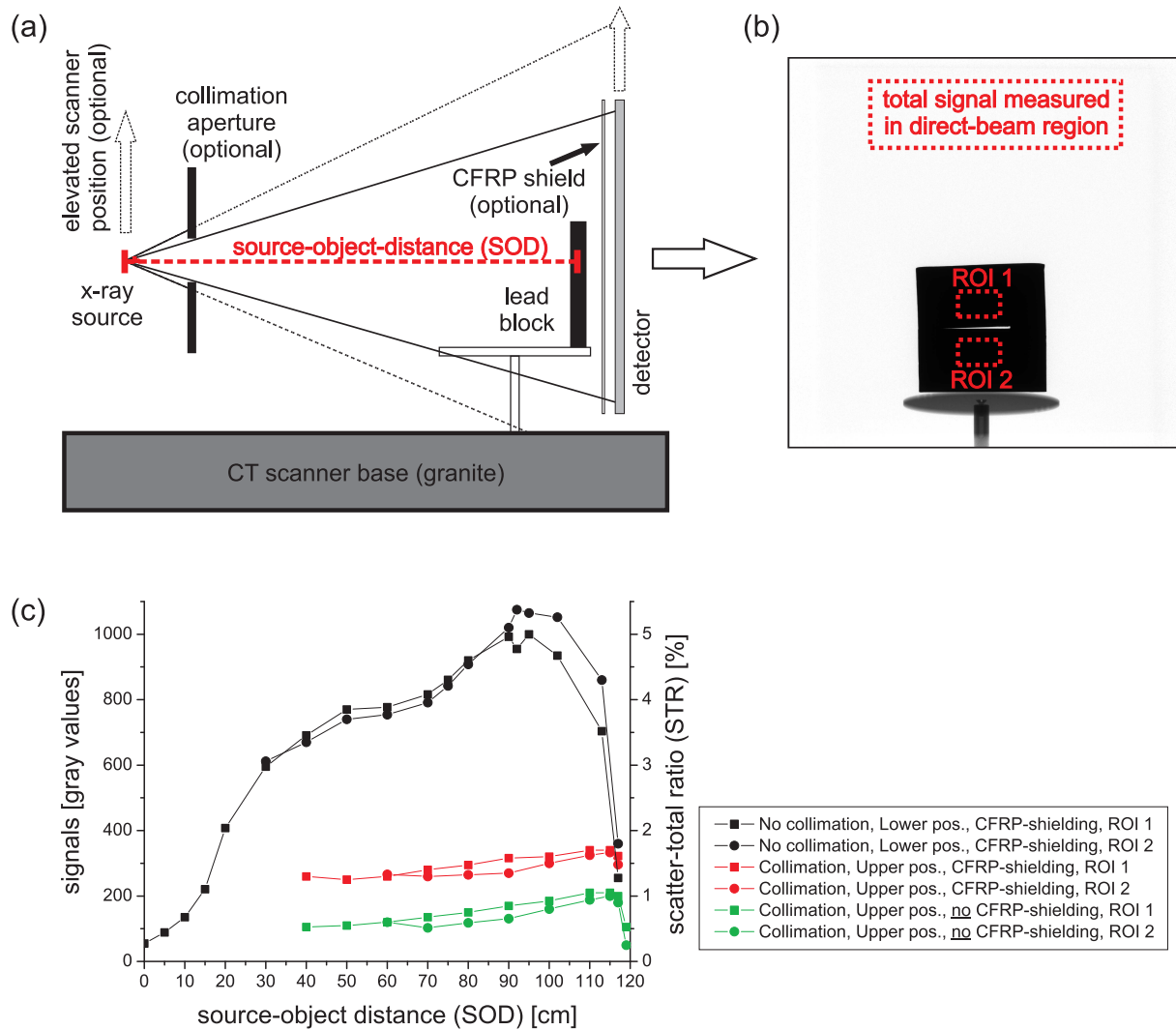
Figure 3.2: (a) Schematic view of experimental setup for demonstrating different steps to reduce environmental scatter. (b) Radiographic projection of lead block at source-object distance SOD = 117 cm with tagged ROIs. (c) Experimental results for signals measured in ROI 1 and 2 for three different CT scanner settings, cf. legend and details in the text.

of measurements is conducted without this CFRP shielding, however with the same parameters and settings as before. Measurement results are given as green curves in Fig. 3.2(c). Note that with these steps the STR could be reduced to about 1.0% and less for all SODs.

In principle, the proposed steps can be performed in order to reduce environmental scatter, however they are subject to experimental conditions. Nevertheless, we expect a scatter contribution from the environment I_{Env} to occur in experiments described in the following parts. Particularly, in situations when a scattering sample is placed into the CT setup, we expect multiple scattering involving both sample and surrounding structures which will lead to increased scatter contributions I_{Env} from the environment.

3.1.3 Detector-Internal Scattering and Veiling Glare

As a last contribution to the total scatter signal S from Eq. (3.3), we consider detector-related scatter and blur mechanisms I_{Det} and S_{Det}. Again, in a simple experiment, we examine the contribution of both. The experimental setup is illustrated in Fig. 3.3(a) whereas the hardware equipment is the same as described above in section 3.1.2. In a series of projections, collimators of different aperture sizes are employed in order to irradiate detector regions of different sizes. For smaller aperture sizes, we expect less detector-internal scattering contributing to the measured signal, and hence, lower signals than with larger aperture openings. In this specific setup without sample and with the measures taken that reduce environmental scatter as described in the last section, we have eliminated scattered radiation from the sample, I_{Obj}, and we may neglect environmental scatter I_{Env}. Thus, only secondary contributions that are detector-related are examined here.

Decreasing the aperture size such that its shadow shrinks from about $108 \times 90 = 9720$ pixels down to $4 \times 4 = 16$ pixels, we measure the signal in a small region at the center of the collimator's projected shadow. Experimental results are shown in Fig. 3.3(b). Note that the signal is rapidly decreasing as the aperture size approaches small openings of the order of a few pixels. In fact, we observe a signal drop of 22% for the smallest aperture size compared to the open field-of-view (FOV) signal at the same location on the detector plane when collimating apertures are omitted. On the other hand, the total open FOV signal is approached when the aperture size increases: irradiating an area of almost 10000 pixels, which represents 0.2% of the total detector sensitive area, constitutes 96% of the total open FOV signal already.

We assume that the true, unbiased signal is the one measured within a very small aperture shadow and that additional signal contributions in projections with larger aperture openings are due to detector-related scatter and blur mechanisms, cf. [PLB08]. From this perspective, the open FOV signal is too large by about 30% if the smallest aperture signal is considered to be 100% primary signal without additional scatter contribution.

In the indirect conversion process described in section 2.2.2, a number of different possible scatter and blur mechanisms have to be considered as responsible for the observed effect: First, incident X-rays may be scattered by any material that is in the vicinity of the detection layer, e.g. the detector housing, mountings, structures behind etc., or even by the detection layer itself. Furthermore, K-fluorescence X-ray photons may be reabsorbed at locations different than their origin, i.e. at the primary detection site. Analogous to
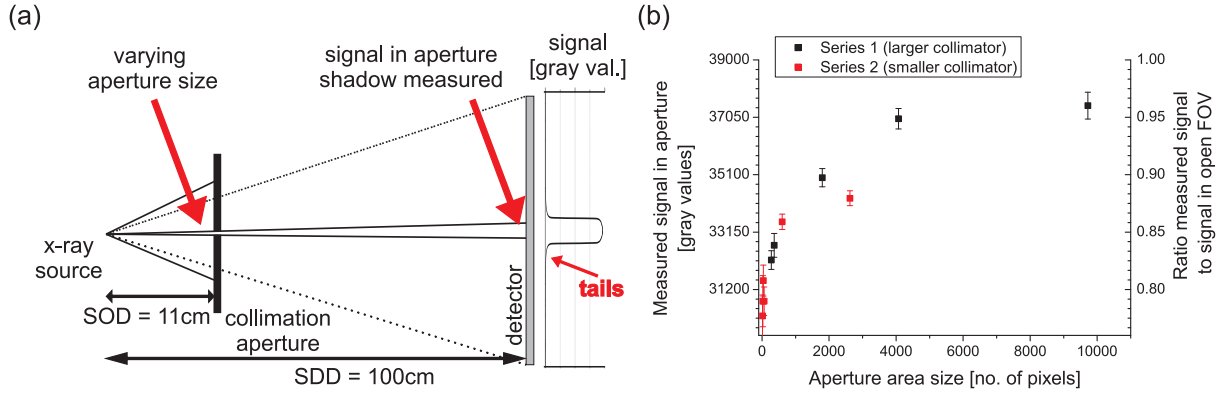
Figure 3.3: (a) Schematic side view of experimental setup for demonstration of the influence of the detector-related scatter component. In this setup, we assume that object scatter does not exist and environmental scatter is negligible. (b) Experimental results of measured signals in the aperture shadow for variable aperture sizes.

the above-mentioned X-ray scatter contributions I_{Obj} and I_{Env}, we denote these detector-related X-ray scatter and fluorescence contributions as I_{Det}. The resulting spatial blurring of (otherwise) sharp sample edges due to scatter has been studied before experimentally in Refs. [ZOE03; Bub+07] and theoretically in Ref. [HKG05], and for X-ray fluorescence in Ref. [Boo+99].

Second, after the X-ray photon has been converted to several thousands of photons in the visible spectrum, those may spread and further scatter optically which causes blurring, also known as veiling glare. Its magnitude mainly depends on the thickness of the detection layer and on the scintillation material characteristics (microstructured, powder, etc.), cf. section 2.2.2 and [Bad03]. The veiling glare is solely caused by photons in the visible spectrum. Hence, we separate it formally from the X-ray scattering mentioned before by denominating it as S_{Det}.

Third, even further sources of blurring exist as defined by Rowlands in Ref. [Beu00, p. 234–236]: geometrical and migration range of electron-hole pairs. These are considered as intrinsic sources of blurring. Geometrical blurring refers to the fact that inclined incident X-rays may be absorbed at different depths within the scintillation layer, and hence, give a different response on the surface. This effect depends on the angle of incidence and on the thickness of the scintillation layer. Blurring due to electron range results from electrons freed by radiation interaction and their subsequent migration through the medium depositing energy. However, their potential migration range is specified to be $10 - 30\,\mu\text{m}$ at $50 - 100\,\text{keV}$ in typical X-ray detection media [Beu00]. Since the width and height of a pixel in our experiment is $200\,\mu\text{m}$, we assume that the electron range is only of little significance here.

3.2 Demonstration of Scatter Artifacts by Model Simulation

Scattered radiation, whether it is originating from the sample, the environment, or from the detector material itself, respectively, represents a secondary signal contribution to the total detected signals in each projection. In radiographic projections, this merely reduces image contrast, since it contributes additively, cf. Eq. (3.2). However, it is well-known that scattered radiation represents a major source of image degradation in CT resulting not only in a loss of contrast, but also in a number of other artifacts. Their consideration is more complicated than in the case of a 2D projection, as the log operation in the reconstruction process is non-linear (cf. section 2.2.3): $\log(P + S) \neq \log P + \log S$.

Thus, in this section, we demonstrate the different typical artifacts commonly encountered in both medical and industrial CT. For this purpose, we perform a model simulation in order to provide an ideal CT reconstruction free from any artifacts. We compare this with a CT reconstruction based on ideal projections where we deliberately add a constant offset representing the scatter contribution. Hereby, an exclusive study of scatter-induced artifacts in the CT volume is made possible while all other sources of artifact, particularly beam-hardening artifacts which have similar appearance, are excluded by the simulation settings chosen accordingly.

3.2.1 Model and Simulation

We perform a <u>di</u>rect-<u>ray</u> <u>sim</u>ulation (DRASIM[1]) where a simple geometrical object, e.g. a rectangular solid, is virtually transmitted by calculating the X-ray attenuation according to Eq. (2.1) along irradiated beam paths within the object. Irradiated path lengths are geometrically calculated as direct-rays by the software, and linear attenuation coefficients $\mu(E, Z)$ are taken from a database[2] that is provided with the simulation package.

Resembling a typical scenario in industrial CT, we create a model for the simulation as follows: A cone-beam CT (CBCT) setup is modeled with an ideal X-ray tube, i.e. the focus is infinitesimally small and the tube is emitting monochromatic radiation with a photon energy[3] of $E_{\mathrm{mono}} = 130\,\mathrm{keV}$. Thereby, we eliminate the effect of beam-hardening. Additionally, noise is disabled as the simulation exactly calculates expectation values based on irradiated path lengths. The flat-panel detector which has dimensions of $40.96 \times 40.96\,\mathrm{cm}^2$ and 2048×2048 pixels, is located at a source-detector-distance (SDD) of $90\,\mathrm{cm}$. Furthermore, the detector is idealized too, i.e. it has a detective quantum efficiency (DQE) of 100% and neither internal scattering nor blurring. The tomographed object is defined as rectangular solid made of aluminum (Z=13) with dimensions $8 \times 4 \times 18\,\mathrm{cm}^3$. We insert some structures in three different transversal planes of the rectangular solid (cf. Fig. 3.4), i.e. thin slits aligned frontally and laterally, as well as holes, by declaring them geometrically as regions within the object where X-rays do not interact with matter

---

[1]Siemens simulation package for direct-ray simulation of radiographic projections, cf. [Sti93].

[2]DRASIM uses the EPDL97 database from the Lawrence Livermore National Laboratory (LLNL), cf. [CHK97].

[3]$E = 130\,\mathrm{keV}$ corresponds approximately to the center-of-mass energy of a $225\,\mathrm{kVp}$ spectrum filtered with $3\,\mathrm{mm}$ of copper that is typically used in industrial CT.

(virtual vacuum). The object is virtually placed at a source-object-distance (SOD) of 75 cm and rotated, while a total number of 1080 projections are simulated.

In a first CT reconstruction based on the simulated projections, an ideal CT volume is reconstructed. In a second run, we add a constant offset of 3000 gray values to each projection which represents the simplest form of scatter contribution. This corresponds to a scatter-primary-ratio (SPR) of 10% in direct-beam regions, which is realistic in magnitude and comparable to ratios measured in the experiments described in chapter 4 and 5.

3.2.2 Simulation Results

Figure 3.4 shows axial CT slices extracted from the two simulated CT volumes with and without scatter contribution as well as corresponding CT slices from a real scatter-contaminated CT, which is described in more detail in section 5.6. The top row shows three CT slices from the ideal CT, i.e. the CT where ideally simulated CT projections were used and no additional scatter offset was added. The middle row depicts simulated CT slices from the reconstructed volume where projections with constant scatter offset were used. Thereby, scatter-related artifacts are visible here which shall be discussed in the following. For comparison, the bottom row in Fig. 3.4 shows CT slices from a real CT where scattered radiation and other secondary signals result in scatter artifacts that are very similar to those encountered in the simulation (middle row). Even though the simulated CT is different from the real CT in quite a few parameters (spectrum, detection characteristics, etc.), their similarity is remarkable, indicating that mainly the scatter offset is relevant to the appearance of scatter artifacts and that other parameters are less dominant.

Let us discuss the most prominent scatter artifacts typically encountered in industrial CT, always referring to the middle row in Fig. 3.4 and comparing this to the ideal CT in the top row:

Cupping artifact The so-called cupping artifact is noticed, i.e. inhomogeneities in regions of homogeneous material. Note that in all scatter-contaminated CT slices central regions within the object appear darker while boundary regions are very bright at half of the side length. In Fig. 3.5, this gray-value difference can also be found quantitatively in the corresponding line profiles (red and black curves) for the scatter-contaminated CTs while the ideal CT shows an almost perfect rectangular profile here (green curve). In the latter, the small overshoots noticed at some of the sharp edges of the slits represent an artifact that is due to the high spatial image frequencies encountered in a perfect simulation setting. Signals including these high frequencies are band-limited when filtered in the reconstruction process and this may cause ringing artifacts.

Cupping artifacts may arise due to the scattered radiation, but also due to beam-hardening effects, cf. section 2.3.1. In fact, both artifacts – although different in their physical origin – lead to measured signals that are larger than they should be according to the attenuation law given in Eq. (2.1). Hereby, inconsistencies arise in the angular projection sampling as the linearity between measured projection integral p and penetrated path length integral in Eq. (2.27) is no longer existent. In addition, a difference
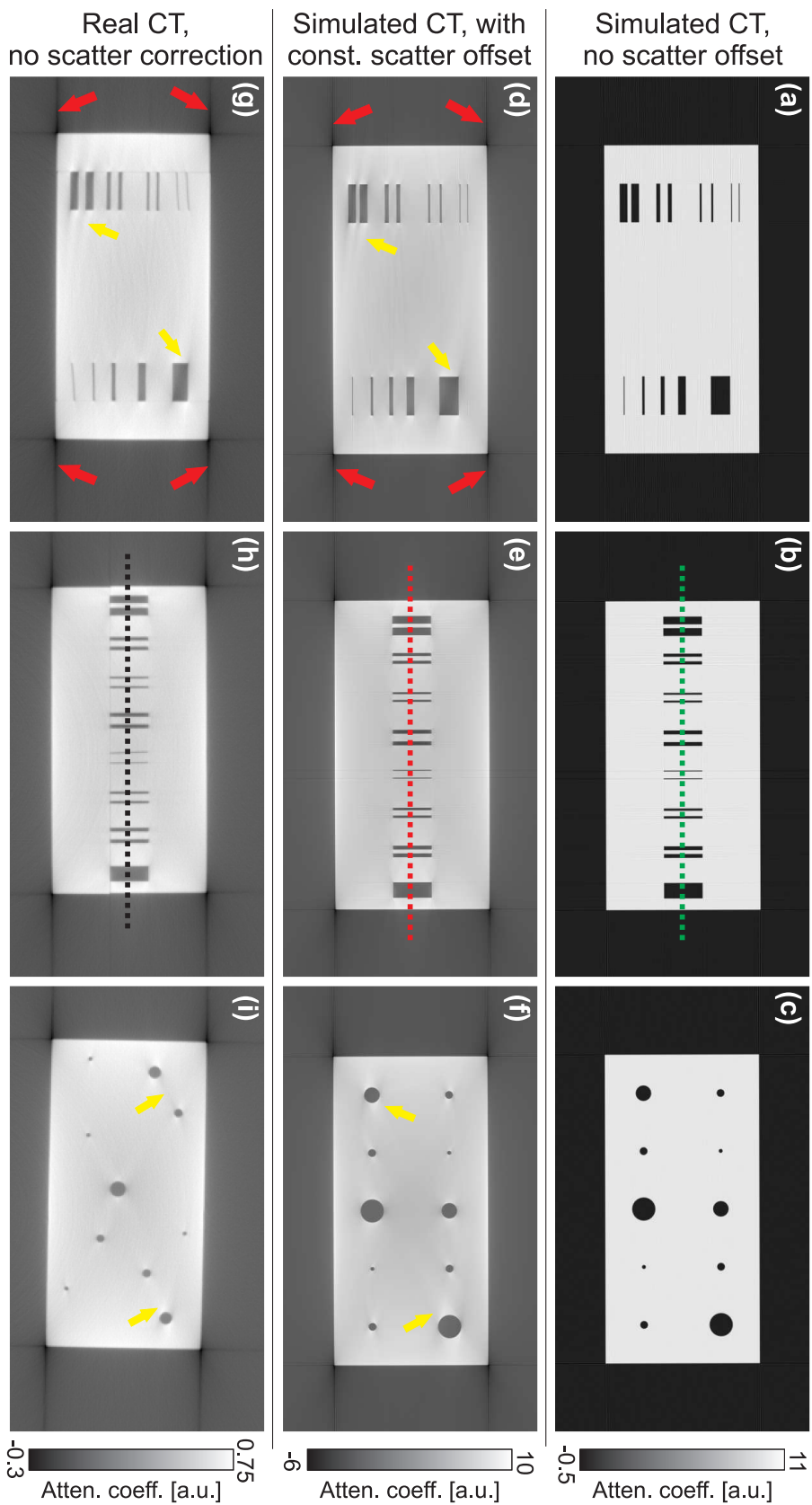
Figure 3.4: Demonstration of scatter artifacts. (a)–(c): CT slices from simulated CT without scatter offset (ideal CT). (d)–(f): Simulated CT slices where a constant scatter offset was added to each projection, resulting in artifacts. (g)–(i): CT slices from a corresponding real CT are given for comparison, showing very similar artifacts as the simulated CT. Arrows and markers indicate different types of artifacts, see text for details.
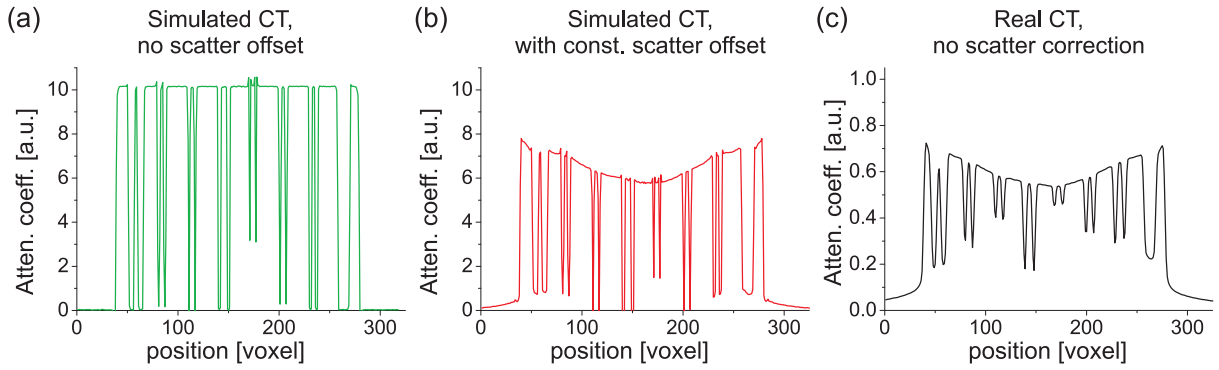
Figure 3.5: Line profiles for the CT slices shown in Fig. 3.4 in the middle column, as indicated. (a) The ideal CT shows an almost perfect rectangular profile with small overshoots, see text for details. (b) A strong cupping artifact and reduced contrast at the slits are noticed in the line profile of the simulated CT with constant scatter contribution. Also, the background is non-zero and rises slowly towards the sample edge. (c) The corresponding line profile from a real CT is given for comparison. Similar artifacts appear as in the simulated CT.

arises between central regions of the object where beam path lengths are longer than for regions near the object boundaries where beam path lengths are short. For the first, the effect of non-linearity is stronger since signals are smaller here. In the reconstruction process, this leads to the observed cupping artifact.

Loss of contrast is noticed at slits and holes in the scatter-contaminated CT slices. This can be seen in Fig. 3.4, but also quantitatively in the corresponding line profiles shown in Fig. 3.5. Scatter introduces loss of contrast in the CT scan process at the stage of CT projections already. Here, a constant offset is added and leads to a loss of contrast in the projections that evolves to the observed final loss of contrast in the CT volume. Loss of contrast is a very critical scatter artifact, particularly in nondestructive testing (NDT), since tiny cracks and flaws which are of low contrast naturally become even more difficult to be detected and visualized.

Streaks represent another scatter artifact and hamper a uniform appearance of otherwise homogeneous material, cf. regions highlighted by red and yellow arrows in Fig. 3.4. Here, dominant dark spikes (red arrows) along the long sides of the object elongate to the outside and disturb the corner regions. Also inside the object, we notice bright and dark streaks starting from high-contrast details, i.e. holes and slits, indicated by yellow arrows. Streak artifacts may lead to misinterpretation and they may superimpose true defects.

Effect on dimensional measurements As a result of the cupping artifact and the artifact-affected corner regions, dimensional measurements that are routinely performed in industrial CT (cf. section 2.2.4) show deviations from true dimensions that we defined for the simulated object and which can be measured in the ideal CT. In our example,

the outer dimensions of the rectangular solid object severely deviate from their correct values as the detected object surface (after the calibration step, cf. section 2.2.4) gets rendered bulbous. In general, scatter artifacts hamper correct and reliable dimensional measurements in industrial CT.

Incorrect CT numbers are also a consequence of the cupping artifact, i.e. reconstructed attenuation coefficients differ from their true values. This is of major importance for medical diagnosis where the so-called CT numbers or Hounsfield units serve as a basis for interpretation and quantitative analysis. In medical and industrial CT as well, it is difficult to set the grayscale scale appropriately in order to visualize fine details because the intensity varies strongly over the region of interest.

Noise represents another negative aspect of the scattered radiation in CT that is not an artifact by itself. It is established understanding that scattered radiation enhances the noise in each projection and thus may affect low-contrast detectability [End+01; ZWX09]. When scatter is corrected by any of the post-processing methods discussed in section 3.3.2, noise is left uncorrected and the signal-to-noise ratio decreases even further as the estimated scatter function is subtracted from the original CT projection.

Returning to the CT slices shown in Fig. 3.4(g)–(i), revealing scatter artifacts in a real CT, we will revisit this exemplary CT in section 5.6 and demonstrate how scatter artifacts can be corrected. The ultimate goal is to attain a corrected version that resembles the idealized CT without scatter artifacts depicted in the top row in Fig. 3.4.

3.3 Review of Existing Methods for Scatter Suppression and *a posteriori* Correction

From the beginning of clinical CT scans in the early 1970's, almost another ten years passed until scattered radiation as a source of CT artifacts became an active topic in scientific research. In 1982, almost simultaneously, three scientific articles were published dealing with the issue of how scattered radiation affects CT image quality [JY82; JS82; Glo82]. Reference [Glo82] was the first to identify the scatter-to-primary ratio (SPR) as crucial quantity that determines the nature and intensity of scatter artifacts. In the following years, up to the present day, numerous articles have been published, mostly for medical CT, that propose various measures for suppression of scattered radiation reaching the detector, and for comprehensive *a posteriori* correction of scatter-related artifacts, respectively. With this distinction of being either a suppression technique or a correction method, we review the most important ones in the following. We also include techniques and methods that were initially proposed for CT systems employing a line detector (or multi-slice at most) rather than flat-panel systems. In these cases, we will discuss their possible migration to CBCT systems and resulting consequences thereof.
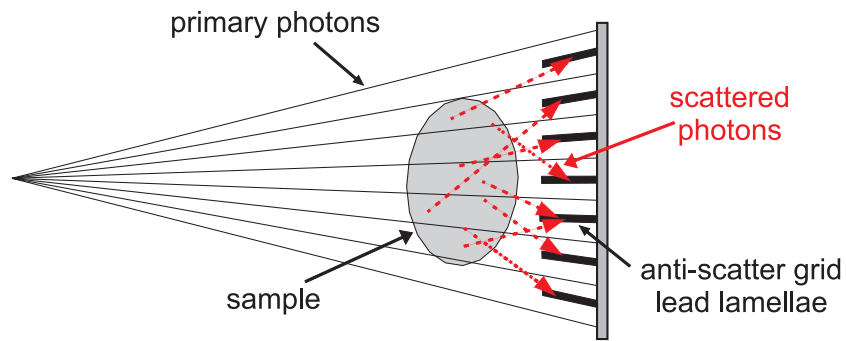
Figure 3.6: Schematic illustration of anti-scatter grid with focused lamellae of highly absorbing material, e.g. lead. Scattered photons are hampered from reaching the detector plane as they have different angles of incidence than primary photons. This reduces scatter contribution on the detector plane.

3.3.1 Suppression Techniques

First, suppressing or at least reducing the amount of scattered radiation reaching the detector can be achieved by very simple means, e.g. by increasing the distance between the scattering sample or patient, respectively, and the detector plane. This technique is known in the literature as air gap [SF85; Nei92] and is very efficient as radiation intensity behaves proportional to $1/r^2$ where r is the distance between radiation point source and detection site. However, when increasing the air gap by relocating the detector further afar from the scattering sample, this also reduces the primary radiation intensity.

In section 3.1.2 describing the environmental scatter contribution, we found that an elevated position of tube, sample and detector from the scattering CT scanner base reduces scatter. This is equivalent to an increased air gap between detector plane and environmental structures beneath. In contrast to air gaps that increase the source-detector-distance (SDD), the air gap by an elevated scanner position does not result in a decrease of primary radiation intensity since the SDD remains the same.

A second suppression technique is the anti-scatter grid that is installed after the sample/patient and right in front of the detector, see Fig. 3.6. Anti-scatter grids are standardly fabricated as 1D lamellae of highly absorbing material (lead or gold) that are aligned in parallel and optionally each individually inclined, such that the majority of primary photons may pass while scattered photons are rejected, see Fig. 3.6. They are routinely used in conventional [CHD85; Bar91; Nei92] and digital radiography [CLW90] and lead to an improved SNR there.

However, their migration to CBCT, both medical and industrial, has to be evaluated critically. Recent publications that studied the use of standard fluoroscopy anti-scatter grids in medical CBCT scenarios [Sie+04; KK07; Wie07] came to the conclusion that – only under specific circumstances – they may reduce scatter artifacts to a certain degree but cannot eliminate them. A successful migration to industrial CBCT seems to be even more unlikely when considering that usually higher energies are used in industrial CT which render the lamellae of the anti-scatter grid less effective in absorbing scattered radiation. Also, the scanning geometry is fixed when a focused anti-scatter grid is used.

This represents a drawback as it reduces the flexibility which is of great importance in many industrial CBCT scanners.

Third, it is possible to employ beam-shaping attenuators, so-called bow-tie filters, in order to reduce the amount of scatter. Mainly used in medical CT, they are built in the form of a bow-tie based on the objective of achieving uniform fluence through a – more or less – cylindrical object (patient's head or torso) by attenuating peripheral radiation more than central radiation. This reduces the dose delivered to the patient as well as emergence of scattered radiation [Gra+07]. In industrial CT, where samples are less often of uniform (cylindrical) shape, the benefit of using bow-tie filters is yet unresolved.

Again, while the discussed techniques may be able to reduce the amount of scatter that is detected, they do not eliminate it completely. Therefore, in the following we will consider correction methods which offer a complete elimination of scatter artifacts in theory.

3.3.2 *A posteriori* Correction Methods

By contrast, scatter correction methods can be applied *a posteriori* to subtract the scatter contribution from the total detected signal. If performed correctly, this subtraction represents an overall correction of scatter as its contribution to the total signal is effectively reversed, cf. Eq. (3.2). In this case, the corrected total signal is linear to the incident primary radiation. Thus, a comprehensive scatter correction requires precise knowledge of the scatter distribution in each projection. The scatter distribution can either be estimated by software-based methods or it can be measured experimentally.

Several scatter estimation methods exist which can be divided into calculations based on analytical scatter models [BS88; SB88; HKK91; OFKR99], Monte-Carlo simulations [Kal81; CD83; CB04; Mic+07], and hybrid methods [KRK06]. Analytical models rely on an approximated, global model which describes the physical scatter buildup as consistent as possible with experimental data. Point-spread functions (PSF) describing the scattering of a pencil beam are simulated or measured, and subsequently they are convolved with the weighted measured projections [OFKR99] or used for deconvolution of projections [SB88]. Usually, the models are adopted to a specific (medical) imaging task by setting their relevant parameters (tube voltage, object size, air gap distance from object to detector, etc.) according to experimental [HKK91] or simulated scatter data [BS88]. Analytical methods may reduce scatter artifacts – however, they fail to provide entirely correct scatter estimates with respect to all possible CT scenarios.

Monte-Carlo simulations are based on repeated tracking of individual photons undergoing scattering events. While presenting a powerful tool to explore scattering development (scatter production and buildup), the drawback of Monte-Carlo simulations lies in the statistical nature of the simulation. A high number of photons have to be simulated, involving time-consuming computation, in order to yield a sufficiently smooth scatter image, which is a prerequisite for an accurate scatter correction. A reduction of the computational effort can be achieved by only simulating a small number of photons and consecutively denoising scatter images using the Richardson–Lucy algorithm [CB04]. Since the actual electron distribution in 3D is initially unknown, it is proposed to use MC simulations in an iterative manner, i.e. to start the simulation with an object model taken from a first reconstructed CT volume that is scatter-contaminated and then iterate

through a number of reconstructions where scatter-corrected projections are subsequently used [ZB06]. Monte-Carlo based scatter correction for diagnostic radiology is investigated in Refs. [Kal81; CD83], for medical cone-beam CT (CBCT) in Refs. [CB04; ZB06], and for industrial CBCT in Ref. [Mic+07].

Hybrid methods aim at reducing computational efforts by calculating first-order scatter deterministically, which is much faster than a Monte-Carlo simulation. Scattering of higher order is either assumed to have spatially uniform distribution and, therefore, is taken into account by a uniform background, or it is estimated by a Monte-Carlo simulation using a small number of photons [KRK06].

Apart from the software-based approaches, a few experimental methods exist which aim at measuring the scatter signal at a number of sampling points. A more thorough discussion of these will follow in the next two chapters.

Chapter 4

Scatter Correction by Use of Beam-stop Array and Beam-hole Array

In chapter 3, we have demonstrated that secondary signals such as scattered radiation degrade CT image quality by introducing several scatter artifacts. We have also given a brief review of existent methods for *a posteriori* corrections of scatter artifacts, i.e. after scattered radiation has contaminated the CT projections. As described, besides purely software-based approaches there exist a few experimental methods which directly measure the scatter signal at a number of sampling points. Since the software-based approaches rely crucially on a realistic modeling of all scatter sources in order to yield accurate scatter estimation, the measurement-based methods are more appropriate for our purpose of initial scatter correction in CBCT.

Thus, in this chapter, two of the measurement-based methods are presented and compared to each other experimentally: the beam-stop array (BSA) and a complementary method using apertures which we call beam-hole array (BHA) method. The BSA method uses beam-stoppers to block primary radiation, thereby secondary signals can be measured in their shadows directly. The BHA method is complementary to the BSA method as it aims at measuring the sampled primary signal in a first projection by using a lead sheet with small apertures and the total signal in a second, open-field projection. The scatter signal can be determined indirectly by subtraction. While the BSA method is considered an established scatter correction technique, the BHA method is less popular and has been used only in a different form for densitometric measurements so far. This motivates a thorough experimental comparison of both methods.

In section 4.1, the concepts of both the BSA and BHA method will be presented from a theoretical point of view. Section 4.2 will describe two comparison measurements of BSA and BHA where geometric effects and scatter-to-total ratios are investigated. Besides the comparison itself, these initial measurements reveal scatter signals exhibiting strong detector-internal scatter contributions. In section 4.3, the proposed beam-hole array method is successfully applied to a strongly scattering industrial sample. Finally, section 4.4 discusses differences between BSA and BHA method and evaluates their performance for different possible application scenarios.

4.1 Background of Beam-Stop Array and Beam-Hole Array Methods

As described in section 3.1, the total measured signal $T(n)$ in each pixel n is the sum of the primary signal $P(n)$, that carries the desired information, and of secondary signals, cf. Eq. (3.3), which together are expressed by a single secondary quantity $S(n)$:

$$T(n) = P(n) + S(n) \, . \tag{4.1}$$

While in chapter 3 we have strictly distinguished between different origins of scattered radiation and of other secondary effects (e.g. detector-internal effects), by using the methods presented in this chapter, we only measure the total sum of all secondary effects. Thus, we denote the total sum by S and term it secondary signal or scatter signal interchangeably if not noted otherwise.

Looking at Eq. (4.1), it can be inferred how the scatter signal S can be measured: A first and direct way is to blind out the primary signal P by appropriate means. This is realized with the beam-stop array (BSA). Representing a second possibility to get hold of the scatter signal S indirectly, we may measure total signals and primary signals separately and then subtract them from each other to yield S, as it is pursued in the beam-hole array method (BHA).

4.1.1 Beam-Stop Array

In the beam-stop array (BSA) method, highly absorbing elements, such as small lead cylinders arranged on a regular grid, are placed between source and object as illustrated in Fig. 4.1. Acting as beam-stoppers, total attenuation of the primary signal behind these cylinders is assumed[1]. $P(n)$ from Eq. (4.1) vanishes for shadowed pixels n and, for those, the detected signal only measures the secondary signal S comprising all secondary effects at once. More specifically and referring to Eq. (3.3), scattered radiation originating from both the object and environmental structures, as well as from detector-internal scatter effects (X-ray scatter and light spread) together give rise to the signal measured in the shadows of the beam-stoppers (Fig. 4.1). The BSA method represents a direct measure of the scatter signal $S_{\mathrm{BSA}}(n)$ at a number of sampling points.

For CT, a second projection without the BSA is necessary to obtain the total image consisting of scatter plus primary image. Beam-stop based scatter correction is a standard method for experimental scatter correction and has been established for a long time. One of the first publications that systematically analyzed scatter-to-primary ratios in medical CT scanners already embarked on this technique [JY82]. Regarding more recent publications investigating the BSA method, we refer to [NTC04] for the medical field and to [PLB08] for industrial CT.

---

[1] Here, we neglect diffraction effects, such as e.g. the Poisson spot, a bright spot which can be observed behind an ideal beam stopper for wavelengths in the visible spectrum due to diffraction at the beam stopper. In our case using X-rays, the wavelengths are very small ($\lambda \approx 10^{-11}\,\mathrm{m}$) compared to characteristic sizes of the object, such as the diameter d of the beam stopper ($d \approx 1\,\mathrm{mm}$). This is expressed by the Fresnel number $F = \frac{d^2}{L \cdot \lambda} \approx 10^5$ where L is the distance between object and detector ($L \approx 1\,\mathrm{m}$). For Fresnel diffraction, $F \gtrsim 1$ needs to be fulfilled, while geometrical optics are valid for $F \gg 1$.
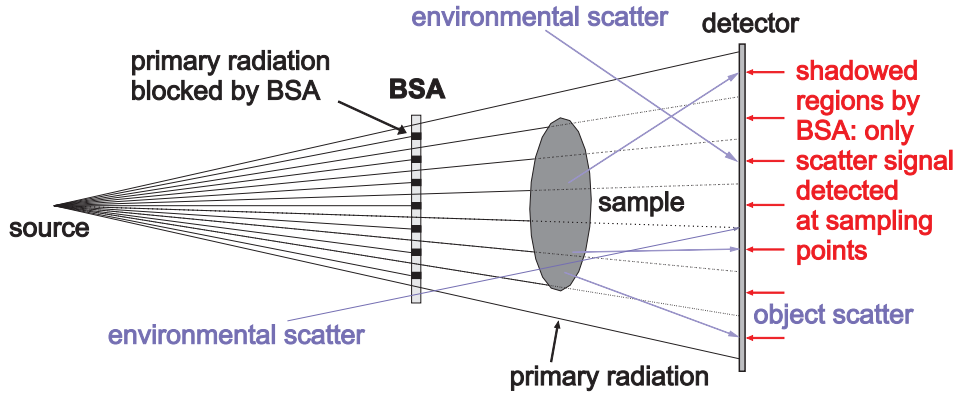
Figure 4.1: Schematic illustration of the working principle of scatter estimation with the beam-stop array (BSA). The BSA is placed between sample and source where it totally blocks incident primary radiation at a number of sampling points. Therefore, any signal detected in the shadows of the lead cylinders of the BSA is considered to be scattered radiation or detector-internal effects. As shown, scattered radiation can originate from the object, from the environment and from detector-internal X-ray scattering and light spread (not shown in this schematic). Altogether, this gives rise to the secondary signal S_{BSA} which can be measured at the given sampling points.

4.1.2 Beam-Hole Array

The beam-hole array (BHA) method is complementary to the beam-stop array method as it aims at measuring primary signals at given sampling points in a first projection and total signals in a second. It can be considered also as inverse technique to the BSA as the sampling of primary signals is achieved by means of a lead sheet with small apertures, i.e. the beam-hole array, placed in between source and object as shown in Fig. 4.2(a). The sample is only irradiated at very few and small spots. Therefore, almost no scattering occurs from the object and environmental structures. The same holds true for detector scatter events since most of the sensitive area of the detector is kept dark. In this configuration, only primary signals $P(n)$ are detected behind the apertures.

In a second projection without the BHA, the total signal T is detected, as illustrated in Fig. 4.2(b). Referring to Eq. (4.1), subtraction of P from T yields the scatter signal S_{BHA} at the given sampling points:

$$S_{\mathrm{BHA}}(n) = T(n) - P(n) . \tag{4.2}$$

The BHA method is considered an indirect method for estimation of secondary signals as it is a differential measurement. This technique has initially been explored in the medical field for densitometric measurements [MM98; ZMM99]. For medical diagnostics, the BHA is advantageous compared to the BSA method since it reduces the dose exposition to the patient. To the best of our knowledge, no publications exist which cover beam-hole array scatter correction in the industrial environment.

At this point, let us mention an important experimental difference between both methods. For the beam-stop array method, an acrylic plate (PMMA plate) serves as support for
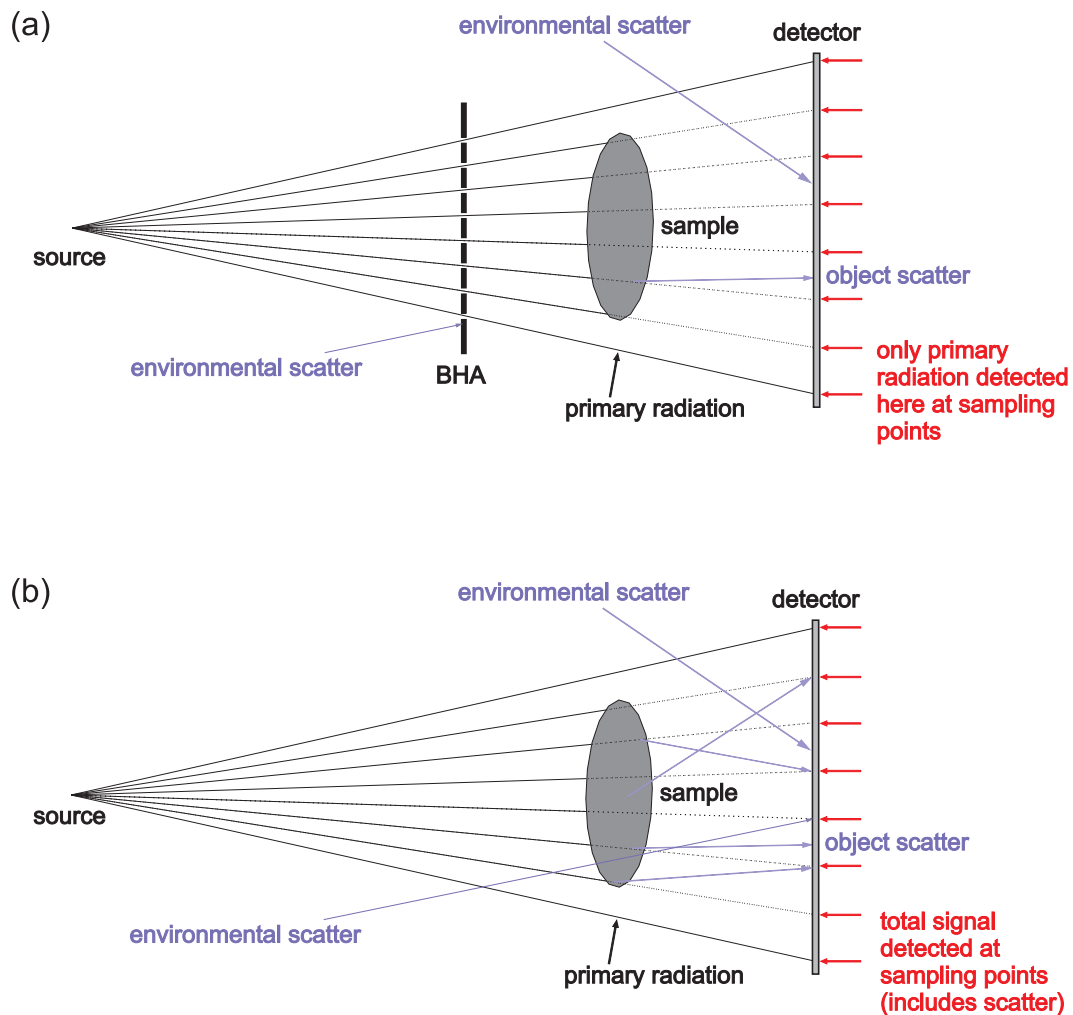
Figure 4.2: Schematic illustration for scatter estimation employing the BHA method: (a) In a first measurement with the BHA in place, almost all incident primary radiation is blocked except for very few and small apertures in the BHA. At these sampling points, it is assumed that only the primary signal is measured. In the first approximation, this is true, since in this configuration, both object scatter and detector-internal scatter effects are low due to the strongly reduced incident radiation. Environmental scatter, as illustrated, is also strongly reduced since most of it is blocked by the BHA. In order to estimate the scatter contribution at the given sampling points, (b) a second, open-field projection is necessary. Here, the total signal, consisting of scatter plus primary signal, is measured at the same points. Subtraction of the primary signal from the total signal then yields the scatter estimate.
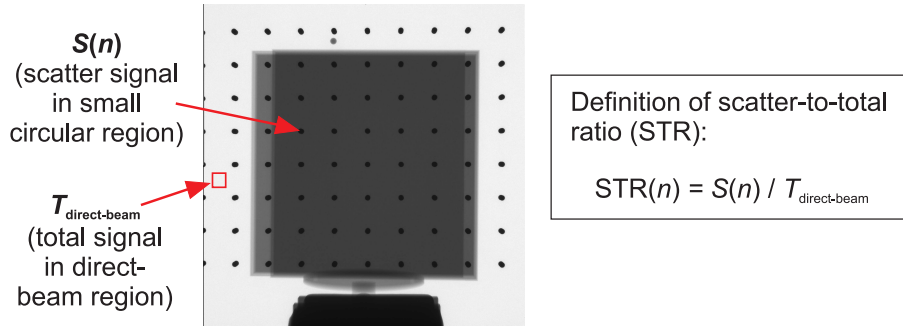
Figure 4.3: Definition of the scatter-to-total ratio STR(n) at pixel n, illustrated with the example of a beam-stop array projection showing a large-scale aluminum sample. For details see text.

the lead cylinders. This acrylic plate is fully irradiated, and hence, it presents additional material that absorbs and scatters X-rays. On the one hand, this leads to smaller primary, and consequently, total signals as compared to the beam-hole method where an acrylic support is not necessary. On the other hand, we expect an additional scatter contribution I_{PMMA} from the acrylic plate, extending Eq. (3.3) in case of the beam-stop method into

$$S_{\text{BSA}}(n) = c \cdot \{I_{\text{Obj}}(n) + I_{\text{Env}}(n) + I_{\text{Det}}(n) + I_{\text{PMMA}}(n)\} + S_{\text{Det}}(n). \qquad (4.3)$$

Taking into account the formerly mentioned effect of attenuation caused by the acrylic plate which is only present in one of the two methods, it is necessary to introduce a quantity that renders the comparison measurements described in section 4.2 independent of this effect. As illustrated in Fig. 4.3, we define the scatter-to-total ratio (STR), also denoted as scatter fraction, as the ratio of scatter signal S in a small circular region around pixel n on the detector to the total signal in an unobstructed-beam region (direct-beam), $T_{\text{direct-beam}}$, typically an outer region of the detector field where the object casts no shadow:

$$\text{STR}(n) := \frac{S(n)}{T_{\text{direct-beam}}}. \qquad (4.4)$$

With this definition, scatter fractions of both methods can be compared directly, even though their absolute signals (scatter and direct-beam) differ due to absorption and scattering by the acrylic plate within the beam-stop method which is not present in the beam-hole method.

4.2 Comparison Measurements between BSA and BHA

From a theoretical point of view, the BSA and BHA methods are complementary in respect of measuring total scatter contributions directly (BSA) and indirectly (BHA). If neglecting the additional PMMA plate used within the BSA method, both methods theoretically should yield equivalent scatter data. In this section, we put this assumption to the test in two comparison measurements and we will learn about specific differences between the two methods.

4.2.1 Experimental Setup

4.2.1.1 Imaging System Specifications

Our cone-beam CT setup consists of an X-ray tube, a sample rotation stage and a flat-panel detector (FPD). A photograph of the scanner setup is shown in Fig. 2.9(e). The X-ray source is a micro-focus transmission tube, model XT9225-TED manufactured by Viscom AG (Hannover, Germany). It is operated at $220\,kVp$, $320\,\mu A$ current, and with prefilters of $3\,mm$ copper and $0.5\,mm$ tin employed in order to harden the spectrum. In this configuration, the focus of the tube is below $10\,\mu m$ in diameter.

The flat-panel detector, a PerkinElmer XRD1621 AN14, is equipped with a DRZ-Plus ($Gd_2O_2S{:}Tb$) scintillation screen; it has a resolution of 2048×2048 pixels with $200\,\mu m$ pixel size. The image is encoded in 16 bit gray values. Frame times amount to $1000\,ms$. The acquired images are all corrected for defect pixel and dark current as well as detector- and beam non-uniformity. The latter two are known as offset and (multi-)gain correction; all corrections are processed by the frame grabber board.

Additionally, X-ray dose is measured for each projection in both beam-hole measurements (open-field and with BHA) with a dosimeter (Diados T11003, PTW Freiburg, Germany) installed between source and BHA, but outside the field of view. This is necessary in order to detect fluctuations in the X-ray tube output and to compensate for them when subtracting the primary from the total signal in the BHA method. Therefore, all sampled measurements are normalized to an average dose. Any uncompensated fluctuation would lead to a deviation in the estimated scatter contribution.

4.2.1.2 Definition of BSA and BHA

In our setup, we use a commercially available beam-stop array produced by QRM (Quality Assurance in Radiology and Medicine, Möhrendorf, Germany). Figure 4.4(a) shows a photograph of the BSA. A matrix of 8×10 parallel aligned lead cylinders with an interspacing of $20\,mm$ is pressed into drilled holes in the support, a $240 \times 240\,mm^2$ acrylic plate of $6\,mm$ thickness. The lead cylinders are $3\,mm$ in diameter and also $6\,mm$ long, which yields an attenuation factor of 5×10^{-3} for $220\,keV$ X-ray quanta [Ber+10]. When the BSA is used for scatter correction in a complete CT, an acrylic plate without cylinders of same thickness has to be used in the second CT scan where the BSA is absent (normal CT projections). This becomes necessary as the acrylic plate of the BSA absorbs and scatters X-rays itself and those conditions have to be reproduced in the second scan.

A Monte-Carlo simulation has been conducted to quantify attenuation and scattering of an acrylic plate with the specified dimensions placed $20\,cm$ in front of the detector. All other X-ray parameters were chosen as specified in section 4.2.1.1, including a polychromatic filtered X-ray spectrum. The acrylic plate was the only object included in the scenario. For the central detector region, where simulated object scatter is maximal (section 3.1.1), the attenuation amounts to 10.0% and scatter contribution results in a scatter-to-primary ratio (SPR) of 2.7% and a scatter-to-total ratio (STR) of 2.6%.

As depicted in Fig. 4.4(b), the beam-hole array is a $6\,mm$ thick plate of lead manufactured to order with apertures arranged in the same way as the lead cylinders are on the beam-stop array: apertures are also $3\,mm$ in diameter and their spacing amounts to $20\,mm$. For comparability, the total size of the BHA is the same as the BSA's.
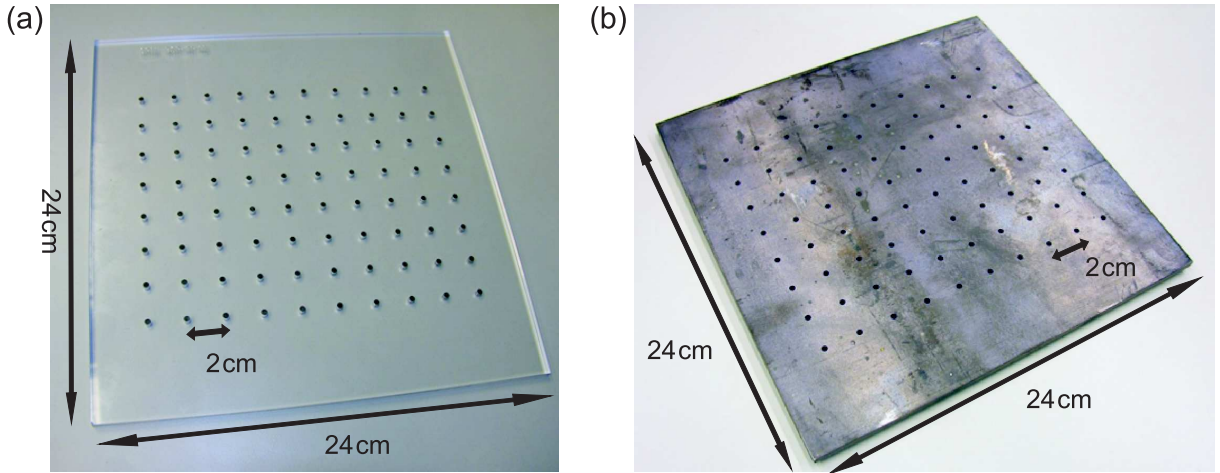
Figure 4.4: Photographs of (a) the beam-stop array (BSA) and (b) the beam-hole array (BHA). Both have the same dimensions and 8×10 parallel aligned cylinders (BSA) and apertures (BHA), respectively, representing the sampling points.

Attention has to be paid to dimensions and interspacing between lead cylinders and apertures, respectively, as well as to their number [ZMM99]. The reason is that the beam-stoppers (BSA) shall not block too much of the incident radiation since this results in less radiation irradiating the sample, thus to less scattering, and hence, to underestimation of scatter. This applies to aperture sizes within the BHA method analogously. In our investigations, the total shadowed area by the BSA lead cylinders amounts to less than 1.5% of the total sensitive area of the detector in a typical CT situation, so underestimation of scatter in this respect is negligible. Analogously, this is true for the BHA.

4.2.2 Experimental Investigations and Results

4.2.2.1 Comparison Measurement without Sample

In the following initial comparison of both methods depicted in Fig. 4.5, no other object apart from beam-stop and beam-hole array, respectively, is imaged. At first, the BSA is placed at a source-to-object distance (SOD) of 50 cm with the detector at a source-to-detector distance (SDD) of 100 cm and an image is taken (Fig. 4.5(a)). Note that, in this configuration, the outermost lead cylinders are traversed by X-rays with a tilt angle of 12° and thus will be imaged tilted and with a bigger shadow than the central cylinder. Exactly the same parameters, including SOD and SDD, are used in the projection with the beam-hole array (Fig. 4.5(b)) and the corresponding open-field projection. Additionally, X-ray dose is measured for each projection with a dosimeter as described in section 4.2.1.1. For both methods, the scatter-to-total ratio (STR, Eq. (4.4)) is calculated. In this step, the scatter signal S is determined by taking the mean gray value in a small circular area with a diameter of 10 pixels in the shadow of a cylinder or aperture, respectively, whereas the total incident signal is taken as mean gray value in an open-field region. Measured STRs for each cylinder and aperture are reported in Fig. 4.5(c), where the numbering
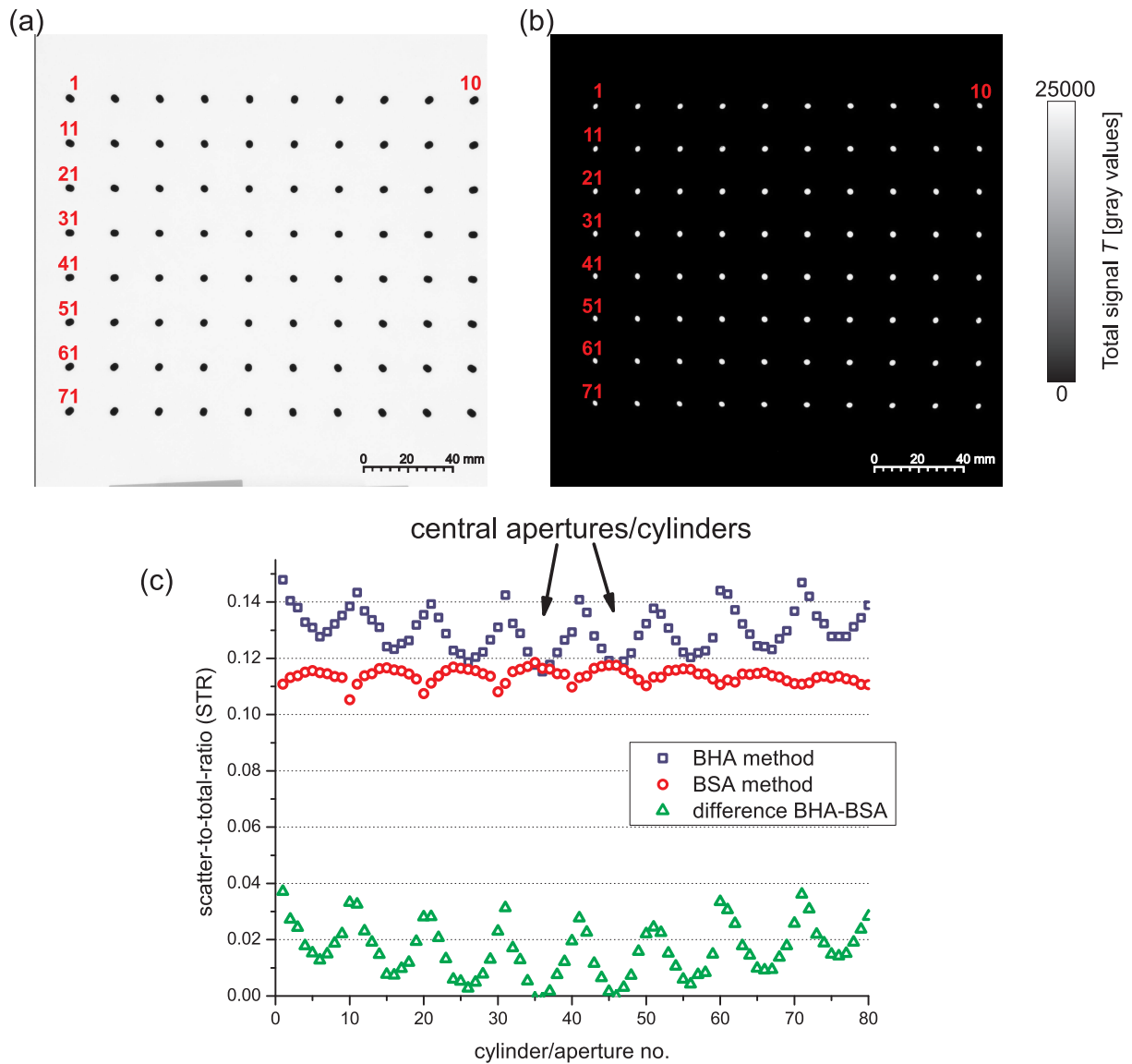
Figure 4.5: Open-field projections with (a) BSA and (b) BHA. Off-centered lead cylinders are traversed by X-rays under a tilt angle and their shadows become larger while corresponding aperture shadows become smaller. This can be clearly seen at outermost cylinders (a) and apertures (b). (c) BSA and BHA methods are compared without any sample: The STRs are reported for each BHA aperture and each BSA cylinder (numbering as above). For central apertures and cylinders, STRs of both methods are approximately the same. Off-centered apertures exhibit higher STRs than their BSA counterparts which is explained in the text.

is as given above in panels (a) and (b). The two measurements show that scattering occurs and amounts to 10–15% of the total incident signal, even in this situation where no sample is imaged.

4.2.2.2 Comparison Measurement with Aluminum Sample

In a second comparison measurement, the scatter-total ratios (STRs) of both methods are examined in an imaging situation with a large-scale sample. Figure 4.6(a) shows the first projection of the sample plus beam-stop array. The dimensions of the aluminum block are $185 \times 185 \times 40 \, \mathrm{mm}^3$; notches are laterally cut. In this comparison measurement, the object is at SOD = 65 cm, the detector at SDD = 100 cm, and the BSA/BHA is placed right in front of the object, i.e. at $x_{\mathrm{BSA/BHA}} = 55$ cm, as shown in Fig. 4.6(a) and (b). The scatter measurements are conducted in the same way as described above. In Fig. 4.6(c), the STR is reported for all cylinders and apertures within this first projection (projection angle 0°). We find a different behavior of STRs for sampling points that are (i) shadowed by the sample and those that are (ii) direct-beam. In the first case, BSA-measured STRs are higher than those from BHA measurements, while in the second case, it is vice-versa, i.e. BHA-measured STRs are greater than BSA-measured ones.

Thus, we conduct a study of the STRs behavior for two exemplary sampling points over the course of a complete rotation, i.e. the object is rotated and a total number of 360 projections are recorded in 1°-steps. The results are shown in Fig. 4.7 where exemplary sampling points are highlighted and the axis of rotation indicated in panel (a). Sampling point no. 1 is the outermost, top-left sampling point which is in the direct-beam (unobstructed incident radiation) in all 360 projections. On the other hand, sampling point no. 41 represents the central cylinder and aperture for both the BSA and BHA method that is permanently covered by the projection of the sample. For these two sampling points, STRs are plotted over the course of 360 projection angles as displayed in panels (b) and (c), respectively.

4.2.3 Interpretation

Referring to the results from the comparison measurement without sample displayed in Fig. 4.5, the dependence of the scatter-total ratio (STR) on shadow size of the aperture/cylinder can be clearly recognized. For the central apertures (BHA) and cylinders (BSA), i.e. no. 35 and 45, the cast shadows are of the same size. In this case, both methods yield nearly the same STR as it is also expected from a theoretical point of view. However, on the one hand, the more displaced a cylinder (BSA) is from the center (meaning its shadow size increases), the smaller the STR becomes. On the other hand, the contrary holds for the BHA method as the imaged apertures become smaller when increasing their tilt angle with respect to the traversing X-rays. A relationship between aperture size (BHA) and detected signal has been investigated in section 3.1.3. Similar results for both blocker and aperture sizes are found in the literature as well [MM98; ZMM99; GG02].

Furthermore, we note that a considerably large amount of scatter is detected in both methods although there is no scattering sample present. From the basic investigations concerning environmental and detector scatter presented in sections 3.1.2 and 3.1.3, we
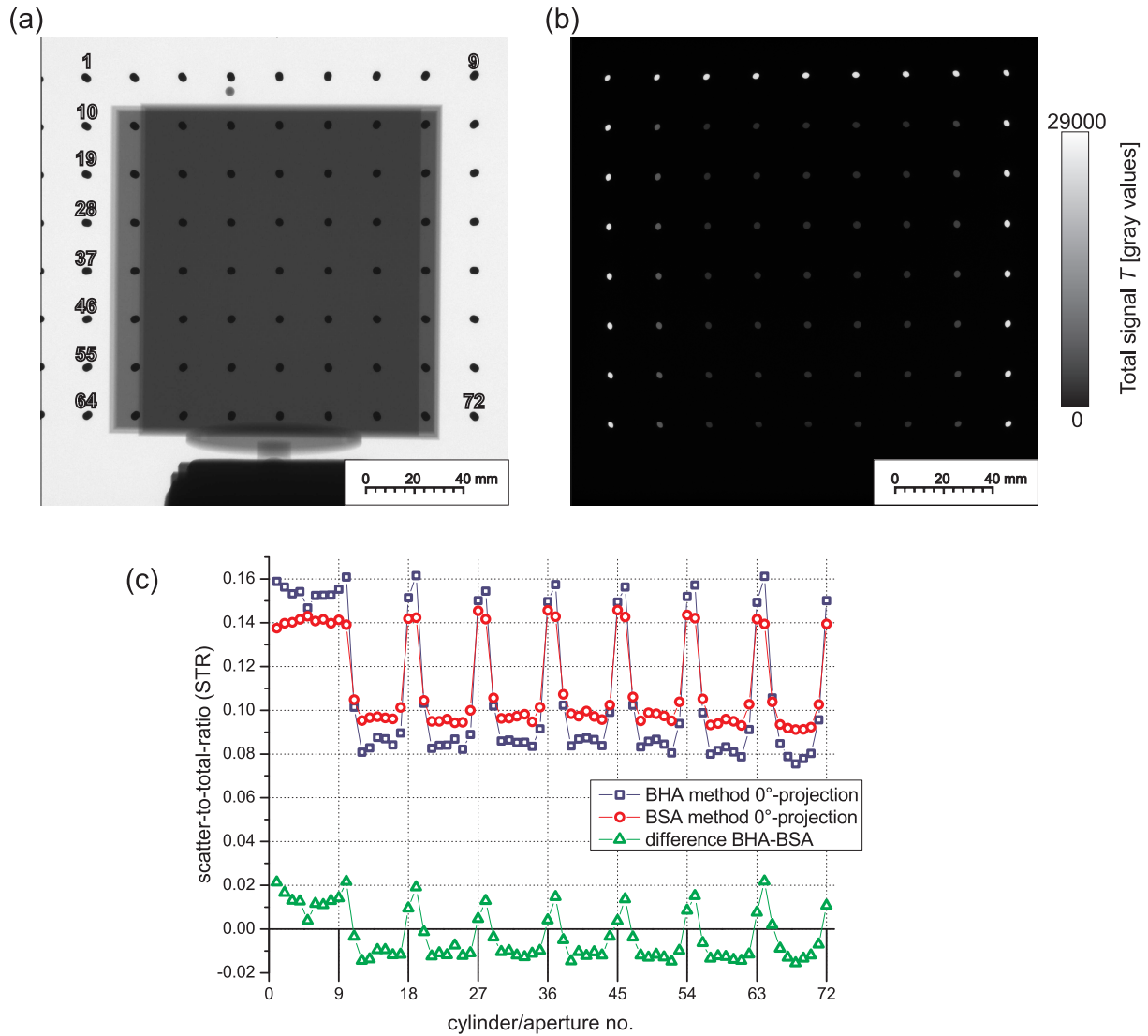
(a)

(b)

(c)

Figure 4.6: First projection (0°-projection angle) of a large-scale aluminum sample (with notches cut laterally) behind (a) BSA and (b) BHA, respectively. (c) Comparison of BSA and BHA method for the first projection. Measured scatter-to-total ratios (STRs) are reported for each cylinder and aperture of BSA/BHA as shown in panels (a) and (b). First, note the prominent difference in STRs between direct-beam sampling points and those which are shadowed by the sample. Second, a quantitatively different behavior between BSA and BHA methods is observed. See text for explanation.
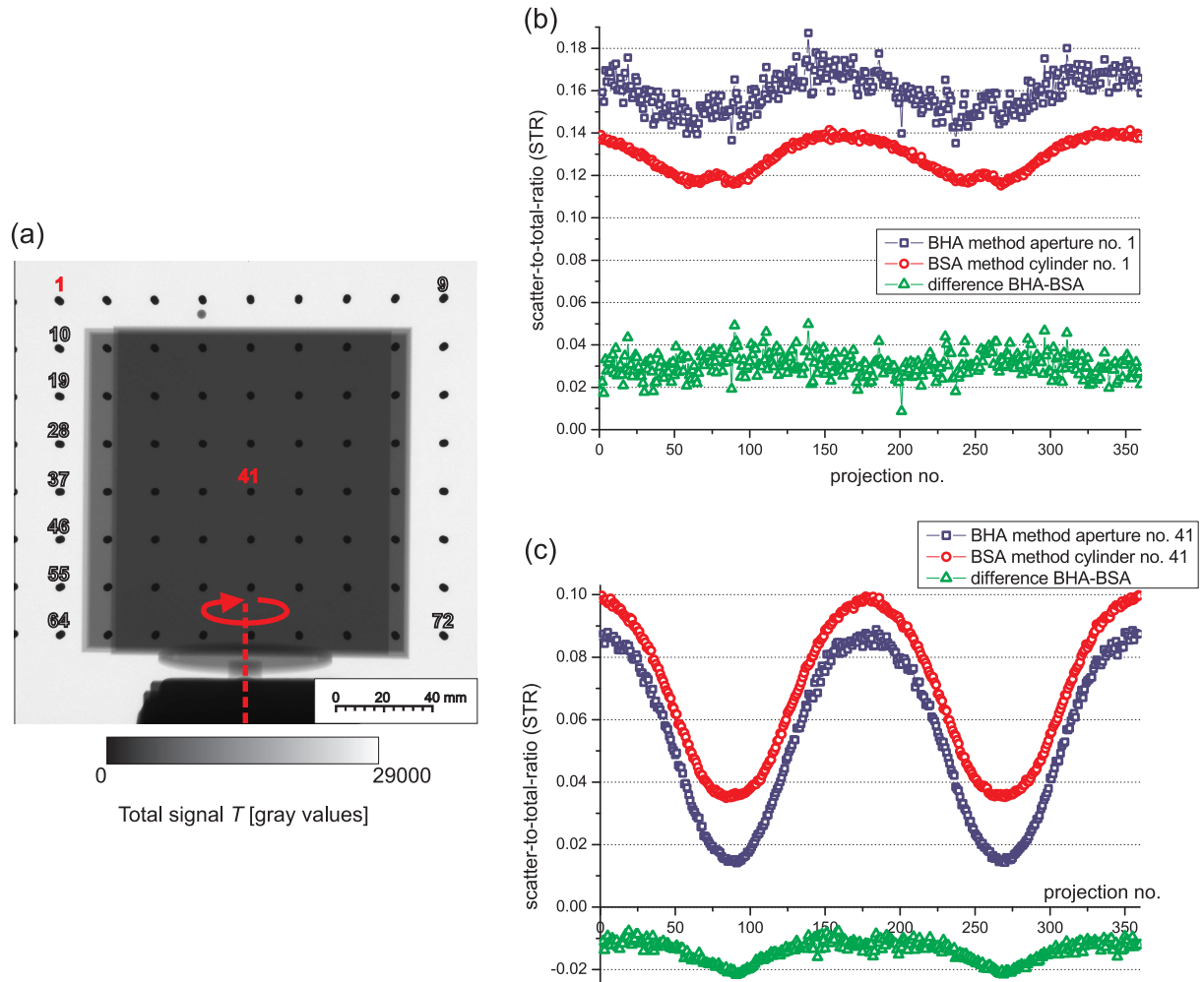
Figure 4.7: (a) First projection (0°-projection angle) of a large-scale aluminum sample (with notches) behind BSA, for reference. The sampling points under investigation are highlighted. The axis of rotation is indicated. (b) Measured STRs for top-left cylinder/aperture (no. 1) which is in the unobstructed, direct beam in all projections: The measured STRs are larger within the BHA measurement which is due to the geometric effect (smaller size of aperture). (c) Central cylinder/aperture (no. 41) which is shadowed by the sample in all projections: The measured STRs, in general, are higher within the BSA measurements which is due to a greater amount of scattered radiation by the PMMA plate (directly and indirectly scattered onto the detector). See text for further interpretation.

conclude that most of the detected scatter signal is due to secondary events in the detector, i.e. I_{Det} (X-ray scatter) and S_{Det} (electronic and light spread) in Eq. (3.3), and less due to environmental scatter I_{Env}. These findings are in good agreement with the results published by Peterzol *et al.* [PLB08].

In the BHA measurement, differences in the STR between apertures are greater than in the BSA measurement indicating that the STR is more accurately measured at small apertures and underestimated at bigger apertures whereas the BSA-based STRs are all underestimated by tendency. Smaller apertures/cylinders would improve the accuracy of scatter estimation. However, the geometric effect always leads to underestimation of scatter with the BSA in off-centered lead cylinders whereas with the BHA method the accuracy of scatter estimation increases for off-centered apertures.

In order to reduce this purely geometric effect, a focused BSA/BHA with lead cylinders/apertures aligned in parallel to the X-rays may be used. This is possible, but limited to certain imaging geometries (SOD, SDD), thus representing a non-universal BSA/BHA, which is also more difficult to manufacture.

Let us now discuss the results from the comparison measurement where a scattering sample is present. Figure 4.6(c) shows the measured STRs for the first projection (projection angle 0°). First of all, note that measured STRs are strikingly higher for sampling points in regions of unobstructed impinging radiation (direct-beam) than for those that are shadowed by the sample. Direct-beam STRs are of the order of 14% for BSA and 15–16% for BHA, while for sample-shadowed sampling points we only measure STRs of 8–10% of total intensity. Representing a key result from our experimental studies, this STR behavior is contrary to Monte-Carlo simulations which we conducted considering only object scatter. In such a simulated scenario, the maximum scatter level is found at the center of the object, cf. section 3.1.1.

We explain the observed effect as follows: Taking into account the strong magnitude of detector-internal scatter (I_{Det} and S_{Det}) that we quantified in section 3.1.3, as well as the narrow spreading of detector-internal scatter given by its point-spread function (PSF), the measured scatter signals contain a large portion of detector scatter from adjacent pixels. Thus, direct-beam regions with high total signals exhibit larger STRs since detector scatter stemming from the surrounding pixels is high. In contrast, object-covered sampling points exhibit lower STRs due to smaller total signals in the vicinity. We can deduce from Fig. 4.6(c) that several adjacent sampling points (such as, e.g. no. 10 and 11) may exhibit STRs quite different in magnitude. This will cause steep gradients in the interpolated scatter images in those regions, as we will see in section 4.3.

A second finding concerns the different STRs obtained for BSA and BHA methods. As illustrated in Fig. 4.6(c), the STRs measured with the BSA are greater than in the BHA measurement for all sampling points that are shadowed by the sample, and vice versa for direct-beam sampling points (i.e. sampling points 1–9, 10, 18–19, 27–28, 36–37, 45–46, 54–55, 63–64, 72). From the measurement without sample (Fig. 4.5), we would expect that all STRs measured by the BSA method are less than or equal to BHA-measured ones. We conclude that additional scatter I_{PMMA} from the PMMA plate used within the BSA method (cf. Eq. (4.3)) is the cause for the increased STRs in the BSA case.

This conclusion is also confirmed by the STR study of two exemplary sampling points highlighted in Fig. 4.7(a) over the complete course of a rotation of the sample. In

Fig. 4.7(b), the BHA-measured STR for the top-left sampling point no. 1, where the geometric effect that we described above is maximum, in general is higher by about 3%-points compared to its BSA counterpart. On the other hand, as depicted in Fig. 4.7(c) for the central sampling point no. 41, where geometric effects are negligible, the BSA method produces in general STRs that are $1 - 2\%$-points higher than in the BHA method. We can ascribe this behavior to additional scatter from the PMMA plate. Particularly, the difference in STRs between the two methods is largest in those projections where the object is rotated 90° and 270°, respectively, i.e. where scattered radiation from the PMMA plate is less hindered by the object to reach the detector. In a CT of this specific sample, these projection angles would be important in respect of being maximally scatter-free and noise-reduced since the primary signal is low at these length scales of penetrated material (here: minimally 185 mm of aluminum).

In another aspect, Fig. 4.7(c) clearly shows the changing scatter contribution stemming from the object. The STR curves resemble a sinusoidal function and reflect the angular-dependent size of the sample's front area facing the focus while the sample is rotated. It is highest for projection angles 0°, 180° and 360°, and lowest when the sample's narrow side is facing the focus in projections at angles 90° and 270°. The observed effect is due to the fact that a larger sample front area facing incident radiation produces more scatter events than a smaller area.

Finally, the scatter estimates by the BHA method show a higher noise level than those measured with the BSA, which can be clearly recognized in Fig. 4.7(b) for the STR of a permanent open-field region. Since, in the BHA method, high-level signals are subtracted, cf. Eq. (4.2), the corresponding noise level, given by

$$\Delta S_{\mathrm{BHA}}(n) \propto \sqrt{(\Delta T(n))^2 + (\Delta P(n))^2}, \tag{4.5}$$

is consequently higher than in the situation of a BSA measurement where the scatter estimate is measured directly and the signal itself is much lower. Here, the noise level is assumed to be dominated by quantum noise, i.e. Poisson-distributed, and thus proportional to the square root of the signal, $\Delta S_{\mathrm{BSA}}(n) \propto \sqrt{S_{\mathrm{BSA}}(n)}$ for the BSA case. In order to improve the signal-to-noise ratio (SNR) for BHA-measured scatter estimates, one has to average over more projections. This is more time-consuming, but poses no general constraint to this method.

4.3 Experimental Demonstration of Beam–Hole Array Scatter Correction

In section 4.2, we compared the proposed BHA method experimentally to the more established BSA with respect to scatter-to-total ratios (STRs). We found a few prominent differences, e.g. smaller STRs with the BHA method at critical projection angles due to absence of an additionally scattering PMMA plate. This may represent a (small) advantage of the BHA over the BSA method. Thus, in this section, we show a first demonstration of the proposed BHA scatter correction method applied to the CT of a highly scattering, industrial sample, i.e. a ceramic specimen used in power generation technology.
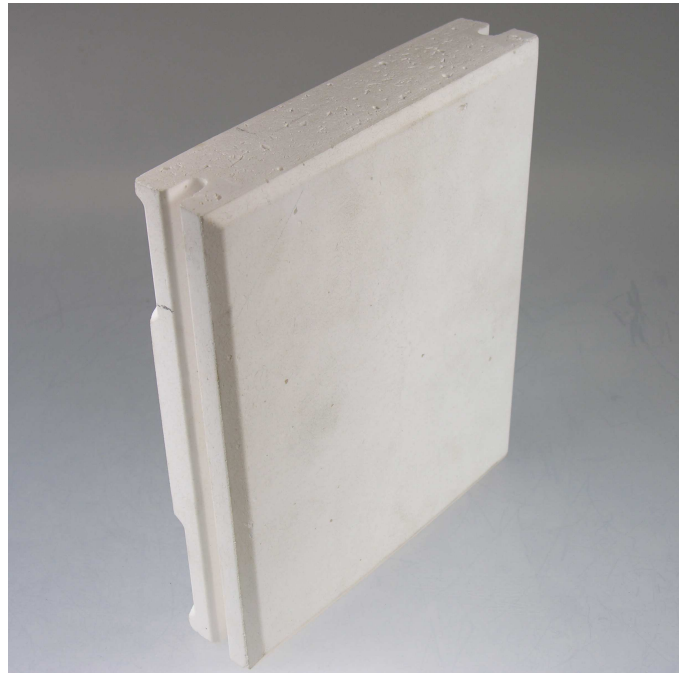
Figure 4.8: Photograph of the tomographed ceramic specimen that is used in power generation technology. Samples such as the one shown here are to be inspected for inner cracks, voids, and dimensional tolerances with CT. The specimen's dimensions are $192 \times 190 \times 38\,\text{mm}^3$.

4.3.1 Experimental Setup

A photograph of the tomographed sample is presented in Fig. 4.8. The dimensions of the specimen are $192 \times 190 \times 38\,\text{mm}^3$, it is manufactured from an aluminum-oxide based ceramic. Samples such as the one examined here are to be inspected for inner cracks, voids, and dimensional tolerances with CT. These inspection tasks require a high-quality CT in terms of spatial resolution and contrast, but also in terms of adequate suppression of any artifacts such as those caused by scatter.

We use the CBCT scanner as described in section 4.2.1.1. Here, SOD is set to 80 cm and SDD to 100 cm. In the first scan, the beam-hole array is put in front of the specimen at $x_{\text{BHA}} = 60\,\text{cm}$. The specimen itself is mounted on the rotating table as shown in the 0°-projection in Fig. 4.9, i.e. tilted by approximately 45°. By this tilting, the top and bottom region of the specimen expose less material to the imaging X-ray cone-beam and are thus better penetrated in those CT projections where long penetration lengths occur in central regions of the specimen, i.e. around projections angles of 90° and 270°. For these projections, the tilting results in relatively high primary signals in the mentioned regions of the specimen compared to a situation where it is not tilted and penetration lengths are critical, yielding only extremely small primary signals for the entire object.

The tilted imaging configuration in combination with our 225 kV X-ray tube allows for good inspection of at least the regions of interest indicated by red boxes in Fig. 4.9. A second CT with the specimen rotated by 90° would be necessary to also tomograph the remaining regions of interest, i.e. the other two notch-halves. Generally, irradiation can
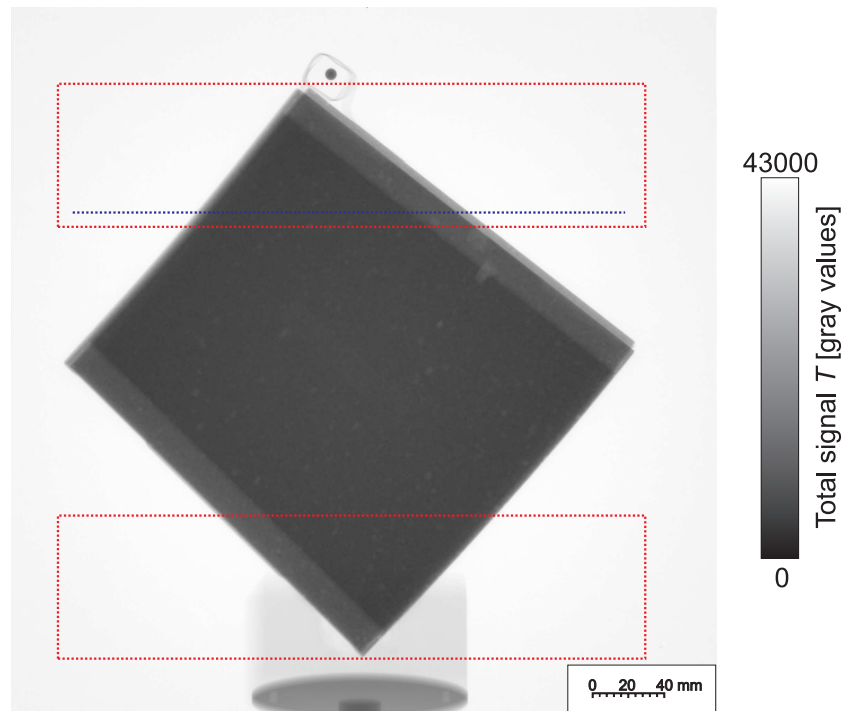
Figure 4.9: First projection (0° angle) from the CT of the ceramic specimen demonstrating the tilted mounting in order to obtain shorter penetration lengths in the top and bottom region of the specimen, indicated by red boxes. Here, primary signals are relatively high and these regions can be reconstructed with very little artifacts – after correction of scatter and beam hardening effects. In central regions however, penetration lengths become too long in projections around 90° and 270° to measure a reasonably high primary signal. Consequently, these regions show severe artifacts in the reconstructed CT volume. The blue dashed line indicates the position of the reconstructed CT slices presented in Fig. 4.11.
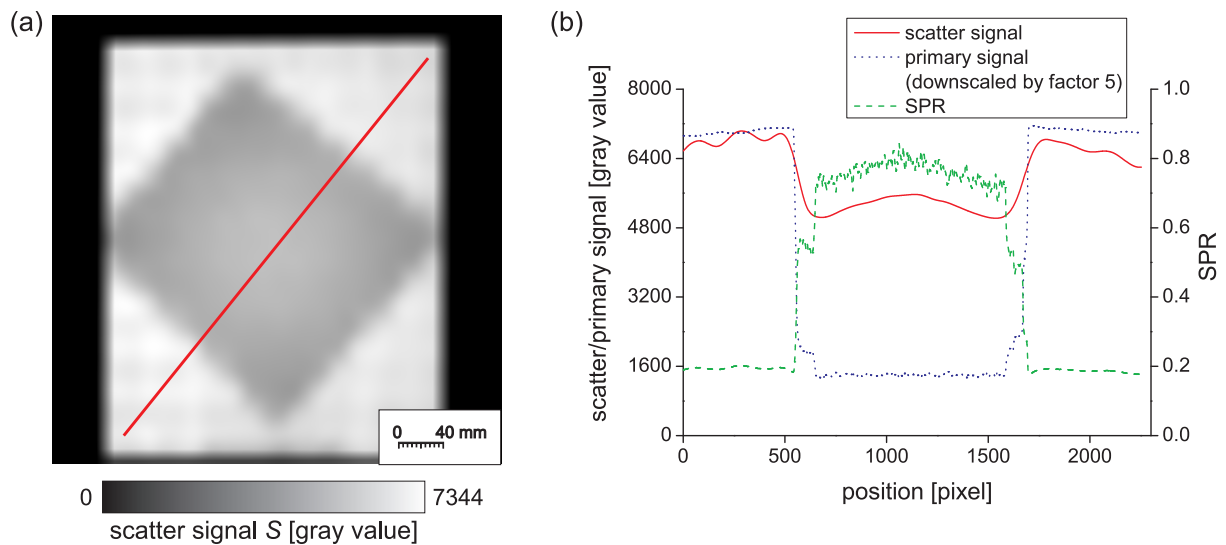
Figure 4.10: (a) Interpolated, smoothed scatter image for first projection (0°) and (b) the corresponding line profile (red graph). Scatter signals resemble primary signals (blue graph). The scatter-primary-ratio (SPR, green curve) amounts to 78% in the object center.

be improved and penetration lengths increased when employing X-ray tubes with higher voltage.

CT reconstructions are computed by an FDK algorithm (cf. section 2.2.3.2), which is implemented as a part of our own X-ray CT software. Here, a linearization-based correction of beam-hardening effects is employed as it was described in section 2.3.1.

4.3.2 Experimental Investigations and Results

In order to generate scatter images, a total of 3×2 equidistantly horizontally and vertically shifted BHA-sets, each comprising 360 projections, have been recorded. Shifting the BHA yields a finer sampling grid of primary signals. This is necessary in order to detect the high spatial frequency content in the scatter distribution which we expect from our initial comparison measurements discussed in section 4.2.3. The total signals at the given sampling points are extracted from the set of 1080 projections of the second CT scan (without BHA), whereby scatter estimates according to Eq. (4.2) can be calculated. For all measurements, the dose is recorded as described in section 4.2.1.1 to be able to compensate for dose fluctuations.

We use a bicubic spline interpolation algorithm in order to generate scatter images based on the BHA-measured scatter data. Scatter images are smoothed by a median filter afterwards. In Fig. 4.10, both the interpolated scatter image for a projection angle of 0° and the corresponding line profile – as indicated in the scatter image – are shown. As can be seen in Fig. 4.10(b), the scatter signal resembles the primary signal, including high spatial frequencies where object edges are present. The calculated scatter-to-primary ratio (SPR) along the given line profile is 75–80% in central regions covered by the object, whereas it can exceed 450% in critical projections around 90° and 270°.
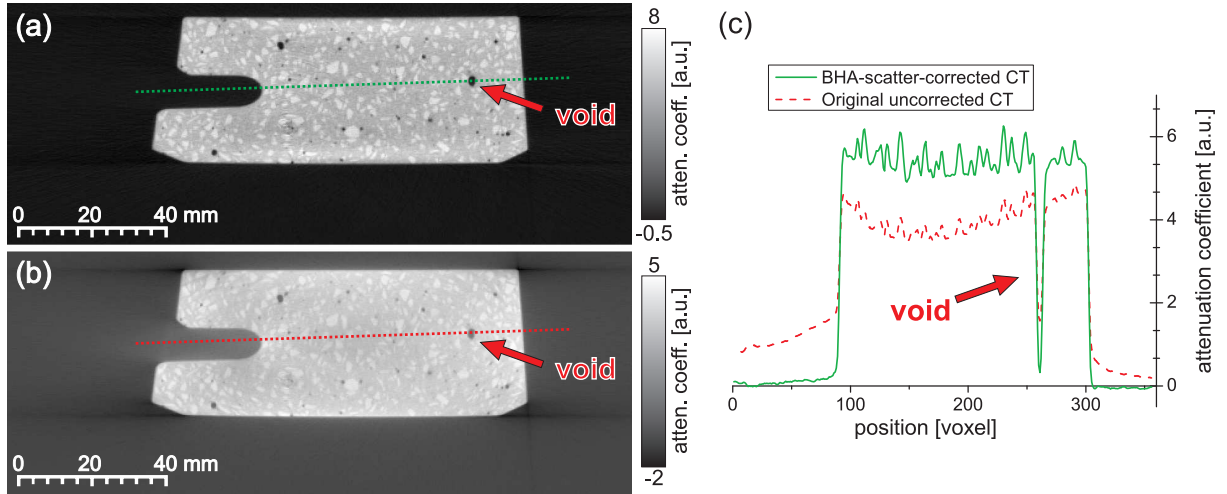
Figure 4.11: (a) Axial CT slice (cf. Fig. 4.9, blue dashed line) from the BHA scatter-corrected CT volume of the ceramic specimen, (b) shows the corresponding slice from the uncorrected CT volume. Corresponding line profiles are indicated and shown in (c).

We subtract the interpolated, smoothed scatter images from the original CT projections. Two different volume reconstructions are performed, one with the uncorrected projections and the other with the scatter-corrected projections. For comparison, an axial slice extracted from each of the volumes is presented in Fig. 4.11: in panel (a) for the beam-hole array scatter-corrected CT and in panel (b) for the uncorrected CT. The indicated line profiles are given in panel (c).

4.3.3 Interpretation

First, note that the BHA-calculated scatter image depicted in Fig. 4.10 remarkably differs from common expectations about scatter functions. Usually, relatively low-frequency scatter functions are assumed [BS88; NTC04; ZBF06]. In fact, a Monte-Carlo simulation with similar parameters as in our CT scan and a rectangular box-shaped object produces a scatter function as depicted in Fig. 3.1(b) with its maximum near the center and slowly decreasing flanks. However, here we notice high spatial frequencies present in the scatter images close to projected sample edges. The occurrence of high frequencies is caused by a strong contribution from detector-internal scatter events I_{Det} and S_{Det} (cf. Eq. (3.3)). Our findings from the comparison measurements as well as from the CT scan with BHA scatter correction are in good agreement with results published recently for the BSA method by Peterzol *et al.* [PLB08]. They also attributed high frequencies to detector-internal scattering.

Second, we performed a BHA scatter correction in an industrial CT scan of a strongly scattering ceramic specimen. The uncorrected volume shown in Fig. 4.11(b) exhibits strong artifacts such as cupping and streaks. Note the particularly dark streaks along the corners and a bright streak along the notch region. These vanish almost completely in the scatter-corrected volume, as can be seen in Fig. 4.11(a). Also, overall contrast is

enhanced as can be seen in the corresponding line profiles in Fig. 4.11(c). Here, e.g. in the mid-region, local contrast of the void (see red arrows) is increased by 24%-points from 70% to more than 94%. This will also improve the ability to detect smaller cracks within the reconstructed notch regions of the specimen. Furthermore, while reconstructed voxel gray values outside the object in the corrected CT are almost zero as they should be, they are not close to zero in the uncorrected CT, cf. the long tail of the line profile (red curve) inside the notch region in Fig. 4.11(c). For dimensional measurement tasks, this leads to deviations in the surface detection process. Finally, edge sharpness is improved significantly in the scatter-corrected volume, see Fig. 4.11(c).

4.4 Discussion

In this chapter, two experimental scatter correction methods, the beam-stop array (BSA) method and the beam-hole array (BHA) method, have been compared to each other. The BHA method can be considered an alternative and inverse technique to the more established BSA method. Although equivalent from a theoretical point of view, in practice, the BHA and BSA methods differ in certain aspects which have been addressed in section 4.2. First, the observed geometric behavior which is different for projected, off-centered apertures (BHA) and beam stops (BSA), leads to a more accurate scatter estimate within the beam-hole method. Second, no additional scattering material as in the beam-stop method has to be used, which has been shown to reduce overall scatter. This is important for large industrial samples where primary signals are often weak in certain projections and where it is thus preferable to reduce noise as well as scatter-to-primary ratios. For these reasons, the proposed BHA method offers specific advantages over the BSA method under certain conditions.

An example for such conditions, where the BHA method is particularly suited, is the series inspection of ceramic samples used in power generation technology. The NDT inspection task is to ensure that (i) no cracks exist above a threshold size, (ii) voids do not exceed a specified volume size, and (iii) that dimensions of the part are within specified tolerance ranges. This necessitates a high-quality CT free from artifacts. Since the ceramic samples represent large-scale parts which lead to large scatter contributions, and hence, to the formation of significant scatter artifacts in CT, a suitable scatter correction such as provided by the BHA method is necessary. In order to create accurate scatter images, a greater effort compared to the BSA method is needed, since scatter estimation with the BHA represents an indirect method and is thus more sensitive to dose fluctuations as well as quantum noise within the image. For this reason, dose recording and a higher level of averaging are necessary. However, the initially greater effort is worthwhile in series measurements since the BHA method reduces overall scatter and noise by not having to insert an additional acrylic plate in the series CT scans as it would be necessary when employing a BSA.

For this specific sample, we have successfully shown the performance of the BHA method. Additionally, the CT was corrected for beam-hardening. The reconstructed CT volume allows for inspection tasks in the regions of interest, i.e. the notches of the specimen marked by red boxes in Fig. 4.9. These regions are almost free of scatter artifacts in the CT. However, the method fails to correct artifacts in central regions of the sample,

i.e. in mid-slices in between the red boxes. This is due to low primary signals, and hence, to bad scatter-primary-ratios (SPR). In this situation, the total measured signal mainly consists of scatter contribution that must be estimated very accurately in order to avoid new errors to the corrected CT. In general, regions with high SPRs are very sensitive to scatter correction by signal subtraction since the scatter signal may be overestimated, and hence, the primary signal underestimated, resulting in pronounced (bright) streaks along corresponding projection angles.

In respect of microtomography being predestinated for scanning small and tiny samples, placing the BHA or BSA in front of the sample is practically impossible. However, we can use the BHA also for scatter correction with small samples by placing the BHA behind the sample. An equivalent positiong of beam-stoppers behind the sample for scatter measurement is not possible since it blocks scattered radiation in part. Hence, the BHA method offers another advantage over the BSA concerning small samples.

From a more general point of view, both the BSA and BHA method can be successfully applied for scatter correction in industrial CBCT. However, both require at least a second scan which implies additional scan time and dose. In the CT demonstration employing the BHA method presented in section 4.3, even six different BHA-sets were recorded in order to obtain a higher sampling rate. This is necessary due to the expected high spatial frequencies within the scatter images. As presented in this chapter, both BSA and BHA method are inefficient in terms of scan time and dose. Thus, there is a motivation to integrate these measurements into a single, normal CT scan without extending scan times.

Concluding this chapter, we want to remark that there exist a few, very recent publications which use moving beam-stopper techniques [ZSF05; WMS10; Yan+10]. They aim at measuring scatter data simultaneously to the normal CT scan. Here, missing primary information (in the shadows of the beam-stoppers) is a major challenge and the proposed schemes attempt to interpolate missing primary data [ZSF05; Yan+10], or to omit it locally in an adapted reconstruction process [WMS10]. A different approach for scatter correction which also requires only a single CT scan will be presented in chapter 5.

Chapter 5

Scatter Correction by Temporal Primary Modulation

In the last chapter, we have discussed and compared two experimental scatter correction methods employing beam-stop and beam-hole arrays. Both techniques represent robust and reliable methods that have proven their capability to improve CT image quality significantly. However, as these methods belong to the class of blocker-based measurements, a certain amount of primary X-rays get totally blocked, at least in a fraction of CT projections. This loss of primary data either means a loss of information or additional scan time and dose that are necessary to obtain the missing primary data. Usually, a second scan is performed in which the blockers are either displaced by a certain distance or completely removed.

In the light of these limitations of blocker-based methods, recently, two groups, Maltz *et al.* and Zhu *et al.*, have theoretically proposed and preliminarily tested a new method for scatter correction [Mal+05; ZBF06]: the scatter measurement by *spatial primary modulation* (SPM). With their proposed method, only a single CT scan is required which both contains the normal projection data as well as the sampling of scatter data. In SPM, the primary photon fluence is spatially amplitude modulated by a fine, repetitive pattern before irradiating the sample. The pattern can either be sinusoidal or rectangular. While the imprinted modulation pattern is preserved by primary photons, it is 'smeared out' by scattered photons, and hence, the scatter contribution at the detector plane will not exhibit this pattern. Hereby, a separation of primary and scatter fluence in the 2D spatial image frequency space is possible afterwards.

Inspired by this work, we devise a scatter correction method in which the primary fluence is amplitude modulated in the time domain. We call this *temporal primary modulation* (TPM): In a simple *gedankenexperiment*, as illustrated in Fig. 5.1, we assume that we are able to temporally modulate the amplitude of the primary fluence for each detector pixel individually. In such a situation, each detector pixel n, continuously recording incident radiation, would yield a total signal containing a single primary fluence contribution $P(n)$ of the frequency f_0 unique for this particular pixel. Additionally, there are many other contributions $S_1, S_2, \dots$ from scattered radiation with different modulation frequencies f_1, f_2, etc. Building on lock-in techniques, we would be able to separate the signal at unique frequency f_0 for this particular pixel from the rest of signal contributions. Hence, in our situation, this would enable a separation of the primary from the scatter signal contribution. Moreover, we could even infer the origins and their specific contributions
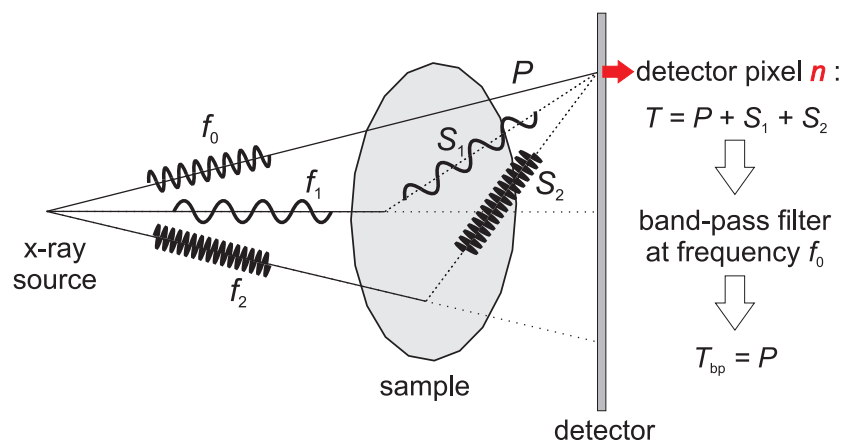
Figure 5.1: *Gedankenexperiment* illustrating the key idea of scatter correction by temporal primary modulation (TPM). For each detector pixel, the primary fluence P gets amplitude-modulated at a unique modulation frequency, e.g. for the particular pixel n, at frequency f_0. Besides the primary signal P, the total signal T measured at this pixel also contains scatter contributions $S_1, S_2, \ldots$ from all over the sample, but they exhibit different modulation frequencies. Thus, a separation of primary and scatter signals is possible by adequate band-pass filtering (lock-in technique).

of scatter for each pixel separately by analyzing the other frequency contributions f_1, f_2, etc.

Due to technical limitations in experimental practice, we cannot perform a pixel-wise modulation as in the gedankenexperiment. Thus, a simplified, yet practical form of TPM with just a single modulation frequency for primary fluences and assumingly constant scatter contributions is realized experimentally. While maintaining the advantage of SPM requiring only a single scan, the TPM method proposed in this chapter avoids some of the inherent limitations and problems that occur with SPM as we will see below.

In this chapter, we will describe the theoretical background of scatter correction by TPM in section 5.1. Here, different forms of experimental realization employing so-called primary modulators will be discussed, too. In the following section 5.2, a series of Monte-Carlo simulations as well as a theoretical analysis will show that the key assumption in TPM, i.e. temporally constant scatter contributions, is dependent on the dissimilarity between frequencies in the spatial modulation pattern and the spatial image frequencies of the sample. In section 5.3, we present a beam-hardening correction based on the linearization approach that we employ within the TPM method for compensation of beam-hardening effects caused by the primary modulator. Section 5.4 will describe the experimental implementation of TPM. We present two key results from the experimental investigations concerning TPM: First, in section 5.5, a comparison between TPM- and BSA-obtained scatter data is performed. Second, in section 5.6, we demonstrate the successful application of the proposed TPM method for scatter correction within a single CT scan. Finally, section 5.7 summarizes our work and critically compares the TPM method to the SPM scatter correction.
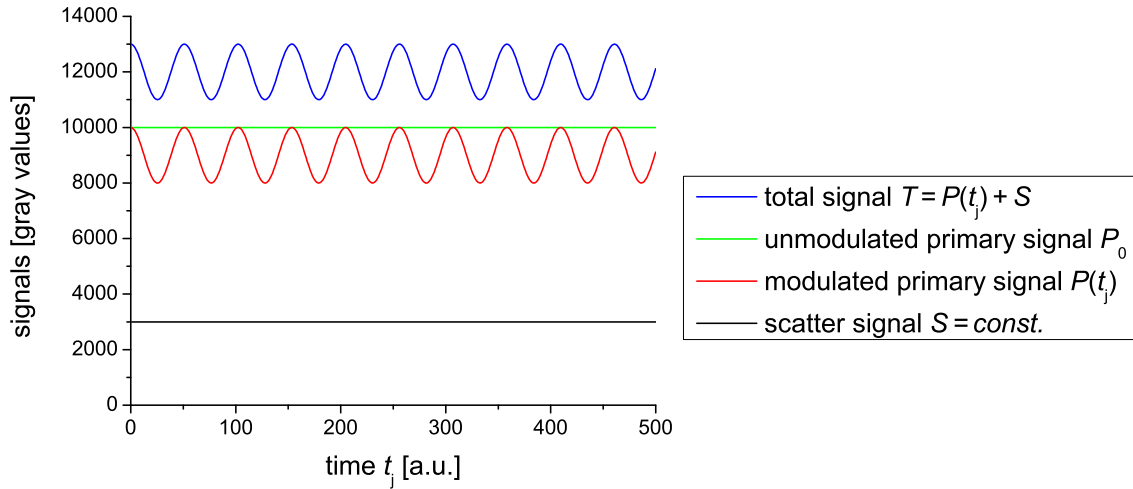
Figure 5.2: Basic principle of temporal primary modulation (TPM): Each angular CT projection is subdivided into a number N_{mod} of modulated projections j, e.g. $N_{\mathrm{mod}} = 500$. In this process, for an arbitrary pixel (x', y'), the primary signal P_0 (green) is temporally modulated yielding $P(t_j)$ (red). Since – in practice – the modulation of the primary signal P_0 can only be performed by appropriate attenuation, $P(t_j) \leq P_0$ applies. The scatter signal S (black) is assumed to be constant. Both signals, $P(t_j)$ and S together, give rise to the total signal $T(t_j)$ (blue).

5.1 Scatter Estimation by Temporal Primary Modulation

5.1.1 Basic Concept

In order to describe the concept of temporal primary modulation (TPM), let us consider a standard CBCT setup comprising an X-ray tube and a detector with pixels (x, y), $x = 1 \ldots x_{\mathrm{max}}$, $y = 1 \ldots y_{\mathrm{max}}$. We assume that it is possible to amplitude modulate the primary fluence incident on the object by some means. Thereby, we postpone the question how this could be realized technically. Ideally, we would be able to manipulate the primary X-ray fluence for each pixel (x, y) individually as presented above in the gedankenexperiment. However, here, we want to limit our considerations to the case where only one modulation frequency ω_{mod} exists for modulating the primary fluence while the total scatter contribution at each detector pixel is assumingly constant at the same time and under certain conditions. The latter represents a key assumption for the TPM method and we will discuss it in detail in section 5.2. This scenario of modulated primary and constant, i.e. unmodulated, scatter signal is depicted in Fig. 5.2. Subsequent separation of the modulated primary and the constant scatter signal is possible by AM demodulation as described in the following.

In a formal framework, we divide each angular CT projection into $j = 1 \ldots N_{\mathrm{mod}}$ sub-projections, also denoted as modulated projections, in which for each pixel the primary fluence is amplitude modulated in the time domain while the object under investigation

remains stationary. Furthermore, let us consider an arbitrary pixel (x', y') and, for simplification, omit its mentioning in the following equations. The primary signal P_0 of this pixel is temporally modulated by multiplication with a modulation function $f_{\text{mod}}(t_j)$,

$$P(t_j) = P_0 \cdot f_{\text{mod}}(t_j) \ , \tag{5.1}$$

where the modulation function can be formally defined as

$$f_{\text{mod}}(t_j) = 1 + \frac{A}{2} \left(\cos(\omega_{\text{mod}} \cdot t_j) - 1 \right) \ , \tag{5.2}$$

with A being the modulation strength and ω_{mod} the modulation frequency. We choose this definition of f_{mod}, since – in experimental practice – the modulation of the primary signal P_0 can only be performed by appropriate attenuation ($P(t_j) \leq P_0$). The primary fluence from Eq. (5.1) is superimposed by a scatter signal $S(t_j)$. As described by Eq. (3.2) in section 3.1 and illustrated in Fig. 5.2, both of them together yield the measured total signal

$$T(t_j) = P(t_j) + S(t_j) \tag{5.3}$$

for pixel (x', y'). As mentioned above, the key assumption in TPM is that the scatter fluence $S(t_j)$ remains virtually unaffected by temporal primary modulation, i.e. $S(t_j) \simeq$ const. With the modulation only being present in the primary signal, we are able to extract this part exclusively from the measured total signal by AM coherent demodulation [Shm06]. We obtain the primary signal by multiplication with the carrier signal $\frac{A}{2} \cos(\omega_{\text{mod}} \cdot t_j)$ (time-dependent term in Eq. (5.2)) and subsequent lowpass-filtering (here: averaging),

$$P_{0,\text{est}} = \frac{4}{A \cdot N_{\text{mod}}} \sum_{j=1}^{N_{\text{mod}}} T(t_j) \cdot \cos(\omega_{\text{mod}} \cdot t_j) \ . \tag{5.4}$$

For a detailed derivation of the demodulation process, refer to appendix A. Substitution of the estimated primary signal from Eq. (5.4) into Eq. (5.1) yields $P_{\text{est}}(t_j)$. Subsequently, the estimated scatter fluence for pixel (x', y') can be calculated as

$$S_{\text{est}} = \frac{1}{N_{\text{mod}}} \sum_{j=1}^{N_{\text{mod}}} \left[T(t_j) - P_{\text{est}}(t_j) \right] \ . \tag{5.5}$$

Extending this calculation over all pixels (x, y) yields an estimated scatter image. For each modulated CT projection j, the scatter fluence is corrected by subtraction of the scatter estimate. Primary modulation patterns still existent in the projection can be eliminated by division with the corresponding flat-field projection where no object is present and primary modulation is the same as in the modulation projection j. In order to improve the signal-to-noise ratio (SNR), we calculate the mean from these N_{mod} projections to obtain a scatter- and modulation-corrected angular CT projection.

5.1.2 Experimental Realization using Primary Modulators

Both in spatial (SPM) and temporal primary modulation (TPM), the primary fluence has to be amplitude modulated by some means. For this purpose in SPM, Maltz *et al.*
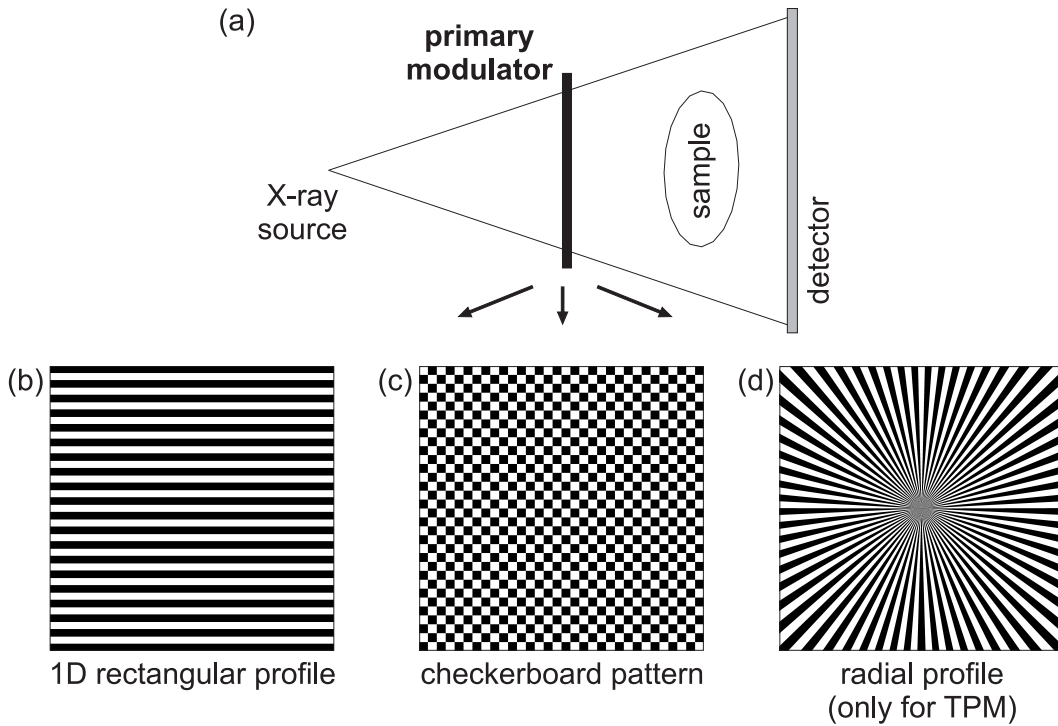
Figure 5.3: (a) Both in SPM and TPM, a primary modulator is placed in between X-ray source and sample to amplitude modulate the primary photon fluence. Different spatial arrangements are possible for the primary modulator such as (b) a 1D rectangular profile or (c) a checkerboard pattern. These two have been tested in SPM and can be used also for TPM. Additionally, (d) radial profiles (rotating chopper wheel) are conceivable for TPM.

have suggested a 1D attenuation grating with spikes [Mal+05], and Zhu *et al.* have implemented a 1D rectangular [Zhu+09] as well as a checkerboard-like attenuation profile [ZBF06]. These so-called **primary modulators** are spatially varying, repetitive attenuation patterns inserted between X-ray source and sample as illustrated in Fig. 5.3.

On the one hand, if installed stationary, primary modulators can be used for SPM as they imprint a distinct spatial attenuation pattern on the primary fluence while the scatter fluence does not exhibit this imprint. Thereby, from a single projection, a separation of primary and scattered signals is possible by adequate filtering algorithms, cf. [Mal+05; ZBF06].

On the other hand, by installing primary modulators **movable**, distinct attenuation functions that exhibit a temporal modulation for each pixel can be realized by translational – or rotational – steps of the primary modulator. Depending on the application, the moving of primary modulators may be implemented in a discrete (stepping) or in a continuous fashion (sliding). Either way, a sequence of $j = 1 \dots N_{\mathrm{mod}}$ modulated projections is recorded representing a set of temporally modulated total signals for all pixels. Subsequently, these data can be used for scatter estimation as described in section 5.1.1. The bottom part of Fig. 5.3 summarizes different forms of before-mentioned modulation patterns: Besides the 1D profile rectangular profile (Fig. 5.3(b)) and the checkerboard pattern (Fig. 5.3(c)), a rotating chopper wheel is also conceivable for TPM, see Fig. 5.3(d).
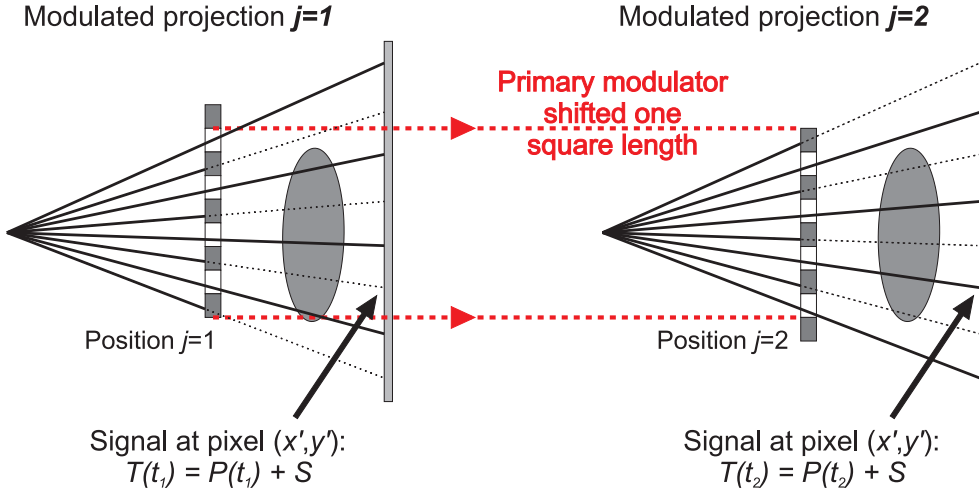
Figure 5.4: Schematic illustration of two-point temporal primary modulation by stepping the primary modulator back and forth for each CT projection. While primary signals are temporally amplitude modulated from projection $j{=}1$ to $j{=}2$, scatter fluence S is assumed to remain constant.

We would like to concretize one specific implementation of TPM realization relevant for considerations in the following sections. This involves the primary modulator with a checkerboard pattern, cf. Fig. 5.3(c). Aiming at a **two-point modulation** with $N_{\mathrm{mod}} = 2$, we suggest a discrete stepping of the primary modulator by half of a period, i.e. by one square length, as illustrated in Fig. 5.4. Moving the checkerboard pattern can be done either in vertical or horizontal direction.

From the two modulated projections $j{=}1, 2$ taken at the end positions of the stepping process of the primary modulator, the primary signal is given by

$$P_{0,\mathrm{est}} = \frac{|T(t_1) - T(t_2)|}{A} \; . \tag{5.6}$$

In the following, we assume that we do not need the absolute value function in Eq. (5.6) as the correct sign is given by the modulation strength A. We assume $T(t_1) > T(t_2)$ and $A > 0$ from now on and simplify Eq. (5.6) to:

$$P_{0,\mathrm{est}} = \frac{T(t_1) - T(t_2)}{A} \; . \tag{5.7}$$

This corresponds to Eq. (5.4) for $N_{\mathrm{mod}} = 2$ where the pre-factor of 4 is replaced by 2, which is due to the fact that we consider a two-point modulation rather than a full cosine-like modulation (which exhibits zero-crossings half the time in case of four and more sampling points). As a result, Eq. (5.5) simplifies to

$$
\begin{aligned}
S_{\mathrm{est}} &= \frac{T(t_1) + T(t_2)}{2} - \left(1 - \frac{A}{2}\right)\frac{T(t_1) - T(t_2)}{A} \tag{5.8} \\
&= T(t_1) - \frac{T(t_1) - T(t_2)}{A} \; . \tag{5.9}
\end{aligned}
$$

5.1.3 Noise Analysis

In experimental practice, the measured TPM signals will exhibit noise. In order to obtain the error in TPM scatter correction, in the following, we apply a propagation of uncertainty calculation. In a first step, we calculate the propagation of noise in the estimated scatter signal from Eq. (5.9):

$$\Delta S_{\text{est}} = \sqrt{(\Delta T(t_1))^2 \left(1 - \frac{1}{A}\right)^2 + (\Delta T(t_2))^2 \left(\frac{1}{A}\right)^2} \,. \tag{5.10}$$

As the X-ray photon statistics follow a Poisson distribution, it can be derived (see e.g. [Buz08]) that

$$\mu = \sigma^2 \,. \tag{5.11}$$

This means that the expectation value equals the variance of the random variable, or equivalently, i.e., the standard deviation is given by the square root of the expectation value, $\sigma = \sqrt{\mu}$. Thus, with $\Delta T(t_{1,2}) = \sqrt{T(t_{1,2})}$, we can rewrite Eq. (5.10) as:

$$\Delta S_{\text{est}} = \sqrt{T(t_1) \left(1 - \frac{1}{A}\right)^2 + \frac{T(t_2)}{A^2}} \,. \tag{5.12}$$

From Eq. (5.12), we deduce that a small modulation strength A will lead to considerable amplification of the noise in the scatter estimate S_{est}. Thus, in experimental practice, we perform averaging over pixel clusters, comprising N_{pix} pixels:

$$S_{\text{est}}^{\text{avg}} = \frac{1}{N_{\text{pix}}} \sum_{k=1}^{N_{\text{pix}}} S_{\text{est}}(k) \,. \tag{5.13}$$

If we assume that S_{est} does not vary in the (small) region of averaging, then Eq. (5.12) will result in:

$$\Delta S_{\text{est}}^{\text{avg}} = \frac{1}{\sqrt{N_{\text{pix}}}} \Delta S_{\text{est}} \tag{5.14}$$

$$= \frac{1}{\sqrt{N_{\text{pix}}}} \sqrt{T(t_1) \left(1 - \frac{1}{A}\right)^2 + \frac{T(t_2)}{A^2}} \,. \tag{5.15}$$

The total signals $T(t_{1,2})$ can be expressed as sum of primary and of scatter signals:

$$T(t_1) = P_0 + S = P_0 \cdot (1 + \text{SPR}) \tag{5.16}$$

$$T(t_2) = P_0 \cdot (1 - A) + S = P_0 \cdot (1 - A + \text{SPR}) \,, \tag{5.17}$$

where in the last steps we have introduced the scatter-to-primary ratio (SPR) defined by $\text{SPR} = S/P_0$. Thus, uncertainty in the total signals $T(t_{1,2})$ is given by X-ray photon statistics as

$$\Delta T(t_1) = \Delta P_0 \cdot \sqrt{1 + \text{SPR}} \tag{5.18}$$

$$\Delta T(t_2) = \Delta P_0 \cdot \sqrt{1 - A + \text{SPR}} \,. \tag{5.19}$$

By using Eqs. (5.16) and (5.17), we can rewrite Eq. (5.15) as

$$\Delta S_{\text{est}}^{\text{avg}} = \frac{\Delta P_0}{\sqrt{N_{\text{pix}}}} \sqrt{(1 + \text{SPR}) \left(1 - \frac{1}{A}\right)^2 + \frac{1 - A + \text{SPR}}{A^2}} \; . \tag{5.20}$$

In a second step, for TPM scatter correction, the estimated and averaged scatter image $S_{\text{est}}^{\text{avg}}$ is subtracted from the modulated projections $T(t_i)$ (cf. section 5.1.1) to yield primary signals

$$P_{\text{est}}^{\text{TPM}} = \frac{1}{N_{\text{mod}}} \sum_{i=1}^{N_{\text{mod}}} \frac{T(t_i) - S_{\text{est}}^{\text{avg}}}{f_{\text{mod}}(t_i)} , \tag{5.21}$$

where the scatter-corrected, modulated projections are divided by $f_{\text{mod}}(t_i)$ in order to reverse the modulation (flat-field correction). For the practical case of $N_{\text{mod}} = 2$ where bright $(f_{\text{mod}}(t_1) = 1)$ and dark squares $(f_{\text{mod}}(t_2) = 1 - A)$ are used for modulation, Eq. (5.21) yields:

$$P_{\text{est}}^{\text{TPM}} = \frac{1}{2} \left[T(t_1) - S_{\text{est}}^{\text{avg}} + \frac{T(t_2) - S_{\text{est}}^{\text{avg}}}{1 - A} \right] . \tag{5.22}$$

From Eq. (5.22), we can now derive the uncertainty of the TPM scatter-corrected signal $P_{\text{est}}^{\text{TPM}}$ by propagation of error as

$$\Delta P_{\text{est}}^{\text{TPM}} = \frac{1}{2} \sqrt{(\Delta T(t_1))^2 + (\Delta S_{\text{est}}^{\text{avg}})^2 \cdot \left(1 + \frac{1}{1 - A}\right)^2 + (\Delta T(t_2))^2 \cdot \left(\frac{1}{1 - A}\right)^2} . \tag{5.23}$$

By inserting Eqs. (5.18), (5.19) and (5.20) into Eq. (5.23), we obtain the relative error $\Delta P_{\text{est}}^{\text{TPM}}/\Delta P_0$ as

$$\frac{\Delta P_{\text{est}}^{\text{TPM}}}{\Delta P_0} = \dots$$

$$\frac{1}{2} \sqrt{1 + \text{SPR} + \left[\frac{1 + \text{SPR}}{N_{\text{pix}}} \left(\frac{A - 1}{A}\right)^2 + \frac{1 - A + \text{SPR}}{N_{\text{pix}} \cdot A^2}\right] \left(\frac{2 - A}{1 - A}\right)^2 + \frac{1 - A + \text{SPR}}{(1 - A)^2}} . \tag{5.24}$$

Equation (5.24) yields the relative noise in the TPM scatter-corrected primary signal $P_{\text{est}}^{\text{TPM}}$ in dependence of the modulation strength A, the scatter-to-primary ratio SPR, and the number of pixels N_{pix} of the average region. Figure 5.5 illustrates these dependencies by two graphs where in panel (a) the number of averaged pixels is $N_{\text{pix}} = 400$, while in panel (b) it is $N_{\text{pix}} = 36$. Each graph displays curves for scatter-to-primary ratios from $\text{SPR} = 0.0$ up to $\text{SPR} = 2.0$ in steps of 0.1. For illustration, the parameter in Fig. 5.5(a), i.e. $N_{\text{pix}} = 400 = 20 \times 20$ pixels, is chosen according to the conditions given in the experimental investigations presented in sections 5.5 and 5.6.

In the graphs depicted in Fig. 5.5, we find local minima in $\Delta P_{\text{est}}^{\text{TPM}}/\Delta P_0$ which are marked by blue crosses. Thus, for a given size N_{pix} of the average region, an optimum range of the modulation strength A exists and is highlighted in Fig. 5.5 by green zones. In the situation depicted in Fig. 5.5(a) for example, an optimum range is found for modulation
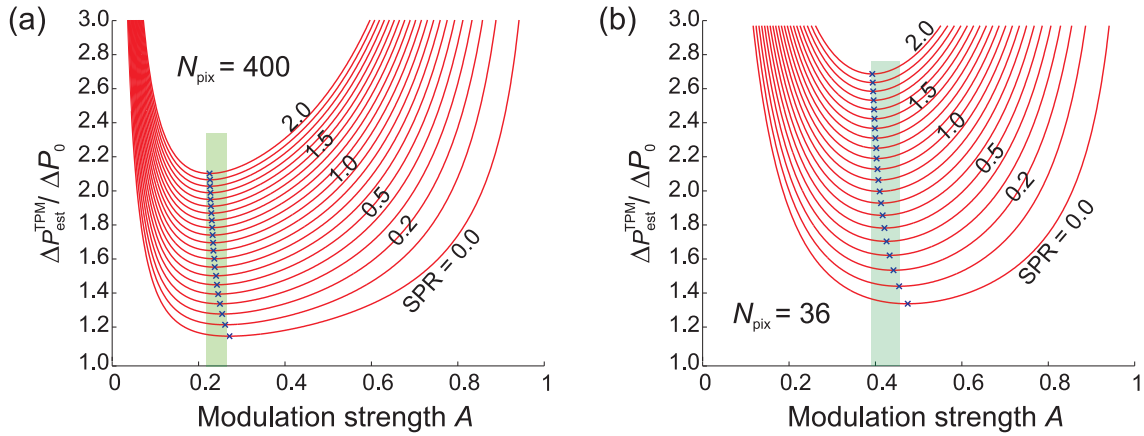
Figure 5.5: (a) Relative error $\Delta P_{\mathrm{est}}^{\mathrm{TPM}}/\Delta P_0$ of TPM scatter-corrected primary estimate $P_{\mathrm{est}}^{\mathrm{TPM}}$, plotted in dependence of modulation strength A while the number of averaged pixels is constant, $N_{\mathrm{pix}} = 400$. The red curves show different scatter-to-primary ratios (SPR) of which some are labeled. Blue crosses indicate local minima. The green zone defines the optimum range of modulation strength A. (b) Corresponding graphs as in (a) for $N_{\mathrm{pix}} = 36$.

strengths $A = 0.22 - 0.26$ and for expected scatter-to-primary ratios of SPR $= 0.1 - 2.0$. The optimum range shifts to higher modulation strengths A if the size of the average region, N_{pix}, is decreased, as can be deduced from Fig. 5.5(b). But, even with a stronger modulation A, the relative error $\Delta P_{\mathrm{est}}^{\mathrm{TPM}}/\Delta P_0$ increases for smaller average regions.

The relative errors $\Delta P_{\mathrm{est}}^{\mathrm{TPM}}/\Delta P_0$ depicted in Fig. 5.5 exhibit a steep rise towards high modulation strengths A. This is due to the flat-field correction $1/(1-A)$, i.e. the third term in Eq. (5.22). In fact, by omitting the summation over the second modulated projection, noise could be reduced to

$$\Delta P_{\mathrm{est}}^{\mathrm{TPM}} = \sqrt{(\Delta T(t_1))^2 + (\Delta S_{\mathrm{est}}^{\mathrm{avg}})^2} \tag{5.25}$$

in those cases where the modulation A is very strong.

In general, Eq. (5.24) gives a correlation between the modulation strength A and the size of the average regions, N_{pix}. Hereby, an optimum between the two experimental parameters A and N_{pix} can be derived for any given setting.

5.2 Verifying the Assumption of Constant Scatter

A key assumption with temporal primary modulation, as introduced in section 5.1, is that the total scatter contribution at each detector pixel is not affected by the modulation process. In other words, it has to be temporally constant during modulation of the primary fluence:

$$S(t_1) \stackrel{!}{=} S(t_2) = \mathrm{const.} \tag{5.26}$$

$$\Rightarrow \Delta S := S(t_1) - S(t_2) \stackrel{!}{=} 0 \,. \tag{5.27}$$

In the following, ΔS is denoted as difference in scatter fluences also. We expect errors in the TPM scatter estimation if the requirement expressed in Eq. (5.27) is not met, i.e. if $\Delta S \neq 0$.

In this section, we are going to verify the key assumption $\Delta S = 0$ by a Monte-Carlo simulation first, and second, append a theoretical analysis that investigates at which point the scatter fluences start to change. In both studies, we will see that this addresses the issue of how (dis)similar the image frequencies of the projected sample are compared to the spatial frequencies found in the primary modulation pattern.

5.2.1 Monte-Carlo Simulation

We perform two runs of Monte-Carlo simulations: In a first run, we simulate primary modulators with checkerboard-like pattern and different numbers of squares which corresponds to a variation of the spatial modulation frequency. In the second run, the modulation strength A is varied. We choose the simulation settings close to the experimental setup described in section 5.4. In particular, we focus on simulating checkerboard-like patterns which are shifted by one square length, i.e. by half a period, in order to realize a temporal primary modulation as described in section 5.1.2. For all simulations described here, a Monte-Carlo simulation package developed by Siemens is used [Sti93].

5.2.1.1 Variation of Spatial Modulation Frequency

Let us consider a simulation setup found in a typical industrial CT setting with an ideal, point-like X-ray source emitting a $225\,\mathrm{kVp}$ polychromatic spectrum as cone-beam radiation, prefiltered by $3\,\mathrm{mm}$ of copper. An ideal flat-panel detector with $512{\times}512$ pixels and dimensions of $40 \times 40\,\mathrm{cm}^2$ is set at a source-detector-distance (SDD) of $100\,\mathrm{cm}$. The sample is a pure aluminum block of $20 \times 20 \times 4\,\mathrm{cm}^3$ placed at a source-object-distance (SOD) of $80\,\mathrm{cm}$. Different primary modulators, each with side lengths of $94 \times 94\,\mathrm{mm}^2$, are simulated as 2D checkerboard patterns with different numbers of square fields, i.e. with $2^n \times 2^n$ squares, $n = 0 \ldots 5$. Simulation of greater n with tolerable noise leads to excessively long simulation times. Each dark square arises from beam attenuation by $0.7\,\mathrm{mm}$ copper which transmits 82% of primary radiation, i.e. modulation strength is homogeneously at $A = 0.18$. The primary modulator is placed $23.5\,\mathrm{cm}$ away from the X-ray source. Using the definition from above, we set $N_{\mathrm{mod}} = 2$. A first projection $j{=}1$ is simulated in this setting and a second $j{=}2$ in the inverse setting where the modulator is translated horizontally by one square length, i.e. primary modulation is maximally phase-shifted by 180° for all pixels.

As reference for the situation without modulator ($n = 0$), Fig. 5.6 depicts both the simulated primary and scatter fluences in the projection of the sample, as well as corresponding line profiles. For simulated primary modulator configurations from 2×2 up to 32×32 squares ($n = 1 \ldots 5$), Fig. 5.7 shows the primary projection $\mathrm{P}(t_1)$ in the top row. The difference of scatter fluences between the two modulator positions, ΔS, downsampled to 32×32 pixels, is shown in the middle row and corresponding line profiles across indicated sampling points in the bottom row. The number of simulated photons was $8 \cdot 10^8$ in the projections for configurations with 1×1 to 16×16 squares ($n = 0 \ldots 4$), and $6.4 \cdot 10^{10}$ in the case of 32×32 ($n = 5$) squares.
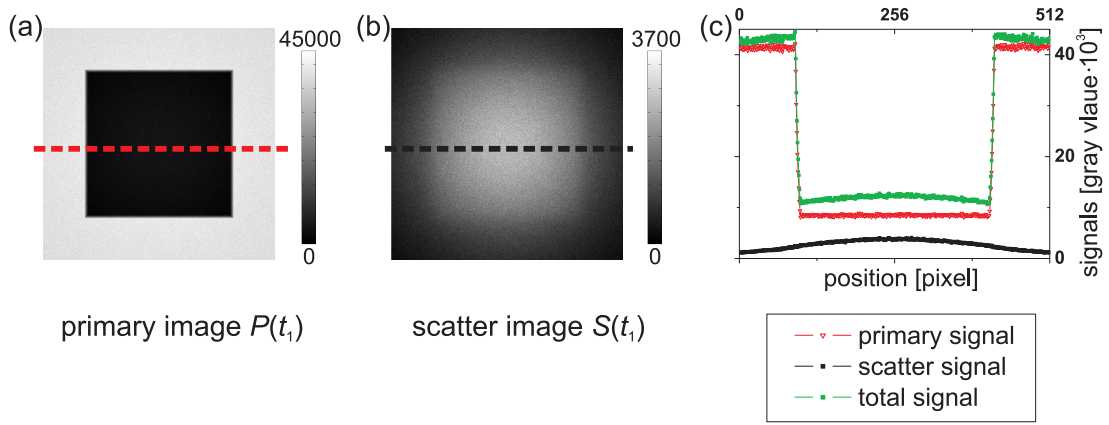
Figure 5.6: Monte-Carlo simulation of a radiographic projection of an aluminum sample without primary modulator for comparison. (a) The simulated primary image, (b) the corresponding scatter image, and (c) corresponding line profiles.

For configurations with 2×2 to 16×16 squares, note that the depicted differences $\Delta S = S(t_1) - S(t_2)$ partly resemble the spatial modulation pattern. Here, bright regions mark areas where $S(t_1) > S(t_2)$, i.e. in primary modulator configuration at time t_1 more scattered radiation reaches the detector than in the configuration at time t_2. Comparing ΔS with $P(t_1)$ indicates that these regions are

(i) either behind dark squares at time t_1, where no part of the object is projected (direct beam), or,

(ii) that they are behind bright squares at time t_1 if part of the object gets projected too.

This can be explained as follows:
For case *(i)*, it is assumed that the dark square of the primary modulator at time t_1 itself scatters radiation in forward directions which reaches the detector mainly in regions that are directly accessible, i.e. regions that are not shaded by the object. For time t_2, dark squares (material) and bright squares (air) are interchanged. Thus, the former dark square becomes a bright square (air), which does not interact with radiation.
Case *(ii)* can be constituted by a higher contribution of forward scattered radiation originating directly from the projected region of the sample. Since this region of the sample is irradiated with more intensity in the configuration at time t_1 (bright square) than in the inverse configuration at time t_2, and hence, more scattered radiation is generated, this makes case *(ii)* plausible.

While in modulator settings from 2×2 to 16×16 squares, i.e. as the spatial modulation frequency increases, the difference between scatter fluences ΔS steadily decreases, it cannot be resolved for 32×32 squares any more. Here, noise is more dominant. The difference between scatter fluences ΔS is less than ± 7 gray values whereas the scatter signal ranges between 1400 and 3700 gray values as can be deduced from Fig. 5.6.
The observed effects can be explained by the relatively broad spatial distribution of Compton scattered X-ray photons for photon energies found in industrial CT (cf. sec-
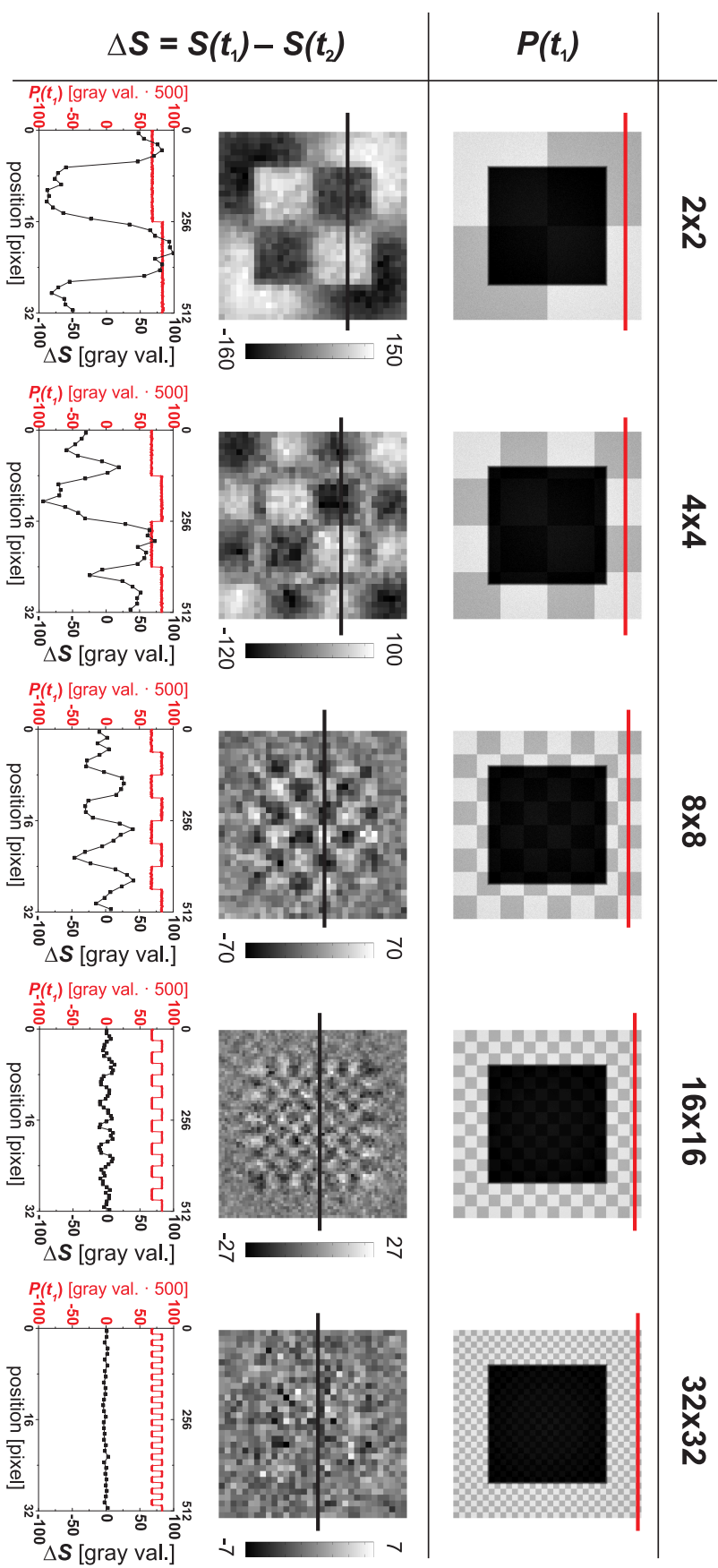
Figure 5.7: Monte-Carlo simulation of a radiographic projection of an aluminum sample and different primary modulator configurations. Primary modulators with checkerboard patterns are simulated with 2×2 up to 32×32 squares. The top row shows primary images for $j=1$ as reference. As the modulation pattern becomes finer, i.e. the spatial frequency increases, the difference between scatter fluences ΔS vanishes as can be seen in the middle row and in the corresponding line profiles also (bottom row). Note that the gray-scale windowing in the middle row is not constant, but adjusted in order to resolve any image patterns.

tion 2.1.4). Also, multiple scattering events will further smear out any incident primary radiation pattern and lead to even broader cones of scattered radiation.

5.2.1.2 Variation of Modulation Strength

Small differences $\Delta S = S(t_1) - S(t_2)$ may be obtained also by a decrease of the modulation strength A as we found from another series of Monte-Carlo simulations. Figure 5.8 exhibits the simulation results. The simulation was conducted in the same way as for the analysis of varying spatial modulation frequencies presented above. In Fig. 5.8, from left to right, the modulation strength decreases from $A = 0.27$, $A = 0.18$, $A = 0.09$ down to $A = 0.04$ for the primary modulator configuration with 4×4 squares. A decreasing modulation strength goes along with a decrease of scatter fluence differences ΔS as expected. However, as explained in section 5.1.3, smaller modulation strengths will lead to larger errors in the scatter estimate. So, an optimum has to be found for the modulation strength A.

5.2.2 Theoretical Analysis

In the last section, by using Monte-Carlo simulations, we have demonstrated that differences between the scatter fluences in the two modulator positions, $S(t_1)$ and $S(t_2)$, become (negligibly) small, if the number of squares is large, i.e. if the spatial modulation frequency is high, and if the modulation strength is moderate. These findings from the Monte-Carlo simulations are a proof for the validity of TPM under certain constraints. In this section, we want to carry out a formal error analysis of the scatter estimation process by TPM using a simple model. Hereby, we address the following two questions:

1. What is the origin of non-vanishing differences between scatter fluences, $\Delta S = S(t_1) - S(t_2)$?

2. How does such a difference ΔS affect the scatter estimation? How large is the resulting systematic error?

5.2.2.1 Non-vanishing Differences between Scatter Fluences

Since the Monte-Carlo simulations in section 5.2.1.1 have shown that the difference in magnitude of the scatter fluences, $\Delta S = S(t_1) - S(t_2)$, is dependent on the spatial frequency of the modulation pattern, we will focus on this aspect here. For a formal analysis, let us consider a 2D model of a parallel-beam scanner for taking radiographic line projections with a one-dimensional detector. According to Eq. (3.2), each pixel x of the one-dimensional detector yields a total signal

$$T(x, t_j) = P(x, t_j) + S(x, t_j) \ , \tag{5.28}$$

where $P(x, t_j) = P_0(x) \cdot f_{\mathrm{mod}}(t_j)$, $f_{\mathrm{mod}}(t_j) = 1 + \frac{A}{2}\left(\cos(\omega_{\mathrm{mod}} \cdot t_j) - 1\right)$ according to Eqs. (5.1) and (5.2). Thereby, we limit our considerations to the practically relevant example of TPM with $N_{\mathrm{mod}} = 2$ as described in section 5.1.2.

For an arbitrary pixel x', the scatter signal $S(x', t_j)$ can be interpreted as the sum of contributions from a number N_{SSS} of single scatter sources (SSS), $s_i(x', t_j)$, which are
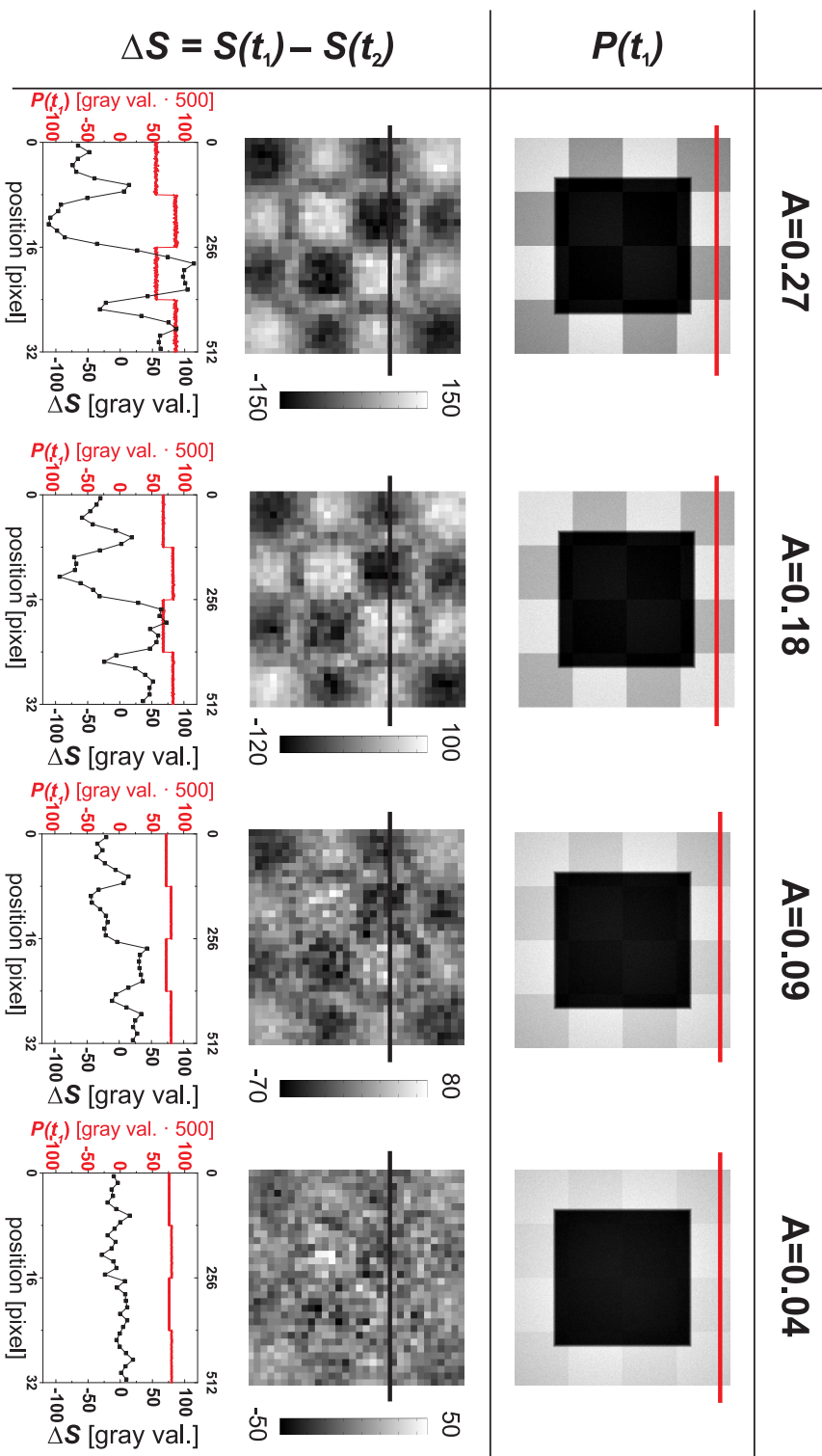
Figure 5.8: Monte-Carlo simulation of a radiographic projection of an aluminum sample and different modulation strengths A of a primary modulator with 4×4 squares. Modulation strengths are $A = 0.27, 0.18, 0.09, 0.04$, from left to right. The top row shows primary images for $j{=}1$ as reference. The middle row displays the differences between scatter fluences ΔS. As the modulation strength A decreases, the ΔS becomes smaller, as expected. This can also be deduced from the corresponding line profiles shown in the bottom row. Note that the gray-scale windowing in the middle row is not constant, but adjusted in order to resolve any image patterns.
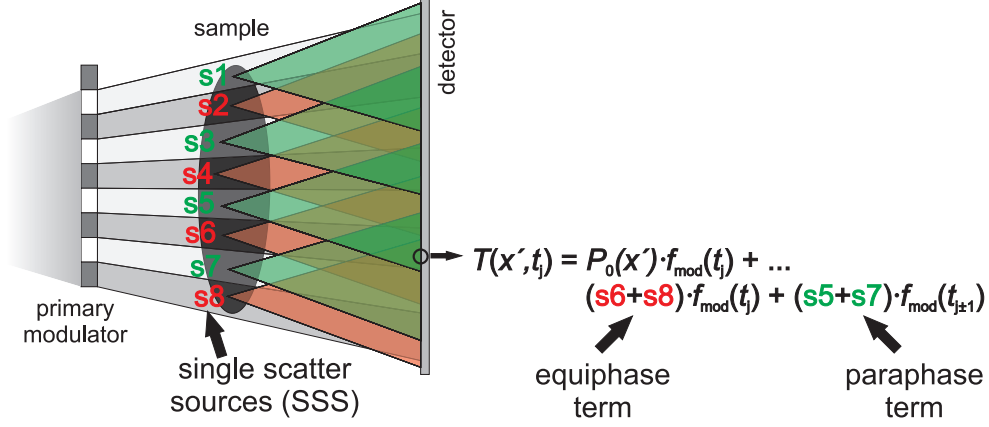
Figure 5.9: Schematic illustration of equi- and paraphase single scatter sources for an arbitrary pixel x'. The total signal at pixel x' consists of the modulated primary part, plus the summation over equi- and paraphase single scatter sources which are modulated themselves.

spatially spread all over the sample. Here, single scatter sources $s_i(x', t_j)$ are to be understood as the locations of initial scatter events (first order scatter events), even for scatter processes of order greater than one. Although spatially uncorrelated, they altogether give rise to the total scatter signal $S(x', t_j)$ detected at pixel x'. With regard to this interpretation, we rewrite Eq. (5.28) as

$$T(x', t_j) = P_0(x') \cdot f_{\mathrm{mod}}(t_j) + \sum_i^{N_{\mathrm{SSS}}} s_i(x', t_j) \ . \tag{5.29}$$

Scattered photons of single scatter sources s_i descend from primary X-rays originally, which in turn are temporally modulated. Thus, each of the single scatter sources individually gets temporally modulated itself as well. Regarding the example with $N_{\mathrm{mod}} = 2$, we can divide the total set of single scatter sources into subsets of *equiphase* and *paraphase* initial scatter sources in respect to the modulation state of the pixel under consideration. The distinction of equi- and paraphase single scatter sources is illustrated schematically in Fig. 5.9 for an arbitrary pixel x' at time t_j. In this illustration, this specific pixel x' is behind a dark square of the modulator. Thus, illustrated as red scatter cones, equiphase single scatter sources are from regions within the sample that are irradiated by primary radiation that has also passed dark squares. On the other hand, marked by green scatter cones, paraphase single scatter sources originate from regions where incident primary radiation is modulated with phase-shift of π with respect to the pixel x' under consideration.

With this distinction, we rewrite Eq. (5.29) as

$$T(x', t_j) = P_0(x') \cdot f_{\mathrm{mod}}(t_j) + \overbrace{\sum_i s_i(x') \cdot f_{\mathrm{mod}}(t_j)}^{\mathrm{equiph.}} + \overbrace{\sum_i s_i(x') \cdot f_{\mathrm{mod}}(t_{j\pm1})}^{\mathrm{paraph.}} , \tag{5.30}$$

where the first summation is over equiphase and the second over paraphase single scatter sources. Note that for single scatter sources in paraphase, the modulation is phase-shifted

by π, i.e. $j \pm 1$ in the second sum. Since only a fraction A of the primary radiation is modulated, we can split Eq. (5.30) into a stationary and a modulated part:

$$T(x', t_j) = \left(1 - \frac{A}{2}\right) \cdot \left[P_0(x') + \overset{\text{equiph.}}{\sum_i} s_i(x') + \overset{\text{paraph.}}{\sum_i} s_i(x')\right] +$$
$$\frac{A}{2} \cdot \cos(\pi \cdot t_j) \left[P_0(x') + \overset{\text{equiph.}}{\sum_i} s_i(x') - \overset{\text{paraph.}}{\sum_i} s_i(x')\right] . \tag{5.31}$$

From the second term, i.e. the modulated part, the TPM method calculates an estimated primary signal $P_{0,\text{est}}(x')$ as described in section 5.1.1. There, we argued that the total scatter signal for pixel x' must not be modulated temporally during primary modulation if the TPM calculation of $P_{0,\text{est}}$ is to be correct. Looking at the second term in Eq. (5.31), note that this requirement is only fulfilled if contributions from equi- and paraphase single scatter sources have the same magnitude and cancel out each other. Thus, for correct primary estimation by TPM, the following has to apply:

$$\overset{\text{equiph.}}{\sum_i} s_i(x') - \overset{\text{paraph.}}{\sum_i} s_i(x') \overset{!}{=} 0 . \tag{5.32}$$

The last equation represents a fundamental requirement for correct scatter estimation with TPM: Single scatter sources need to be equally distributed and of same magnitude between the two modulation phases, e.g. bright and dark squares, when using a checkerboard-like primary modulator. In practice, Eq. (5.32) will not be fulfilled exactly. There will be rather some amount of imbalance between contributions from the two subsets which we denote as

$$\Delta s(x') := \overset{\text{equiph.}}{\sum_i} s_i(x') - \overset{\text{paraph.}}{\sum_i} s_i(x') . \tag{5.33}$$

The greater the imbalance $\Delta s(x')$ is, the greater the error in primary signal estimation, and hence, in scatter signal estimation becomes, as we will describe below.

Within this 2D model description, we are going to address the question of how the imbalance correlates with the spatial distribution of scatterers, and more precisely, with the spatial frequencies of the object. For this purpose, we make use of the Fourier analysis, by which we are able to decompose a given object function into its constituting (spatial) frequencies. In our case, we compress an arbitrary 2D object function into a 1D object function (line) where the scatter originates from. Subsequently, this 1D object can be decomposed into single frequencies, which are here represented as object grids with different periods. The primary modulator is represented by a 1D modulator grid as well. We conduct a simulation where the pitch of the primary modulator grid is constant, d_{Mod}=const., while the object grid is varied in its pitch d_{Obj}. For each pitch of the object grid, we calculate the scatter distributions deterministically for both positions of the primary modulator. From this, we obtain the difference in scatter fluences ΔS between the two positions in dependence of the grid width of the object.

The simulation setup is schematically shown in Fig. 5.10(a). Without loss of generality, we make the following simplifying assumptions with respect to scatter build-up:
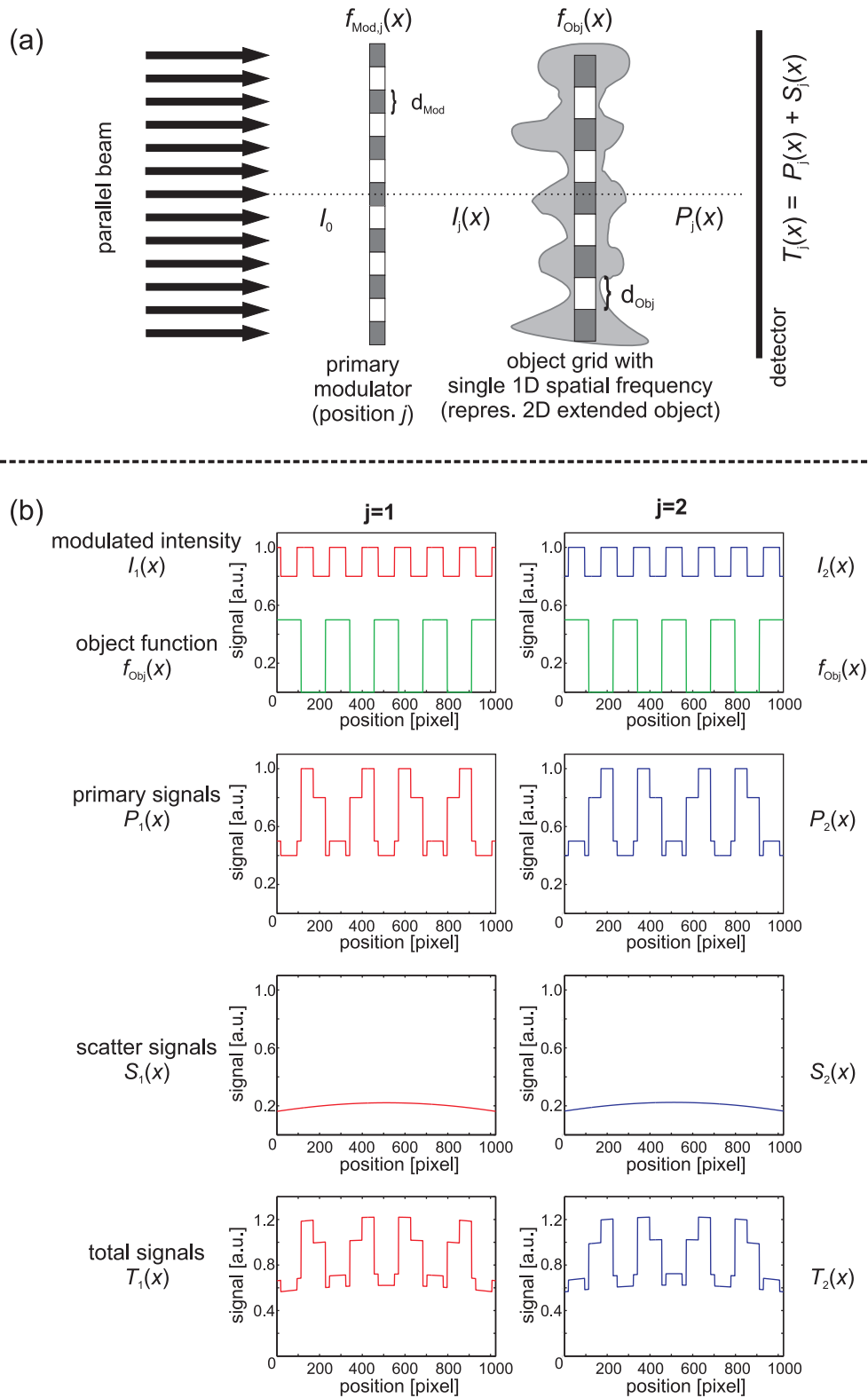
Figure 5.10: (a) Schematic illustration of the simulation setup for studying the change in scatter fluences between the two positions of the primary modulator depending on spatial frequencies of the object. (b) Exemplary model signals calculated for the situation shown in (a). For details see text.

- First, the simulation is limited to only first-order scattered radiation by the object.

- Second, although the object is extended in 2D, scattering occurs only at a single line within the object, e.g. the central line.

- Third, scattered X-ray photons originate from structures within the sample which can be analyzed separately, i.e. for each spatial frequency within the object plane individually as in Fourier analysis.

- Fourth, in order to be able to easily calculate the signals, we consider parallel-beam geometry and a discretized 1D detector of 1024 pixels.

The initial intensity from the X-ray source is given by $I_0 = 1$. The primary modulator grid $f_{\mathrm{Mod},j}$ with modulator pitch d_{Mod} is defined by

$$f_{\mathrm{Mod},j}(x) = \begin{cases} 1, & \text{if } \lfloor \frac{x}{d_{\mathrm{Mod}}} \rfloor \text{ is even } (j{=}1)/\text{odd } (j{=}2), \\ 1 - A, & \text{if } \lfloor \frac{x}{d_{\mathrm{Mod}}} \rfloor \text{ is odd } (j{=}1)/\text{even } (j{=}2), \end{cases} \tag{5.34}$$

where A is the modulation strength. The intensity I_j behind the primary modulator grid is given by

$$I_j(x) = I_0 \cdot f_{\mathrm{Mod},j}(x) \ . \tag{5.35}$$

Furthermore, we define the 1D object function f_{Obj} in a similar way as the modulator function:

$$f_{\mathrm{Obj}}(x) = \begin{cases} 0.5, & \text{if } \lfloor \frac{x}{d_{\mathrm{Mod}}} \rfloor \text{ is even}, \\ 0, & \text{if } \lfloor \frac{x}{d_{\mathrm{Mod}}} \rfloor \text{ is odd}, \end{cases} \tag{5.36}$$

representing a grid with pitch d_{Obj}. For both modulator positions $j{=}1$ and $j{=}2$, the primary signals $P_j(x)$ are calculated from the incident radiation intensity $I_j(x)$ (incident on the sample) and the object function $f_{\mathrm{Obj}}(x)$:

$$P_j(x) = I_j(x) \cdot (1 - f_{\mathrm{Obj}}(x)) \ . \tag{5.37}$$

In our model, scatter functions are simulated by convolution of single scatter sources, given by $I_j(x) \cdot f_{\mathrm{Obj}}(x)$, with a scatter kernel function $S_{\mathrm{kernel}}(x)$,

$$S_j(x) = (I_j(x) \cdot f_{\mathrm{Obj}}(x)) \otimes S_{\mathrm{kernel}}(x) \ . \tag{5.38}$$

For pixels $x = 1 \ldots 1024$, we define the scatter kernel as the sum of angular distributions of Rayleigh and Compton single-scattered photons:

$$S_{\mathrm{kernel}}(x) \propto \frac{\mathrm{d_a}\sigma_{\mathrm{R}}(\theta)}{\mathrm{d}\Omega} + \frac{\mathrm{d_a}\sigma_{\mathrm{C}}^{\mathrm{KN}}(\theta)}{\mathrm{d}\Omega} \ , \quad \text{where } \theta = \arctan\left(x/512\mathrm{pixel} - 1\right). \tag{5.39}$$

Here, $\mathrm{d_a}\sigma_{\mathrm{R}}/\mathrm{d}\Omega$ and $\mathrm{d_a}\sigma_{\mathrm{C}}^{\mathrm{KN}}/\mathrm{d}\Omega$ denote the differential atomic cross sections for Rayleigh and Compton scattering, respectively, as defined before in Eqs. (2.8) and (2.17). Each of the differential cross sections indicates the probability (per unit solid angle) that an incident photon is scattered at scattering angle θ. We obtain the scatter kernel S_{kernel} for parameters which are chosen close to our experimental conditions. Figure 5.11(a)
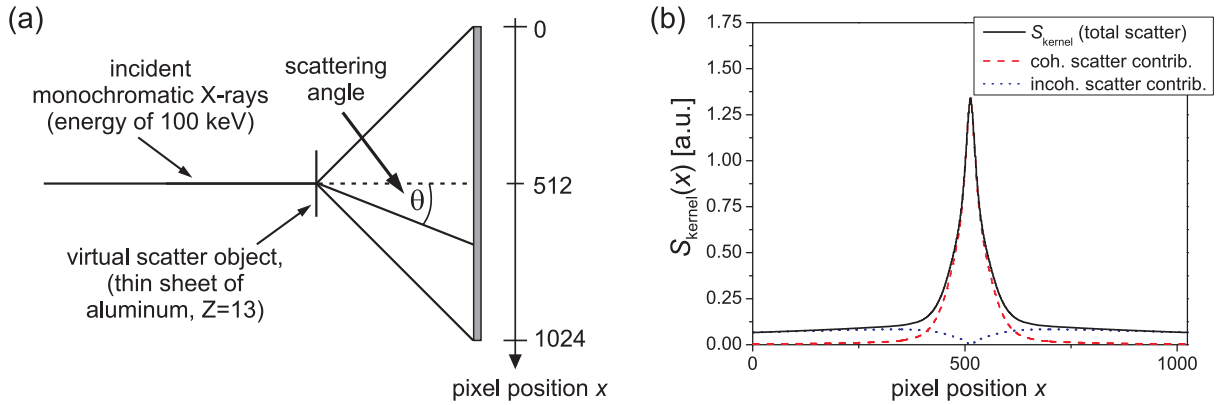
(a)

(b)

Figure 5.11: (a) Schematic illustration of the calculation of the angular scatter distribution described by scatter kernel $S_{\text{kernel}}(x)$. (b) Linear plot of scatter kernel $S_{\text{kernel}}(x)$, calculated as the sum of coherent Rayleigh-scattered and incoherent Compton-scattered photons. For details see text.

shows schematically the assumed setup: a monochromatic pencil beam, i.e. X-ray photons with a photon energy of $100\,\text{keV}$ (which is close to the average energy of a polychromatic $225\,\text{kVp}$ X-ray spectrum), is scattered by a thin sheet of aluminum ($Z{=}13$). The angular distributions of Rayleigh- and Compton-scattered photons is calculated using Eq. (2.8), Eq. (2.17) and the atomic form factors $F(q, Z)$ as well as the incoherent scattering functions $S(q, Z)$ listed in Ref. [Hub+75]. The scattered photons are registered by a one-dimensional detector which forms an angle of 90° with the scattering site (i.e. the scattering site is at a distance which equals half the detector length, cf. Fig. 5.11(a)). Hereby, the scatter kernel $S_{\text{kernel}}(x)$, plotted in Fig. 5.11(b), is obtained.

Finally, the total signals are given by

$$T_j(x) = P_j(x) + S_j(x)\,. \tag{5.40}$$

All signals are exemplarily illustrated in Fig. 5.10(b). In a simulation run where $d_{\text{Mod}} = 15\,(\text{pixel})$ and d_{Obj} is varied from 1 to $1024\,(\text{pixel})$, we obtain the scatter functions $S_j(x)$ for both modulator positions $j = 1, 2$. For each d_{Obj}, we are interested in the mean relative deviation (RelDev) between the two scatter functions obtained,

$$\text{RelDev} = \frac{1}{A}\ \text{mean}_x\left(\frac{\Delta S(x)}{S_{\text{tot}}(x)}\right)\,. \tag{5.41}$$

Thereby,

$$S_{\text{tot}}(x) = \frac{1}{2}(S_1(x) + S_2(x)) \cdot \frac{1}{1 - A/2} \tag{5.42}$$

85

is introduced, i.e. the TPM-undisturbed total scatter signal[1], for normalization of the scatter difference $\Delta S(x)$. Looking back at Eq. (5.31), we see that

$$\Delta S = S_1(x) - S_2(x) = A \cdot \Delta s(x)\,, \tag{5.43}$$

giving a correlation to earlier considerations concerning imbalances between the two sets of single scatter sources in equi- and paraphase described by $\Delta s(x)$. Thus, we can rewrite Eq. (5.41) as mean normalized imbalance $N.I.$ between these two sets:

$$N.I. = \text{mean}_x \left(\frac{\Delta s(x)}{S_{\text{tot}}(x)} \right) \tag{5.44}$$

$$= \text{mean}_x \left(\frac{\sum_i^{\text{equiph.}} s_i - \sum_i^{\text{paraph.}} s_i}{\sum_i^{\text{equiph.}} s_i + \sum_i^{\text{paraph.}} s_i} \right). \tag{5.45}$$

Figure 5.12 exhibits the simulation results in which the normalized imbalance $N.I.$ is plotted against the ratio $d_{\text{Mod}}/d_{\text{Obj}}$. While we find approximate balances for most of the ratios, there are distinct peaks for ratios $d_{\text{Mod}}/d_{\text{Obj}} = (2n + 1)^{\pm 1} = 1, 3^{\pm 1}, 5^{\pm 1}, 7^{\pm 1}, \ldots$, $n \geq 0$. This can be most easily explained for the example $d_{\text{Mod}}/d_{\text{Obj}} = 1$. Here, the pitch of the object grid is the same as the pitch of the modulator grid, therefore, in each of the two modulated projections single scattering sources either lay all behind dark or all behind bright squares, respectively. This is due to the fact that the object model is just a copy of the modulator grid. In this case, the imbalance is maximum, i.e. all single scatter sources are either completely equi- or paraphase, cf. Eq. (5.45). Thus, $N.I. = -1$ for this example. The occurrence of the other peaks can be explained analogously, but with different ratios equi- to paraphase. In fact, for cases where the ratio $d_{\text{Mod}}/d_{\text{Obj}}$ is an odd integer, the normalized imbalance $N.I.$ can be expressed as:

$$|N.I.| = \begin{cases} \frac{d_{\text{Mod}}}{d_{\text{Obj}}}, & \text{if } d_{\text{Mod}} \leq d_{\text{Obj}}, \\ \frac{d_{\text{Obj}}}{d_{\text{Mod}}}, & \text{if } d_{\text{Mod}} > d_{\text{Obj}}. \end{cases} \tag{5.46}$$

A few of these cases are marked in Fig. 5.12. On the other hand, we find the smallest normalized imbalances in equi- and paraphase single scatter sources for even ratios $d_{\text{Mod}}/d_{\text{Obj}} = (2n)^{\pm 1}$, $n \geq 1$.

---

[1]

$$S_{\text{tot}} = \frac{1}{2}(S_1 + S_2) \cdot \frac{1}{1 - A/2}$$

$$= \frac{1}{2} \left\{ \left(1 - \frac{A}{2}\right) \left(\sum_i^{\text{equiph.}} s_i + \sum_i^{\text{paraph.}} s_i \right) + \frac{A}{2} \left(\sum_i^{\text{equiph.}} s_i - \sum_i^{\text{paraph.}} s_i \right) + \ldots \right.$$

$$\left. \left(1 - \frac{A}{2}\right) \left(\sum_i^{\text{equiph.}} s_i + \sum_i^{\text{paraph.}} s_i \right) - \frac{A}{2} \left(\sum_i^{\text{equiph.}} s_i - \sum_i^{\text{paraph.}} s_i \right) \right\} \cdot \frac{1}{1 - A/2}$$

$$= \frac{1}{2} \left(2 \cdot \left(1 - \frac{A}{2}\right) \left(\sum_i^{\text{equiph.}} s_i + \sum_i^{\text{paraph.}} s_i \right) \right) \cdot \frac{1}{1 - A/2}$$

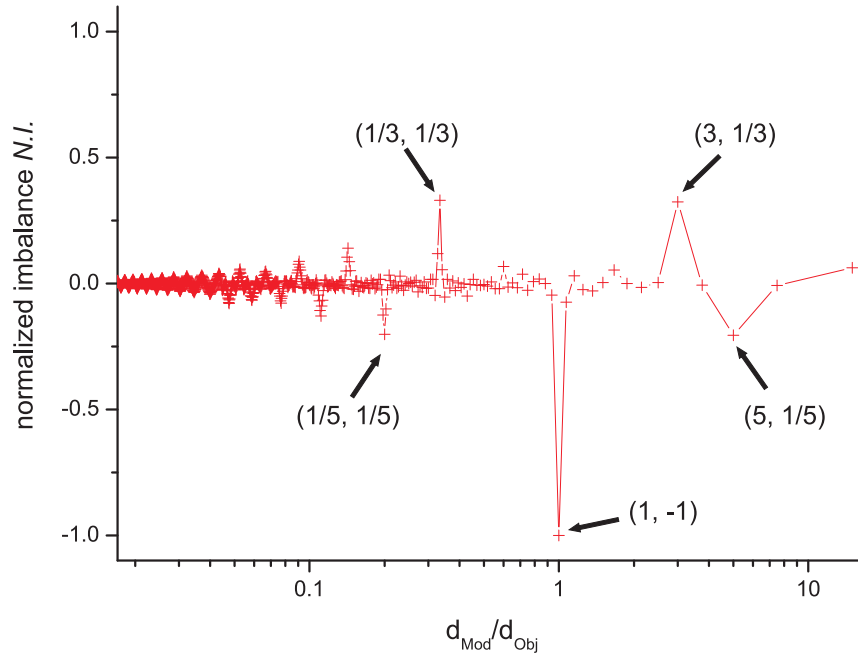$$= \sum_i^{\text{equiph.}} s_i + \sum_i^{\text{paraph.}} s_i$$

Figure 5.12: Simulation result plot of normalized imbalance $N.I.$ against the ratio of the modulator grid pitch over object grid pitch, $d_{\mathrm{Mod}}/d_{\mathrm{Obj}}$, on a logarithmic scale. The imbalance between equi- and paraphase scatter sources is small except for ratios which yield an odd number or its reciprocal.

The analysis so far yields normalized imbalances in scatter fluences for model objects with a single spatial frequency. As stated at the beginning of the model simulation, more complex objects can be created by combining different object grids. The results obtained here can be transferred to this case since, in the simplified model, scatter contributions from different object structures behave additively, i.e. different structures do not impede scatter contributions from others (no effect of depth, no multiple scattering). Thus, in a simulation run where we combine two grids, e.g. with $d_{\mathrm{Mod}}/d_{\mathrm{Obj,1}} = 1$ and $d_{\mathrm{Mod}}/d_{\mathrm{Obj,2}} = 3$, we obtain a normalized imbalance of $(-1 + 0.33)/2 = -0.33$, cf. Fig. 5.12. Here, the single normalized imbalances are summed up and then divided by the number of scatter contributing structures.

5.2.2.2 Systematic Errors in TPM Scatter Estimation

In the last section, we have described the origin of any imbalances between equi- and paraphase single scatter sources. Here, we are going to address the question how such an imbalance affects the scatter estimation procedure. Looking at the model for $N_{\text{mod}} = 2$, with Eq. (5.31) we find in a simplified notation for $t_j = 1, 2$ and omitting coordinate x':

$$T_{1,2} = \left(1 - \frac{A}{2}\right) \cdot \left[P_0 + \underbrace{\overbrace{\sum_i s_i}^{\text{equiph.}} + \overbrace{\sum_i s_i}^{\text{paraph.}}}_{S_{\text{tot}}}\right] \pm \frac{A}{2}\left[P_0 + \underbrace{\overbrace{\sum_i s_i}^{\text{equiph.}} - \overbrace{\sum_i s_i}^{\text{paraph.}}}_{\Delta s}\right] \quad (5.47)$$

$$= \left(1 - \frac{A}{2}\right) \cdot [P_0 + S_{\text{tot}}] \pm \frac{A}{2}[P_0 + \Delta s] \quad (5.48)$$

By inserting this expression for $T_{1,2}$ in Eq. (5.9) for scatter estimation, we obtain

$$S_{\text{est}} = \left(1 - \frac{A}{2}\right)[P_0 + S_{\text{tot}} - (P_0 + \Delta s)] \quad (5.49)$$

$$= \left(1 - \frac{A}{2}\right)[S_{\text{tot}} - \Delta s] . \quad (5.50)$$

This result can be interpreted as follows: the scatter estimation is perfect within noise limits if $\Delta s = 0$, i.e. if equi- and paraphase single scatter sources are balanced in magnitude. Otherwise, their imbalance will lead to a systematic error in the scatter estimate S_{est}. Returning to the analysis of single frequencies of the object from above, for the extreme case $d_{\text{Mod}}/d_{\text{Obj}} = 1$ where all single scatter sources are either completely equi- or completely paraphase, and hence, normalized imbalance $= \Delta s/S_{\text{tot}} = \pm 1$, we find:

$$S_{\text{est}} = \left(1 - \frac{A}{2}\right) \cdot \begin{cases} 0, & \text{all SSS are equiphase,} \\ 2 \cdot S_{\text{tot}}, & \text{all SSS are paraphase.} \end{cases} \quad (5.51)$$

This situation is shown in Fig. 5.13(a). The TPM-calculated scatter signal (black curve) exhibits a strong pattern originating from the modulation profile. Generally, by dividing S_{est} of Eq. (5.50) by $S_{\text{correct}} = \left(1 - \frac{A}{2}\right) S_{\text{tot}}$, we obtain the relative scatter estimation error:

$$\frac{S_{\text{est}}}{S_{\text{correct}}} = 1 \pm \underbrace{\frac{\Delta s}{S_{\text{tot}}}}_{\text{\textit{N.I.}, cf. Eq. (5.44)}} . \quad (5.52)$$

With this simplified model analysis, we conclude that it is essential for correct TPM scatter estimation that for each pixel scatter contributions from equi- and paraphase scatter sources are equally strong in magnitude. If this requirement is not or only insufficiently fulfilled, the resulting imbalance will lead to a spatial pattern remaining in the estimated scatter images that reproduces the spatial modulation pattern.

By the theoretical analysis given here, we can interpret the results from the Monte-Carlo simulation of section 5.2.1.1. There, we obtained difference maps ΔS (Fig. 5.7) which resemble the modulation pattern in the same way as the exaggerated situation depicted
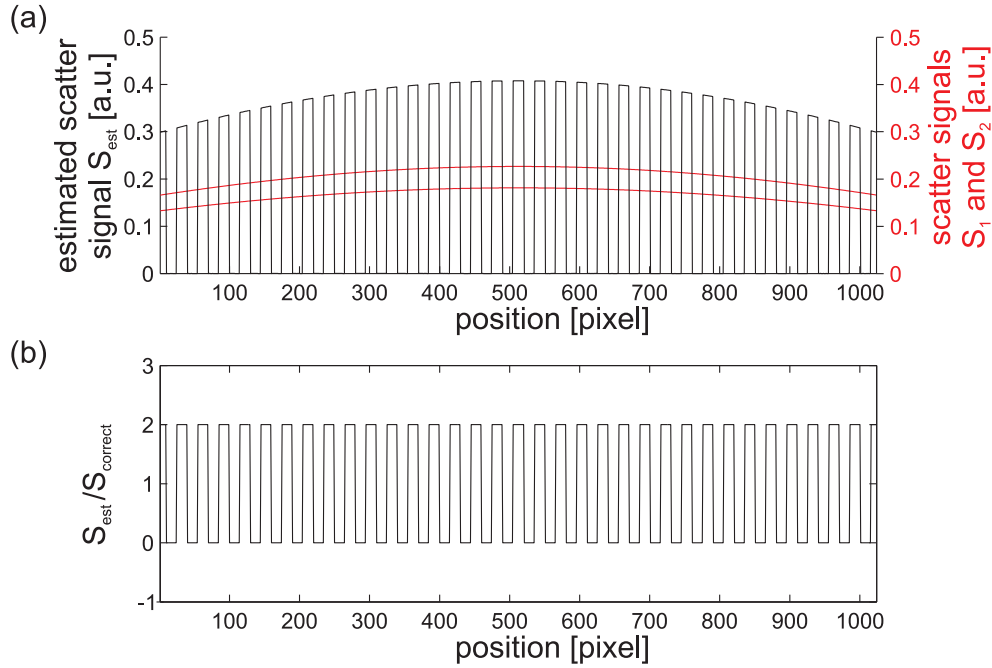
Figure 5.13: (a) Simulated signals for the situation $d_{\mathrm{Mod}}/d_{\mathrm{Obj}} = 1$. In this extreme case, the calculated scatter signal (black curve) shows a strong imprint by the modulation pattern. (b) The ratio $S_{\mathrm{est}}/S_{\mathrm{correct}}$ alternates between 0 (equiphase regions) and 2 (paraphase) as described by Eq. (5.52).

in Fig. 5.13. Both are a result of an imbalance between equi- and paraphase modulated regions which contribute scatter. Furthermore, this imbalance decreases, and hence, ΔS decreases, as the modulation pattern becomes finer. The latter corresponds to decreasing the pitch of the modulator grid, d_{Mod}, while the pitch of the pre-dominant grid within the object function remains the same. This corresponds to the situation that, in Fig. 5.12, we move to the left towards smaller normalized imbalances.

Regarding applications in industrial CBCT, we typically find samples that can be decomposed into constituting frequencies yielding a broad spectral distribution. The same holds true for most applications from the medical field. In general, we expect that the critical frequencies that we investigated in Fig. 5.12 are contained within this spectrum of object frequencies. As derived here, this results in a spatial modulation pattern remaining in the estimated scatter image. However, considering the typically broad distribution of spatial frequencies, critical frequencies are only of minor importance in the overall spectrum. As a result, the modulation patterns remaining in the estimated scatter images exhibit only small magnitudes, as also supported by the Monte-Carlo simulation using fine modulation patterns.

For unfavorable situations where the pre-dominant object frequency is the same as the primary modulator frequency (or odd integers, or their reciprocals), we can improve the TPM scatter estimation by:

- Averaging: From Fig. 5.13(a), we see that averaging over two adjacent modulated regions that are phase-shifted (equi- and paraphase) yields the correct scatter estimate S_{est} whereby $S_{\mathrm{est}}/S_{\mathrm{correct}} = 1$ in Fig. 5.13(b). Averaging will reduce the

spatial resolution of TPM scatter estimation. However, in experimental practice, the frequency of the primary modulation pattern can be chosen sufficiently high, whereby a spatial resolution reduced by factor of two is compatible.

- Filtering: We can use notch-filtering in order to suppress the frequency of the spatial pattern of primary modulation. Thereby, we are unable to detect this specific frequency within the scatter image. A second primary modulator with different spatial modulation frequency could be used in order to gain information about this blind spot.

5.3 Beam-hardening Correction Combined with TPM

For spatial as well as temporal modulation of the primary fluence, the primary radiation has to be modulated in small clusters or pixels within the field of view (FOV). Several possible implementations in form of primary modulators have been presented in section 5.1.2. A primary modulator imprints a specific spatial pattern on beam intensities within the FOV. Since this spatial imprint is technically realized as attenuation of X-rays by matter, beam hardening (BHD) effects may occur (cf. section 2.3.1). The BHD effect leads to different penetration capabilities of radiation behind bright and dark squares: The radiation that passes bright squares without (or with less attenuating) matter is not beam-hardened unlike the radiation that passes dark squares with strongly attenuating matter. At two different stages within the scatter correction method using TPM, this effect has to be taken into account:

1. Before scatter calculation, in order to correctly estimate the amount of scatter: Let us consider how BHD affects the scatter calculation process by TPM. Since the radiation behind dark squares is beam-hardened, i.e. it has stronger penetration capabilities than without the BHD effect, it will give rise to primary signals higher than without BHD when irradiating the sample. During the demodulation process, this leads to the underestimation of primary signals, cf. Eq. (5.7). Thus, the TPM scatter estimate will result in scatter signals which are too large, cf. Eq. (5.9).

2. BHD effects have also to be taken into account after scatter subtraction from the modulated projection and before division by flat-field modulated projection, in order to obtain correct pattern removal by flat-field division.

In the literature concerning spatial primary modulation (SPM), BHD effects have been described [ZBF06; Zhu+09; Gao+10], but have not been taken into account until very recently. Gao *et al.* proposed to reduce BHD effects by selection of an 'optimal material' for the dark squares of the primary modulator [GZF10]. Here, optimal material refers to choosing an element which has one of its absorption edges close to the mean energy of the system spectrum whereby inconsistencies caused by BHD are minimized. Regarding medical applications operating at 120 kVp, the optimal material was found to be erbium [GZF10].

Alternatively and focused on industrial applications operating at greater voltages, we have implemented a beam-hardening correction (BHC) based on the linearization ap-
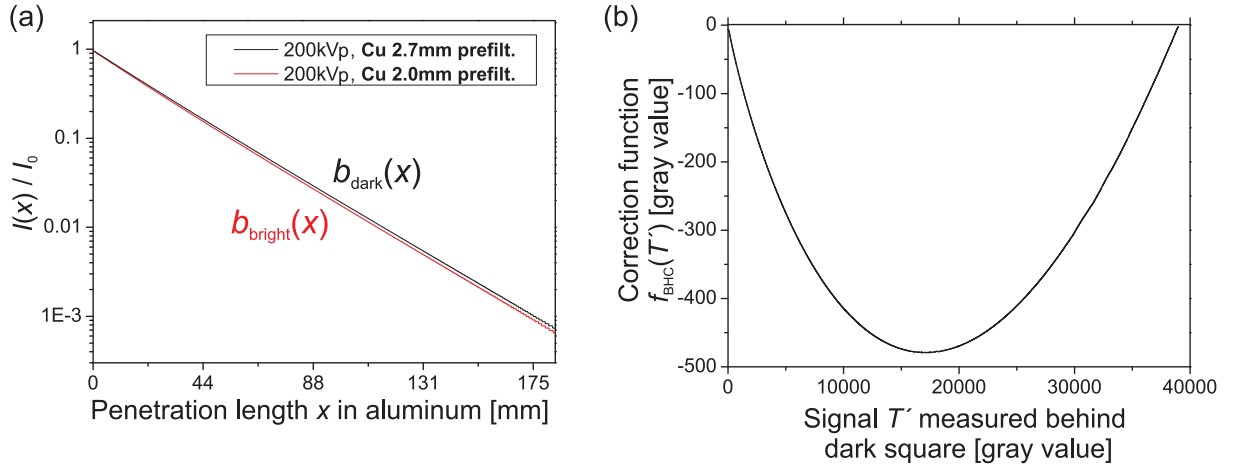
Figure 5.14: (a) Attenuation curves calculated for two different spectra incident on an aluminum wedge. For the bright squares of the primary modulator, we assume a spectrum prefiltered by the tube prefilter of 2.0 mm copper (red curve), while, for the dark squares, the prefilter is effectively enlarged to 2.7 mm (black curve) due to the additional material (0.7 mm copper). (b) From the difference between the two attenuation curves in (a), we construct a lookup table which maps each signal measured behind a dark square, T', to a correction value $f_{\text{BHC}}(T')$.

proach that corrects BHD effects occurring at the dark squares. This correction algorithm is adopted from a BHC applied to entire CT projections in the course of CT volume reconstruction, cf. section 2.3.1. The original approach is presented in Ref. [HM98]. A limitation of the linearization approach relates to the fact that it is theoretically correct only for single-material samples, i.e. samples that can be described by one mass attenuation coefficient μ/ρ (cf. Eq. (2.2)).

We will describe our approach to correct BHD effects occurring at the dark squares of a primary modulator. For this purpose, let us assume that the primary modulator only comprises regions with two different mass attenuation coefficients, e.g. bright and dark squares as with the checkerboard pattern. Furthermore, we assume that bright squares have a negligible BHD effect on incident X-radiation. Hence, the task is to correct the signals that have been measured behind dark squares since they arise from X-rays affected by BHD.

For a given tube voltage (e.g. 200 kVp) and prefilter setting (e.g. 2 mm of copper), we calculate two attenuation functions for X-rays penetrating a continuous wedge made of a single material (e.g. pure aluminum). These two attenuation curves are shown in Fig. 5.14(a) on a logarithmic scale for I/I_0. Assuming a plain prefilter of 2 mm copper for bright squares, we obtain the red attenuation curve $b_{\text{bright}}(x)$, where x is the penetration length within the wedge. For X-rays that have to pass dark squares, and consequentially have to penetrate additional material (e.g. 0.7 mm of copper), we calculate the black attenuation curve $b_{\text{dark}}(x)$ by extending the prefilter correspondingly. Thus, in this case, a total prefilter of 2.7 mm copper is assumed.

As anticipated, the beam-hardened radiation (dark squares) experiences less attenuation while traversing the wedge than the non-hardened radiation (bright squares), thus $b_{\text{dark}}(x)$ is higher than the corresponding curve $b_{\text{bright}}(x)$, cf. Fig. 5.14(a). We calcu-

late the difference between both attenuation curves which yields the correction function $f_{\mathrm{BHC}} = b_{\mathrm{bright}} - b_{\mathrm{dark}}$, depicted in Fig. 5.14(b). Each originally measured, scatter-corrected signal T' from regions shadowed by dark squares is mapped to a correction value $f_{\mathrm{BHC}}(T')$. Before the projections are processed with respect to scatter calculation by TPM, we perform a BHD correction for all pixels (x, y) shadowed by dark squares. This involves the following steps:

1. Given a total signal $T(x, y)$, subtract a scatter estimate $S_{\mathrm{est}}(x, y)$, e.g. by using the calculated scatter image from the CT projection before: $T'(x, y) = T(x, y) - S_{\mathrm{est}}(x, y)$.

2. Use $T'(x, y)$ as lookup value in the lookup table f_{BHC}; this yields a (negative) correction value which is added to $T'(x, y)$, yielding: $T'_{\mathrm{corr}}(x, y) = T'(x, y) + f_{\mathrm{BHC}}[T'(x, y)]$.

3. Undo subtraction of the scatter estimate to yield the BHD-corrected signal T_{corr} for pixel (x, y): $T_{\mathrm{corr}}(x, y) = T'_{\mathrm{corr}}(x, y) + S_{\mathrm{est}}(x, y)$.

Using this beam-hardening correction, we can compensate BHD effects occurring at dark squares. This is a prerequisite for correct estimation of scatter signals by TPM. After the scatter image is calculated and subtracted from the original modulated projection and before the latter is divided by its corresponding flat-field modulated projection, we apply this correction step again in order to remove the modulation pattern correctly.

5.4 Experimental TPM Implementation

In the experiments demonstrating the proposed TPM scatter correction method, the industrial CBCT scanner setup as described in section 4.2.1.1 is used. Before we discuss the experimental investigations in sections 5.5 and 5.6, let us present the TPM specific part of the experimental setup.

5.4.1 Primary Modulator

Our experimental implementation of TPM constitutes a two-point modulation employing a checkerboard pattern which we either step or slide by one square-length as described in section 5.1.2. For this purpose, a primary modulator was manufactured to order as a printed circuit board (PCB) where the checkerboard pattern is realized by PCB etching. Fig. 5.15(a) shows a photograph of the primary modulator mounted within a frame. It is fabricated as a ten-layer PCB with 99×99 square fields, arranged by the etching process as 2D checkerboard pattern with bright squares (PCB base material) and dark squares (copper), each with side lengths of $1 \times 1\,\mathrm{mm}^2$. The copper fields have a total thickness of $0.7\,\mathrm{mm}$. With the tube voltage of $200\,\mathrm{kV}$ and a source prefilter of $2\,\mathrm{mm}$ of copper, we measure a mean transmission of 82% for the copper squares, i.e. the modulation strength is $A = 0.18$ if detector-internal scattering is not considered and not corrected. If we take into account contributions from detector-internal scattering (5500 out of 39000 gray values), cf. section 3.1.3, the modulation strength is $A = 0.21$. This is in good agreement
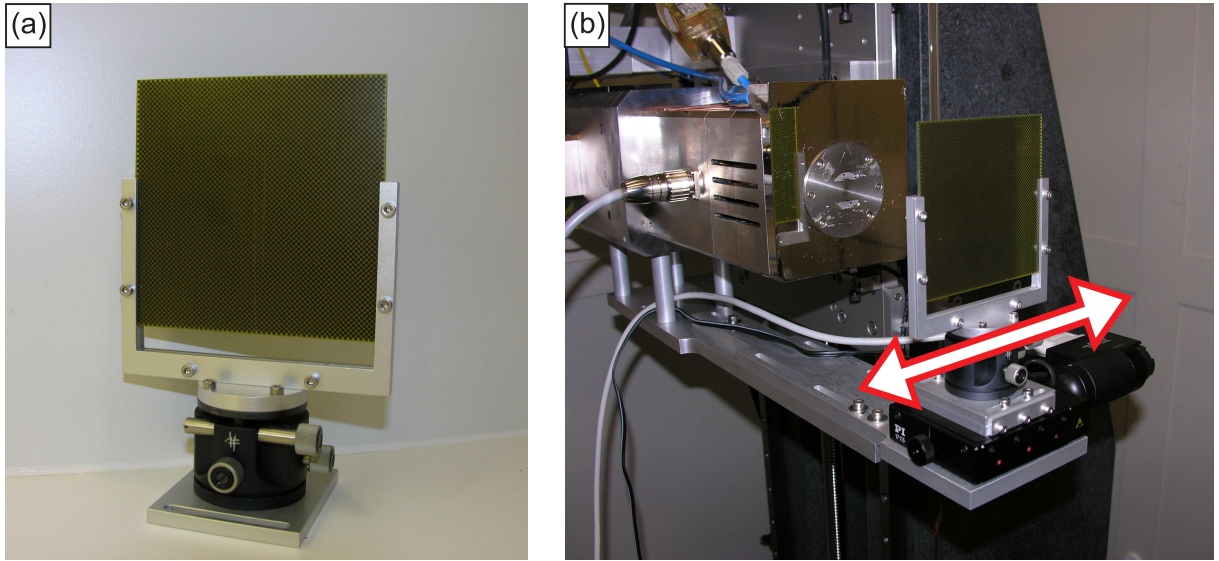
Figure 5.15: (a) The primary modulator, manufactured to order, is arranged as checkerboard pattern and mounted within a frame. (b) Motorized linear translation stage installed in front of X-ray tube for discrete stepping or continuous sliding of the primary modulator.

with simulations which we carried out using a direct-ray simulation tool[2]: Here, we found the target modulation strength of $A = 0.2$ for a design thickness of $0.7\,\text{mm}$ with copper squares.

Choosing a specific modulation strength A for the primary modulator includes the following opposing considerations: according to Eqs. (5.12) and (5.15), on the one hand, a stronger modulation A minimizes noise in the scatter estimate. On the other hand, smaller modulation strengths necessitate less material for attenuation, and thereby minimize beam-hardening effects for signals measured behind dark squares. Furthermore, we conclude from Monte-Carlo simulations in section 5.2.1 that, besides high spatial frequencies of the modulation pattern, a smaller modulation strength lowers systematic errors in the scatter estimation process.

Consequently, a tradeoff between improved scatter estimation and reduced perturbation of the original projection has to be reached. In section 5.1.3, we have derived a correlation (Eq. (5.24)) between the size of averaging regions, N_{pix}, and the modulation strength A. Aiming at averaging regions which correspond to the 99×99 squares of our primary modulator, we obtain $N_{\text{pix}} = 20 \times 20\,\text{pixels} = 400$. For this specific case, Fig. 5.5(a) indicates that an optimum range of modulation strengths with respect to a minimum relative error $\Delta P_{\text{est}}^{\text{TPM}}/\Delta P_0$ is given by $A = 0.22 - 0.26$. Therefore, the modulation strength $A = 0.2$ of our manufactured primary modulator is very close to the specified optimum range.

---

[2]Siemens simulation package for direct-ray simulation (DRASIM) of radiographic projections, cf. [Sti93]. DRASIM uses the EPDL97 database from the Lawrence Livermore National Laboratory (LLNL), cf. [CHK97].

5.4.2 Temporal Primary Modulation Unit and Variants of Modulation

From a technical point of view, we consider two possible variants for moving the primary modulator: (i) the discrete stepping by one square length and (ii) the continuous sliding. In both cases, we employ a linear translation stage (PI-Physik Instrumente, model M-126.PD2) that is installed close to the X-ray tube, cf. Fig. 5.15(b). The primary modulator is mounted onto the linear translation stage and moves horizontally.

In descriptions and illustrations of TPM in section 5.1.2 and particularly in Fig. 5.4, up to this point, we have used **discrete stepping** where the primary modulator is stepped by one square length in between the two modulated projections. As a result, a complete inversion of the modulation for each detector pixel, i.e. bright to dark squares and vice-versa, is obtained. In this case, the modulation strength A is theoretically homogeneous over the entire FOV, assuming parallel-beam geometry and an ideal primary modulator. Thus, in principle, we are able to calculate the scatter signal for each detector pixel individually yielding maximum resolution.

However, in experimental practice, due to imperfections in the fabrication of the primary modulator (bright and dark squares do not have same side lengths) and due to the cone-beam geometry, the modulation is not completely homogeneous. Figure 5.16(a) shows a small section (120×120 pixels out of 1024×1024) of the modulation map $A(x, y)$ where the modulation strength is calculated by

$$A(x, y) = \frac{|P_1(x, y) - P_2(x, y)|}{\max\left[P_1(x, y), P_2(x, y)\right]} \; . \tag{5.53}$$

where $P_{1,2}$ are modulated flat-field projections, i.e. without object, and hence, without scattered radiation. These reference projections are recorded only once for a CT setup; they represent modulated primary signals after exact subtraction of the detector-internal scattering contribution (cf. section 3.1.3).

As can be deduced from Fig. 5.16(a), for most pixels (x, y) the modulation strength A is about 20%, except for a grid-like structure of pixels where the modulation is close to zero due to different side lengths of bright and dark squares of the modulator. According to Eq. (5.12), scatter estimation for small modulation strengths A exhibits large errors. Thus, for TPM scatter estimation, we limit the calculations to regions with $A > 16\%$. Additionally, spatial averaging is performed in the experimental TPM investigations described in sections 5.5 and 5.6. Averaging over pixel clusters of the size of one projected square of the primary modulator strongly improves the signal-to-noise ratio on the one hand, cf. Eq. (5.15), but on the other hand, reduces scatter resolution from 2048×2048 down to 99×99.

An important disadvantage of discretely stepping the primary modulator lies in the fact that a certain amount of time (here: $0.4\,\text{s}$) is needed for the motor shifting process. This is the reason for implementing and testing also another variant: the continuous sliding, which we will describe in the following.

If the primary modulator is **continuous sliding**, it is possible to take the two modulated projections consecutively, i.e. without interruption, and hence, without loss of time. This implies changes to the primary modulation since – in this situation – we cannot realize a
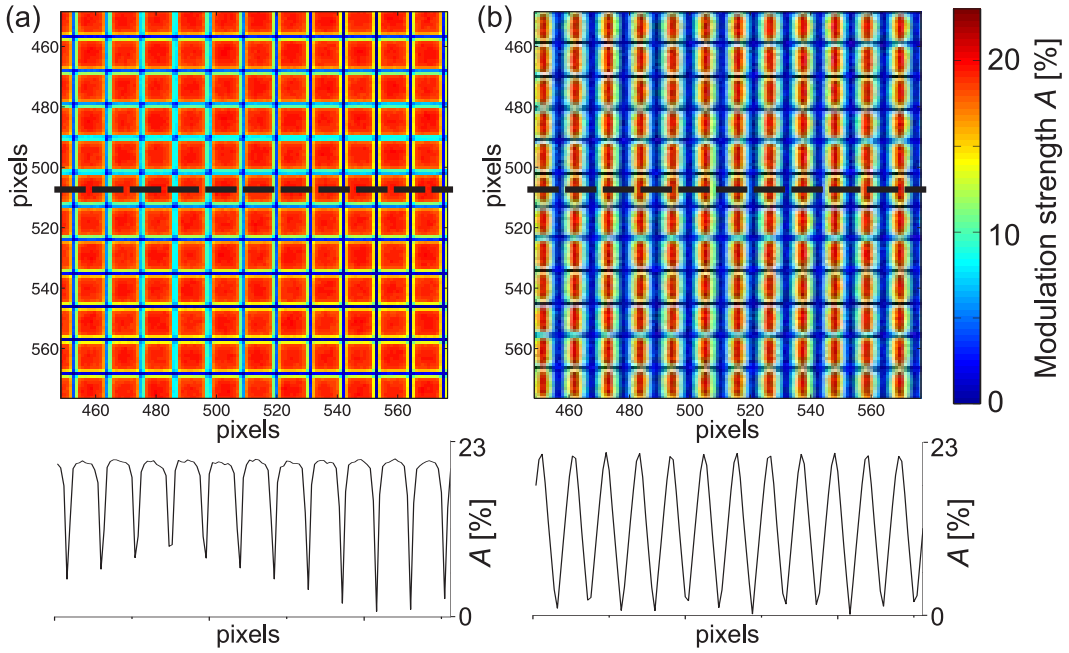
Figure 5.16: Modulation maps $A(x, y)$ of 120×120 pixels (out of 1024×1024 pixels) for (a) discrete stepping and (b) continuous sliding of the primary modulator. In both cases, the primary modulator is horizontally translated by one square length per modulated flat-field projection $P_{1,2}$ (reference projection). Corresponding line profiles are given below.

complete inversion of modulation for the entire FOV as before[3]. In the experiments, we slide the primary modulator at constant speed $v = 0.2\,\mathrm{mm/s}$, i.e. one square length per frame time of one modulated projection (cf. Table 5.1 below). As shown in Fig. 5.16(b), this leads to a horizontal sawtooth-like modulation profile with a frequency equal to the spatial frequency of the modulation pattern. Analogous to the variant of discrete stepping, for TPM scatter calculation we only consider pixels (x, y) where $A(x, y) > 7\%$ here.

The distinction between the two variants, discrete stepping and continuous sliding of the primary modulator, is of technical nature. However, since, in view of industrial applications, the sliding variant is the more interesting of the two, we will focus on this variant in the following.

---

[3] In case of the continuous sliding primary modulator, theoretically homogeneous modulation over the entire FOV could be implemented by increasing the number of modulated projections to $N_{\mathrm{mod}} = \frac{\text{no. of detector pixels}}{\text{no. of squares per row}}$ (or greater). As a result, we would obtain a finer temporal sampling of the signals and get hold of the modulated primary signal for each detector pixel. Let us remark that we have not implemented this technique into the experiment yet.

5.5 Experimental Verification of TPM Scatter Estimation: Comparison of TPM with BSA Scatter Images

Representing a key result of our experimental TPM investigations, we compare scatter estimates of the proposed TPM method with scatter data obtained from the established beam-stop array (BSA) method. The latter has been proven to be robust and reliable for directly measuring scatter signals, see chapter 4.

5.5.1 Experimental Investigations and Results

We perform a CT scan employing the TPM variant with a continuous sliding primary modulator (see section 5.4.2 above). CT parameters applied for this scan and also for the scans described in section 5.6 are given in Table 5.1. The tomographed sample is an aluminum phantom which we specifically designed for demonstration of scatter artifacts. Its dimensions are $8 \times 18 \times 4 \, \text{cm}^3$. Furthermore, it has thin slits cut laterally and transversally as well as drilled boreholes in different planes. It is positioned 8 cm off the axis of rotation, i.e., for the projection angle 0° it is further afar from the detector than for projection angle 180°.

X-ray anode voltage	200 kVp
X-ray tube current	375 μA
Prefilter	2.0 mm copper
Source-object distance (SOD)	75.3 cm
Source-detector distance (SDD)	90.0 cm
Integration time (per angular step)	$2 \times 5.0 \, \text{s}$
No. of angular projections	1080

Table 5.1: CT scan parameters for demonstration of TPM scatter estimation using a primary modulator with a checkerboard pattern.

The primary modulation unit is mounted 21 cm in front of the X-ray tube whereby a total of 95×95 squares is projected onto the detector. Before the actual CT scan, we record flat-field modulated projections $P_{1,2}(x,y)$ in order to generate a modulation map $A(x,y)$ as shown in Fig. 5.16(b). The actual CT scan comprises two modulated projections for each angular step which form the basis for scatter estimation by TPM. In the TPM algorithm, first we apply the beam-hardening correction as specified in section 5.3. However, we do not consider bright and dark squares, but weight the correction value $f_{\text{BHC}}(T')$ according to the individual modulation strength $A(x,y)$ for each pixel (x,y). Subsequently, the BHD-corrected modulated projections are used for TPM calculation of the scatter estimate $S_{\text{est}}(x,y)$ according to Eq. (5.9). This yields a scatter image which is further processed by downsampling to 95×95 points (cf. sections 5.1.3 and 5.4.2).

Furthermore, besides the TPM scan, we conduct a reference measurement to obtain scatter images with an established method that directly measures the scatter signals. Therefore, a short-scan comprising 360 projections is performed where we employ the

beam-stop array method (BSA, cf. section 4.1.1). In this measurement, the CT setting is identical to the CT scan where TPM scatter correction with the continuous sliding primary modulator is applied. Additionally, the BSA is placed into the setup with the primary modulator. The signal decrease due to the attenuation by the PMMA support plate of the BSA is compensated by readjusting the X-ray tube current. Two scans are performed where – after the first scan – the BSA is shifted diagonally by 1.41 cm (half of a diagonal period) in order to obtain a finer sampling grid. From the obtained projection data, BSA scatter images are generated by applying bicubic spline interpolation to the sampled scatter data, analogous to the BHA procedure described in section 4.3.2.

In order to give an overview of the comparison study between TPM and BSA method, Fig. 5.17 displays nine ratios between the BSA and the TPM scatter images. More specifically, it shows color-coded quotient images obtained by pixel-wise division of the BSA generated scatter image by the corresponding TPM scatter image (BSA/TPM-ratio) for the nine projection angles $\alpha_i = 45° \cdot i$, where $i = 0 \dots 8$. Here, small bullets mark the sampling points of the two sets of BSA scans. The green color indicates BSA and TPM scatter signals of equal magnitude. Dark red and dark blue shaded regions represent a deviation of $+30\%$ and -30% (and larger), respectively, of the BSA scatter signal relative to the TPM signal.

For a large part of regions in the quotient images, we find that BSA/TPM-ratios maximally deviate from one by $\pm 10\%$ (light blue to light orange in quotient images). This represents a fairly good agreement between the two methods in general. However, we also notice strong deviations between TPM and BSA scatter signals in regions close to the edges of the sample, particularly on the top edge (all quotient images affected) and along the lateral edges of the sample. By tendency, in these prominent regions, BSA scatter signals are larger than TPM (ratio > 1) when the region is covered by the sample, as in the two examples just mentioned, and smaller (ratio < 1) in regions outside. Examples for the latter can be particularly noticed in quotient images no. 0, 90, 270, and 360 as long blue strips parallel to lateral edges and outside of the sample.

In the following, we limit the comparison of BSA and TPM scatter estimates to representative sampling points of the BSA in which the scatter signal is directly and 'truly' measured, i.e. it is not interpolated. For that purpose, in Fig. 5.18(a), scatter signals estimated by the TPM method are plotted as a function of the projection angle as solid curves. For comparison, the dashed curves show the results from the corresponding BSA measurement. In both cases, the three different curves represent three vertically aligned sampling points which are located in a central region of the scatter images, see markers in the insets of Fig. 5.18(a). Generally, scatter signals obtained from both methods are quantitatively in good agreement over the course of projection angles: Deviations are $\pm 6\%$ at maximum for sampling points 2 and 3 and most of sampling point 1 (except for projection angles around $140°$ and $325°$).

Analogously, Fig. 5.18(b) shows experimental results from the corresponding comparison of TPM and BSA estimated scatter signals for three horizontally aligned sampling points in the center of the scatter images. The sampling points are marked in the inset which depicts the TPM estimated scatter image for the projection angle $270°$. In the graph, blue and green curves represent the outer sampling points which are covered by the sample in
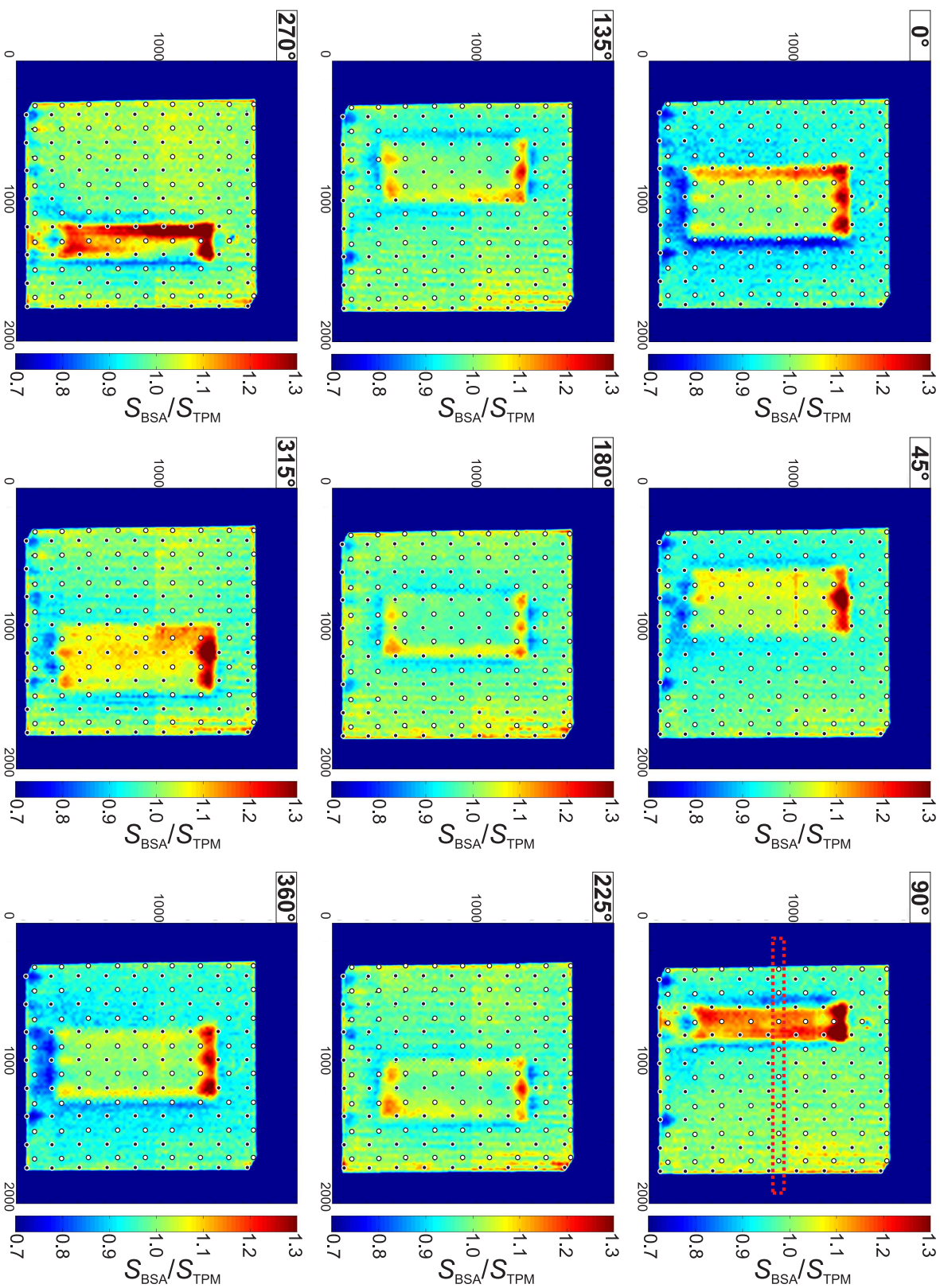
Figure 5.17: Quotient images obtained by dividing BSA scatter images by TPM scatter images. Nine different quotient images are given for equiangular projection angles $\alpha_i = 45° \cdot i$, $i = 0 \ldots 8$. Sampling points of the two BSA-sets are indicated by small bullets. In general, good agreement of TPM and BSA calculated scatter signals is found with maximum deviations of the order of $\pm 10\%$, but prominent regions of larger deviation also exist. For details see text.
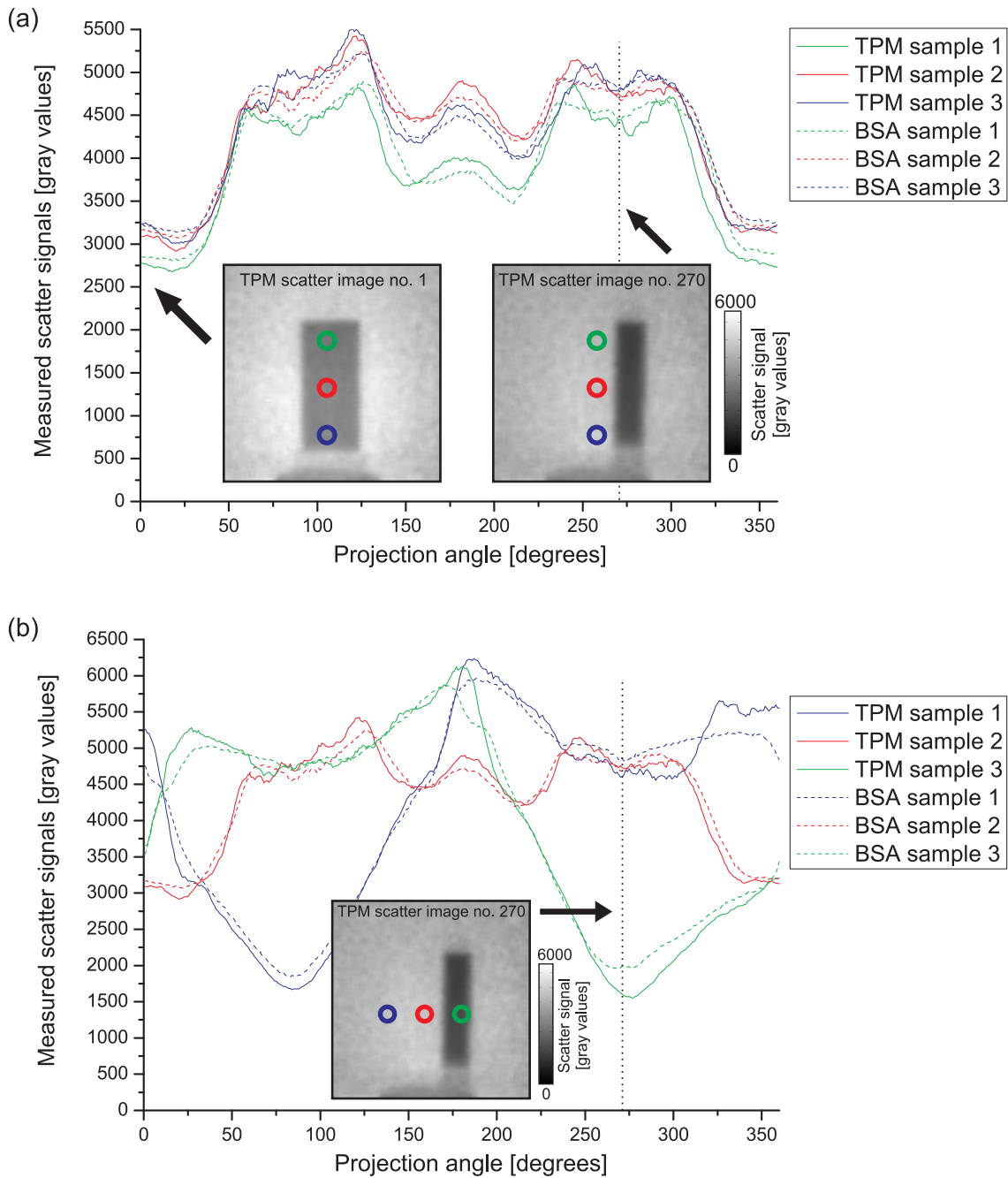
Figure 5.18: Comparison of scatter signals obtained with the TPM method (solid curves) and the BSA method (dashed curves) over the course of 360 projection angles. (a) Scatter signals are given for three vertically aligned sampling points marked in TPM scatter images in the insets. (b) Scatter signals are given for three horizontally aligned sampling points indicated in the TPM scatter image no. 270 depicted in the inset. For details see text.

(a)

(b)
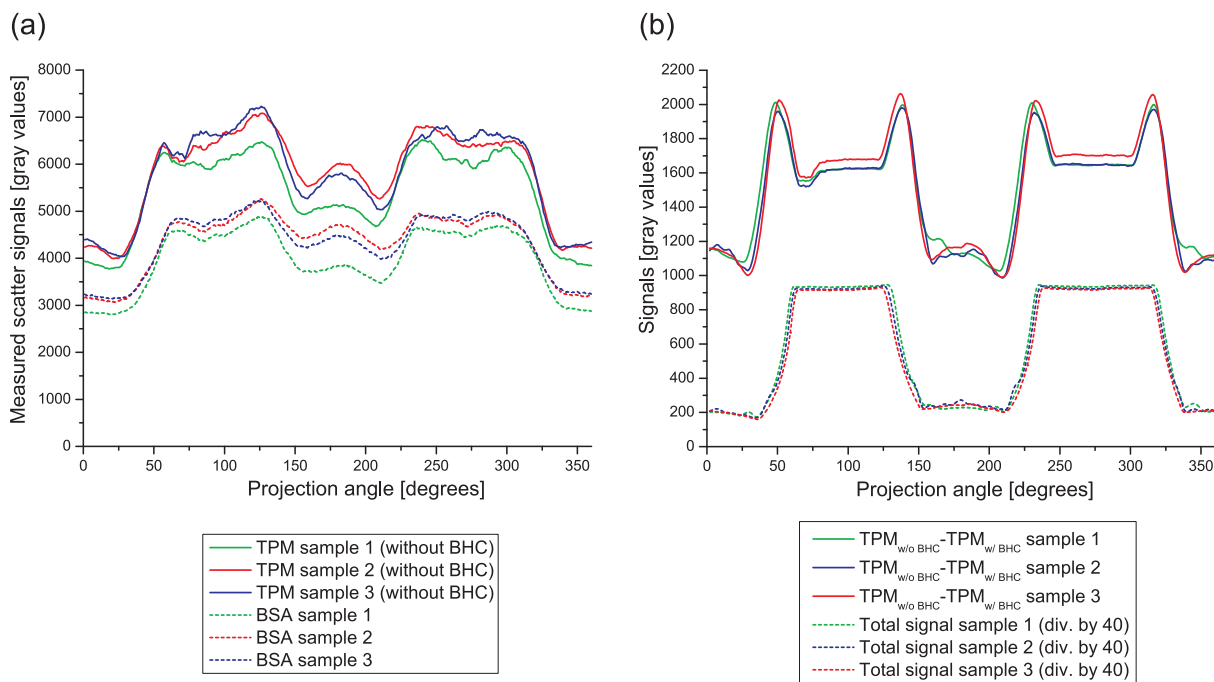
Figure 5.19: (a) Comparison of scatter signals obtained by the TPM method without beam-hardening correction (solid curves) and corresponding BSA-measured scatter signals (dashed curves), comparison analogous to Fig. 5.18(a). (b) Difference plots (solid curves) of TPM-calculated scatter signals $S_{\text{TPM,w/o BHC}} - S_{\text{TPM,w BHC}}$ illustrating the effect of beam-hardening correction as pre-processing step. Down-scaled total signals are given for reference (dashed curves). For details see text.

projections 90° and 270°, respectively. Again, TPM and BSA measured scatter signals agree well.

Influence of Beam-hardening Correction within TPM Method

In order to demonstrate the effect of the beam-hardening correction (BHC) within the TPM method (section 5.3), here we calculate TPM scatter images without BHC for comparison. For this purpose, the same TPM projection data as presented above are used and scatter images are calculated whereas the pre-processing step which compensates for beam-hardening effects, i.e. prior BHC, is omitted. Analogous to Fig. 5.18(a), TPM-calculated scatter signals without BHC are compared with BSA-measured scatter signals in Fig. 5.19(a). Plots are given over the course of 360 projection angles and for the same three sampling points analyzed in Fig. 5.18(a). TPM-calculated scatter signals without prior BHC are considerably larger than BSA-measured scatter signals as expected from the discussion in section 5.3.

In Fig. 5.19(b), the corresponding difference plots of TPM-calculated scatter signals without prior BHC and with prior BHC are given as solid curves. For reference, the corresponding down-scaled total signals are also given for the same sampling points and they exhibit a similar trend as compared to the difference plots. More precisely, the difference in TPM calculated scatter signals without and with prior BHC is dependent on the total

signal since the BHC algorithm takes the latter as input parameter for determining the correction value, cf. Fig. 5.14 in section 5.3. This also explains why the largest differences between TPM scatter signals without and with prior BHC are found in intervals of projection angles where total signals coincide with gray values of about 17000: At this point, the BHC correction value is maximum, cf. Fig. 5.14.

For projection intervals $0° - 25°$, $160° - 200°$, and $335° - 360°$ where the vertically aligned sampling points are covered by the sample shadow, we find differences of $1000 - 1200$ gray values between TPM scatter signals without and with prior BHC. Corresponding to an increase of about 35%, this overestimation of the TPM scatter signal without prior BHC would lead to significant errors in the CT reconstruction process. Thus, we conclude that the BHC pre-processing of TPM projection data is essential for accurate TPM scatter estimation and correction.

5.5.2 Interpretation

The experimental results shown in Figs. 5.17 and 5.18 demonstrate a generally good agreement of estimated scatter images between the TPM and BSA method. Employing the proposed TPM method, we obtain scatter estimates which are within a $\pm 10\%$ range to the scatter data measured using the established BSA technique. This proves that the TPM method is able to measure the scatter distributions very accurately.

However, we noticed a few prominent deviations between the two methods in Fig. 5.17 above. These can be explained by a different sampling and interpolation process between BSA and TPM method. Note that all prominent regions, which are colored dark red and dark blue, lie exactly in between BSA sampling points. Regarding this, it appears that – compared to the TPM method – the scatter data sampling with the BSA is not sufficiently fine. We only measure the scatter signals directly at 16×20 sampling points with the BSA (cf. markers in the quotient images) and apply bicubic spline interpolation in between. Thus, high frequency changes in the scatter signal are not appropriately detected with the BSA using a coarse sampling. In contrast, the TPM sampling grid is 95×95 sampling points for the FOV, and hence, a five- to sixfold finer sampling is obtained with the TPM method.

The observed deviations arising from different sampling resolutions are illustrated exemplary in Fig. 5.20. Here, the central horizontal line profiles of the TPM (green curve) and the BSA (red curve) scatter images for angular step no. 90 are displayed, cf. marked line profile in Fig. 5.17 also. Red circles indicate sampling points where scatter signals are directly measured with the BSA. Additionally, the ratio of the BSA- over the TPM-measured scatter signal is given as black curve (S_{BSA}/S_{TPM}-ratio). Although, in general, the scatter estimates from both methods agree well (S_{BSA}/S_{TPM}-ratios close to one), we notice that in regions where the scatter signal exhibits steep changes (in the vicinity of sample edges as described in section 4.3.3), the S_{BSA}/S_{TPM}-ratio deviates from one. Marked by blue and red arrows in Fig. 5.20, this corresponds and illustrates the occurrence of dark blue and dark red prominent regions close to sample edges in Fig. 5.17. While this explains the observed behavior for regions where the BSA method does not directly measure but interpolates the scatter signal, we still have to consider the prominent dark red regions enclosing BSA sampling points in Fig. 5.17, since, here, the scatter signal is truly measured with the BSA. Note that this mostly concerns the red regions
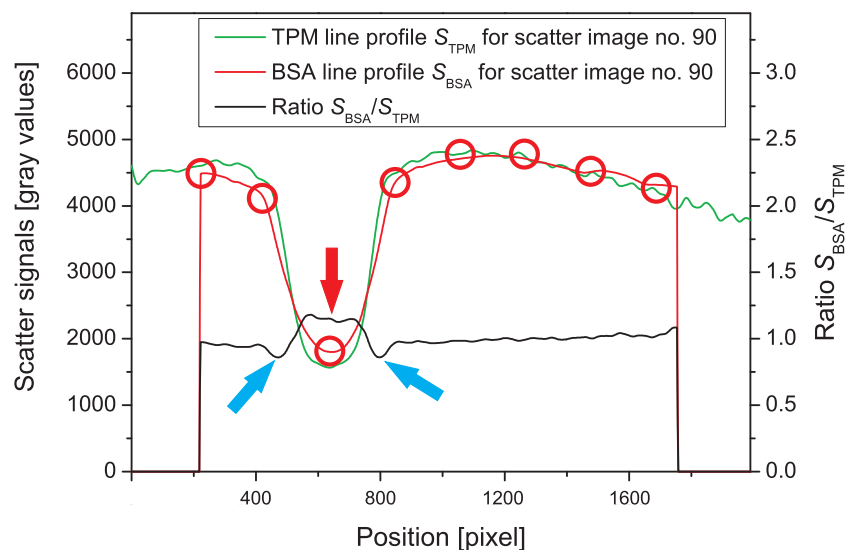
Figure 5.20: Horizontal line profiles in scatter images no. 90 of TPM (green curve) and BSA method (red curve), see also indicated line in quotient image no. 90 in Fig. 5.17. The black curve gives the ratio of BSA-measured scatter signal S_{BSA} divided by TPM-calculated scatter signal S_{TPM}. Red dots indicate sampling points where scatter signals are directly measured within BSA method. Pixel size is $200\,\mu\mathrm{m}$. See text for further explanation.

observed in the quotient images for projection angles 90° and 270°. Also, this applies to the sampling point marked by a red arrow in Fig. 5.20. Analogous to the comparison results obtained for the BSA and BHA methods in section 4.2, here BSA-measured scatter signals are larger than the corresponding TPM-measured signals due to additional scatter from the PMMA support plate of the BSA. This characteristic behavior can also be observed in the graph shown in Fig. 5.18(b): The solid curves indicate that TPM scatter signals are considerably smaller than BSA scatter signals (dashed curves) at projection angles 90° and 270° for object-covered sampling points.

In another aspect, graphs in Fig. 5.18 suggest that BSA- and TPM-measured scatter signals are smaller for regions covered by the sample than for direct-beam regions. In accordance with the results presented in section 4.3 demonstrating the BHA scatter measurement in a CT scan, this is due to detector-internal scattering, cf. interpretation given in section 4.3.3.

Furthermore, in Fig. 5.18(a), scatter signals are higher for projection angles around 180° than at 0°. This is due to the sample positioned 8 cm off the axis of rotation. Hence, the amount of object scatter detected is larger when the sample is closer to the detector at projection angles around 180°.

5.6 Experimental Demonstration of Scatter Correction by Temporal Primary Modulation

As a second key result from the experimental TPM investigations, we demonstrate the successful application of the proposed TPM scatter correction to the CT of a test phan-

tom. A comparison of TPM scatter-corrected CT slices with uncorrected, normal CT slices of the test phantom is performed. Hereby, we prove the capability of the novel TPM method to correct scatter-related artifacts within the reconstructed volume by necessitating only a single CT scan.

5.6.1 Experimental Investigations and Results

In addition to the CT scan where TPM is applied with a continuous sliding primary modulator and which is described in detail in section 5.5.1, we perform a reference CT as normal scan without scatter correction means. In the following, we refer to these two scans as TPM (scatter-corrected) CT and normal (uncorrected) CT. The normal CT is acquired under the same conditions and with the same parameters as the TPM CT (see Table 5.1). In both scans, the tomographed sample is the test phantom specifically designed for demonstration of scatter artifacts that is also described in more detail in section 5.5.1 above.

For scatter correction of the acquired TPM CT, we use the TPM scatter images that have already been calculated for comparison with BSA scatter data as described in section 5.5.1. A detailed description of the exact procedure of calculating TPM scatter images is given there. In order to correct scatter in the acquired TPM projections, we perform the following steps for each projection angle i:

1. From the two modulated TPM projections $j = 1, 2$, we subtract the corresponding TPM scatter image which has been calculated before. This yields two scatter-corrected, modulated projections.

2. For both scatter-corrected modulated projections, we correct beam-hardening effects by the approach described in section 5.3 while the first and last step are omitted. Due to the fact that we already have subtracted the estimated scatter contribution we can omit the first step, and we do not add scatter at the end of the procedure (last step). This yields scatter- plus beam-hardening corrected, modulated projections.

3. For each scatter- plus beam-hardening corrected, modulated projection, we undo the modulation through division by the corresponding flat-field modulated projection (reference projection). This yields scatter- and beam-hardening corrected, unmodulated projections, i.e. completely corrected projections.

4. Since $N_{\mathrm{mod}} = 2$, we obtain two completely corrected projections for each angular step i. In order to improve the SNR, we average over these two and obtain the corrected CT projection i that is used for reconstruction.

In Fig. 5.21, a comparison is shown that illustrates the effect of beam-hardening correction (BHC) in step 2, which we also call post-BHC due to its application after the TPM scatter correction. Figure 5.21(b) shows a scatter- plus beam-hardening corrected projection $j=1$ (unmodulated) from the TPM scan after we have performed steps 1–3. The modulation pattern is not visible any more. Furthermore, the corresponding line profile, which is given as green curve in Fig. 5.21(d), indicates that the modulation has been removed. However,
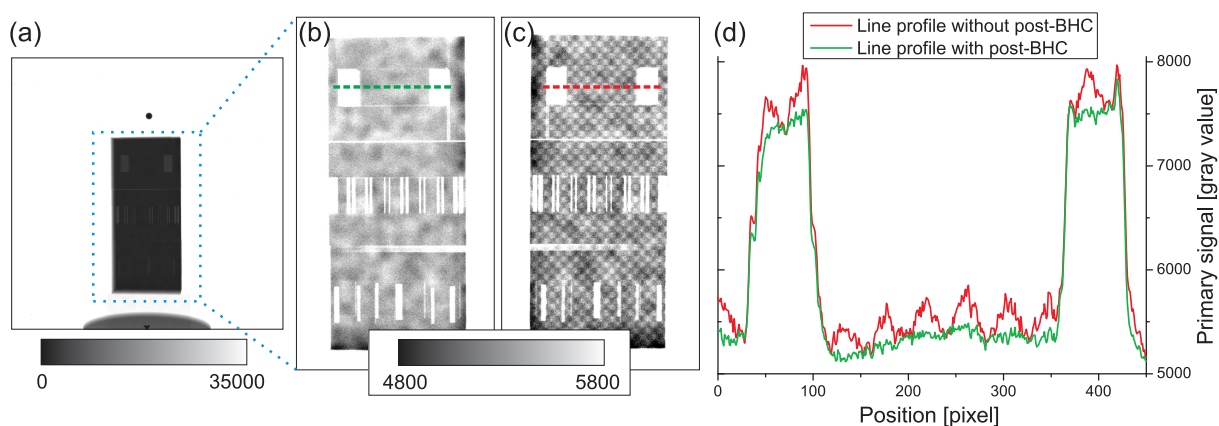
Figure 5.21: (a) Corrected CT projection i=15 (out of 1080) of aluminum test phantom where slits are cut for scatter artifact demonstration purposes. Panel (b) displays object regions of the scatter- plus beam-hardening corrected projection j=1 where gray-level windowing is set to a small range in order to make potential patterns visible. In panel (c), beam-hardening correction has been omitted. (d) Corresponding line profiles for indicated lines in (b) and (c).

if we omit the post-BHC, the modulation pattern will not be completely removed by the flat-field division as can be seen by the corresponding projection j=1 in Fig. 5.21(c) where only steps 1 and 3 have been applied. Also, the corresponding line profile, which is given as red curve in Fig. 5.21(d), clearly exhibits modulation patterns. If these were left uncorrected in the final CT projections, this could lead to the formation of ring artifacts in the reconstructed CT volume. We conclude that the post-BHC, performed in the second step, is essential for correct elimination of the modulation pattern in the third step.

For both the TPM CT and the normal CT scan, reconstructions are computed by an FDK algorithm (cf. section 2.2.3.2). Here, a beam-hardening correction for entire CT projections based on the linearization approach is applied within the reconstruction process (cf. section 2.3.1). Exemplary axial slices of the reconstructed CT volumes are shown in Fig. 5.22, where panels (a)–(c) display the TPM scatter-corrected CT while panels (d)–(f) show normal CT slices that are left uncorrected. Corresponding line profiles are given beneath in panels (g)–(i).

For further analysis, Table 5.2 lists the contrast values of the 15 slits found in the axial CT slices in Fig. 5.22(f) for the uncorrected CT (fourth column in Table 5.2) and in Fig. 5.22(c) for the scatter-corrected CT (fifth column). Here, the numbering is as indicated in Fig. 5.22(c). The table is sorted in ascending order of ratios of the slit widths to the voxel size, which is $335\,\mu\text{m}$.

5.6.2 Interpretation

We discuss the results obtained from the TPM scatter-corrected CT and from the normal, uncorrected CT, as illustrated in Fig. 5.22 for comparison. For a more detailed discussion of scatter artifacts in general, we refer to section 3.2.
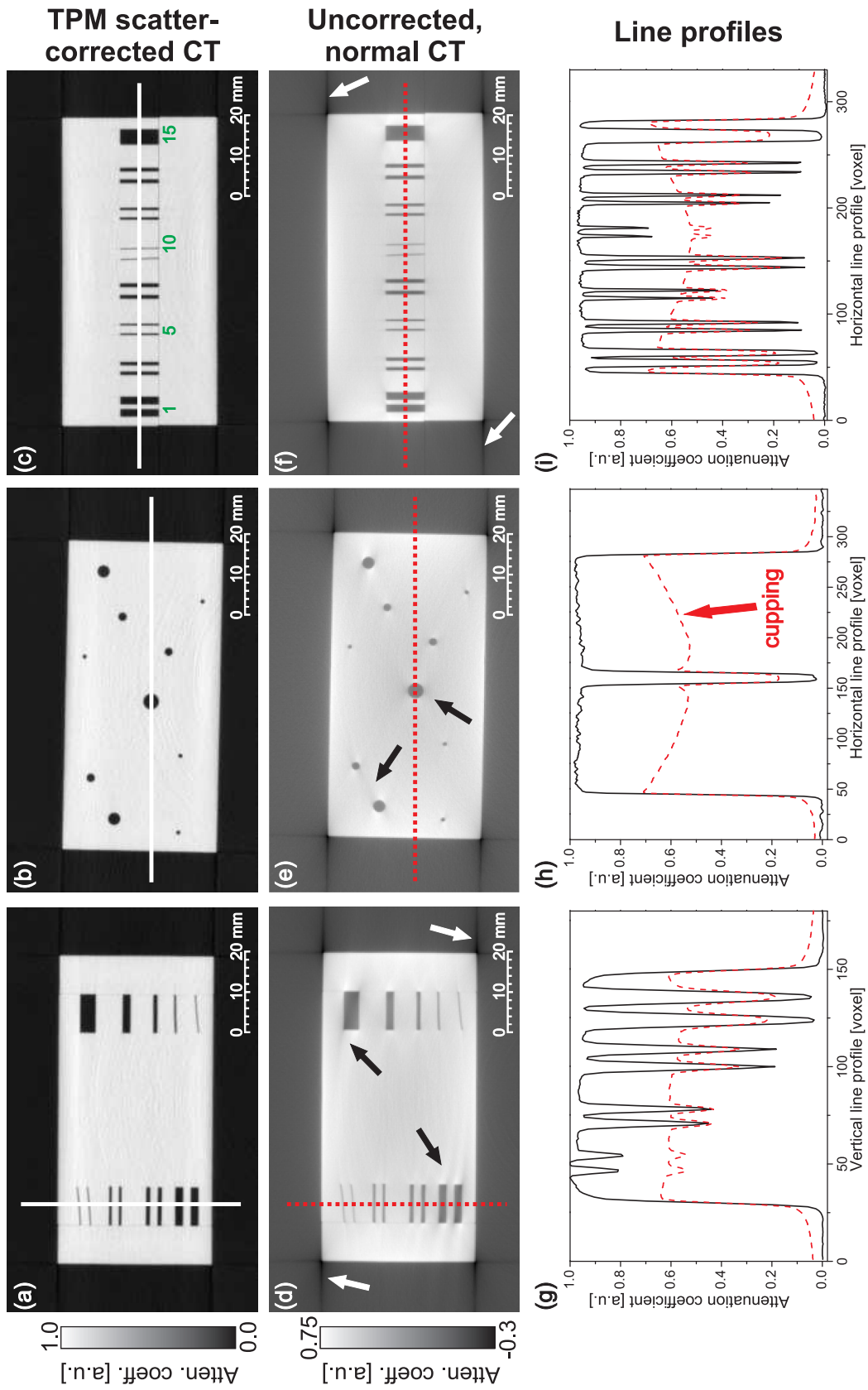
Figure 5.22: (a)–(c) TPM scatter-corrected axial CT slices (TPM variant employing a continuous sliding primary modulator). (d)–(f) show the corresponding CT slices from a normal CT without scatter correction. (g)–(i) Corresponding line profiles. Voxel size is 335 μm. Contrast values for slits in (c) and (f) are given in Table 5.2. For details see text.

105

Ratio slit width to voxel size	Slit no.	Contrast simulated CT [%]	Contrast uncorr. CT [%]	Contrast TPM-corr. CT [%]	Deviation uncorr. CT to Sim. [%-points]	Deviation corr. CT to Sim. [%-points]
0.5	9	31	24	30	-7	-1
0.5	10	31	24	31	-7	0
1.5	5	78	43	70	-35	-8
1.5	6	77	50	64	-27	-13
1.5	11	94	60	77	-34	-17
1.5	12	94	60	80	-34	-14
2.4	3	100	64	89	-36	-11
2.4	4	100	67	90	-33	-10
3.0	7	100	64	91	-36	-9
3.0	8	100	65	91	-35	-9
3.0	13	100	70	91	-30	-9
3.0	14	100	67	91	-33	-9
6.0	1	100	71	97	-29	-3
6.0	2	100	69	97	-31	-3
12.0	15	100	79	99	-21	-1

Table 5.2: Contrast values of the 15 slits in axial CT slices, given for simulated, ideal CT (cf. section 3.2), for the uncorrected CT and for the TPM scatter-corrected CT, see Fig. 5.22(f) and (c), (c) also for numbering. Deviations of the uncorrected CT and the TPM scatter-corrected CT to the simulated, ideal CT are given in the last two columns. Voxel size is 335 µm.

First of all, note a prominent visual difference in scatter-corrected and uncorrected CT slices, i.e. the sample in the uncorrected slices appears to have bulging bright edges and a rather dark central region which renders the appearance of the sample to a bulbous form. This scatter artifact is called cupping artifact and it is particularly evident from corresponding line profiles (red curves): here, although the sample is made from homogeneous material, the red line profiles show a strong downside-bending (cupping). In contrast, the scatter-corrected CT slices do neither show this artifact visually nor quantitatively in the line profiles (black curves). Instead, the line profiles exhibit a nearly perfect rectangular shape in this case. Also, note when considering edge sharpness, that the uncorrected CT line profiles show a slow and smooth increase at the bottom part of the line profiles. This will negatively affect dimensional measuring tasks if left uncorrected.

Second, the sample features different slits and holes for contrast studies. Note the improved visibility of the slits and holes in the corrected CT slices due to larger contrast. This is also illustrated by the corresponding line profiles which clearly show gain in contrast. Quantitatively, Table 5.2 lists contrast values for the 15 slits displayed in Fig. 5.22(c) and (f), where the numbering is as indicated in Fig. 5.22(c). For comparison, contrast values are also given for the simulated, ideal CT of the same object which we have used as model for demonstration of scatter artifacts in section 3.2. Furthermore, deviations of contrast values of the uncorrected CT and of the TPM scatter-corrected CT

to the simulated CT are given in the last two columns of Table 5.2. As indicated by the simulated CT contrasts, nine slits with a ratio of slit width to voxel size of 2.4 or greater are wide enough to exhibit full contrast (100%). For these slits, we find contrast values of $65 - 70\%$ for the uncorrected CT, while the corresponding contrast values of the TPM scatter-corrected CT are 90% or greater. In other words, deviations of about $30 - 35\%$ in the uncorrected CT can be reduced to 10% and less in the corrected CT. Similar results are obtained for the transversally cut slits (Fig. 5.22(a) and (d)). Generally, a higher contrast improves detectability of small structure details, such as cracks, flaws etc.

Third, note another typical scatter artifact, i.e. the occurrence of streaks between high-contrast elements or along edges and corners. In the uncorrected CT slices in Fig. 5.22(d)–(f), some of the occurring streak artifacts are marked by bright and dark arrows. On the other hand, streaks are greatly suppressed in the scatter-corrected CT slices in Fig. 5.22(a)–(c).

When employing a modulation device such as the primary modulator within each CT projection, concerns arise that spatial modulation patterns might remain in final projections used for CT reconstruction. This may lead to the formation of pronounced ring artifacts. In section 5.6.1, we have analyzed that the flat-field division successfully removes modulation patterns from projections used for reconstruction.
However, in the scatter-corrected CT slices shown in Fig. 5.22(a)–(c), we notice moderate occurrence of ring artifacts. In contrast, we cannot visually recognize any ring artifacts in the reference CT slices from the normal CT scan without scatter correction. This raises the question of whether TPM scatter correction causes the formation of ring artifacts.
In order to investigate this issue, we perform the following comparison: A reference CT reconstruction based on BSA scatter-corrected and unmodulated CT projections is performed whereby TPM is completely excluded from the process. Here, BSA scatter images are taken from the comparison measurements described in section 5.5. We note that the reference CT without TPM also exhibits ring artifacts which are of the same magnitude as in the TPM scatter-corrected CT slices shown in Fig. 5.22(a)–(c). Thus, we conclude that ring artifacts do not originate from TPM. The detector calibration has been performed within the standard experimental preparation, but it seems to cause ring artifact formation. Advanced methods for detector calibration should be investigated in order to reduce the formation of ring artifacts in both BSA- and TPM-corrected CTs.
Moreover, ring artifacts only become visible in the scatter-corrected CT slices, either by TPM or by BSA, and are not visible in the uncorrected CT (Fig. 5.22(d)–(f)). This is due to two reasons: First, the cupping artifact introduces a steep gradient in the line profile superimposing the fluctuations from the ring artifacts. This makes them less clearly visible. Second, projection signals are larger if scatter is not corrected, thus a detector miscalibration is less prominent compared to the situation when scatter is corrected by subtraction.

At this point, let us remark that we have also implemented the TPM variant where the primary modulator is discretely stepped (section 5.4.2) and that we have performed an analogous comparison of TPM scatter-corrected CT to normal CT as shown in Fig. 5.22. The CT results for this variant are given in the appendix B. Concerning the correction of scatter-related artifacts, our results indicate that TPM scatter correction with the variant

of a discrete stepping primary modulator are almost identical as with the continuous sliding primary modulator which has been presented here. However, an import technical difference is given by the motor shifting times in the discrete stepping variant which necessitate longer total scan times. Shifting times amount to $0.4\,$s per step. In contrast, for the TPM CT scan with continuous sliding primary modulator and the corresponding normal CT without scatter correction presented here, scan times were exactly the same.

Concluding this section, we have successfully demonstrated that the proposed TPM method eliminates scatter-related artifacts in the reconstructed CT. Moreover, with the TPM method employing a continuous sliding primary modulator, scatter correction is possible without additional scan time and without additional dose.

5.7 Discussion

In chapter 5, we have presented a novel method for scatter correction based on temporal primary modulation (TPM). The distinct feature of TPM scatter correction compared to other techniques lies in the fact that it can be performed without additional scan time, i.e. it can be integrated into the normal CT scan. This represents a major advantage over other scatter correction methods, e.g. beam-stopper based methods that we have discussed in chapter 4.

Moreover, based on the theoretical considerations from sections 5.1.1 and 5.1.2, we conclude that the TPM method – in principle – offers spatial resolution only limited by the resolution of the detector. In experimental practice, however, a high noise level in the scatter estimates, as derived in section 5.1.3, may necessitate spatial averaging over pixel clusters, which lowers spatial resolution but can be arbitrarily adjusted. A different approach for reducing noise in the scatter estimates is extending the integration time of each modulated projection which yields an improved SNR in the measured signals.

For the experimental investigations presented in sections 5.5 and 5.6, we have essentially downsampled the resulting TPM scatter image to a frequency equal to the primary modulator's spatial modulation frequency. The latter is given by the primary modulator which features 99×99 squares in our case. Even with strong spatial averaging in the described situation (downsampling from 2048×2048 to 95×95 pixels), we are able to calculate scatter images by TPM – without extra scan –that exhibit a five- to sixfold finer resolution than two sets of combined BSA measurements.

In another aspect, the comparison of TPM- and BSA-measured scatter data presented in section 5.5 shows good agreement between the two methods at sampling points where the BSA truly and directly measures the scatter signal. Deviations between the TPM- and BSA-measured scatter signals are of the order of 6% or less. This represents an experimental verification of the proposed TPM method with a standard technique for measuring scatter contributions which has been established for a long time.

In section 5.6, we have successfully demonstrated the application of TPM scatter correction in a CT scan of a test phantom. In comparison to uncorrected CT slices from a normal CT scan without scatter correction, the TPM scatter-corrected CT clearly shows elimination, or at least very good suppression of scatter-related artifacts. Here, the cupping artifact is eliminated, streaks are greatly suppressed and the contrast of slits cut

in the test phantom is enhanced. As a result, the deviations of contrast values to ideal contrast values of a simulated CT could be lowered from about $30 - 35\%$ to 10% or less. As demonstrated, this is performed without extending the scan time of the normal CT scan. The experimental demonstration of TPM scatter correction in a CT scan presented here, which comprises the implementation of two-point modulation, a continuous sliding primary modulator as well as a beam-hardening correction for modulated regions, constitutes a further verification of the TPM method.

As explained in the beginning, we have devised the scatter correction method based on temporal primary modulation (TPM) when we performed experiments with a similar technique: the scatter correction by spatial primary modulation (SPM). Since both methods are related to each other, and SPM scatter correction also offers the advantage to measure scatter contributions within the normal CT scan, a comparison of both methods is worthwhile. Thus, the remainder of this discussion is a theoretical and contrasting juxtaposition of SPM and TPM methods. For this purpose, first we are going to give a concise overview of SPM. For a detailed description of SPM scatter correction, we refer to the conceptual and theoretical considerations by Maltz *et al.* [Mal+05] and the experimental demonstration of SPM scatter correction by Zhu *et al.* [ZBF06].

The key idea in SPM is that in each single CT projection the primary fluence is spatially amplitude modulated while the scatter fluence is not. Zhu *et al.* insert a stationary primary modulator with checkerboard pattern between X-ray tube and sample/patient in order to imprint a spatially repetitive modulation pattern onto the primary fluence. As a result, in the spatial frequency domain, primary signals are replicated as they are convolved with the modulation function which (theoretically) is a delta function at a frequency given by the reciprocal period of the modulation pattern. Thus, in the spatial frequency domain, we find a broad background of unmodulated signals (primary and scatter) superimposed by the spectral copies that only contain primary signals. This process is illustrated in Fig. 5.23(a) showing a radiographic projection without, and in Fig. 5.23(c) with the primary modulator in place. Figure 5.23(b) and (d) display the corresponding spatial frequency domains where the amplitude is color-coded on a logarithmic scale. If we assume that the spectral copies of the primary signals are not affected by unmodulated signals, i.e. they do not overlap, a theoretical exact reconstruction of primary signals is possible. Hereby, the maximum restorable primary frequency is given by half of the modulation frequency due to cut-off filtering that is used for separation of modulated from unmodulated signals.

To summarize this overview, note that SPM and TPM build on the same hardware in order to manipulate the primary photon fluence, but that they have different domains of modulation, and consequently, of demodulation: the spatial versus the temporal domain.

We are now able to compare the SPM and TPM scatter correction methods from a theoretical point of view and to comprehend some of the inherent limitations of SPM that are overcome by TPM.

First of all and most important, in practice, with SPM, spectral copies of the primary signals overlap with the unmodulated spectrum in frequency space (Fig. 5.23). Arising from high spatial frequencies present in the image, particularly from edges and high contrast regions of the sample, this spectral overlapping leads to an inaccurate estimation of primary signals, as illustrated in Fig. 5.24(a). Here, an SPM-calculated primary estimate
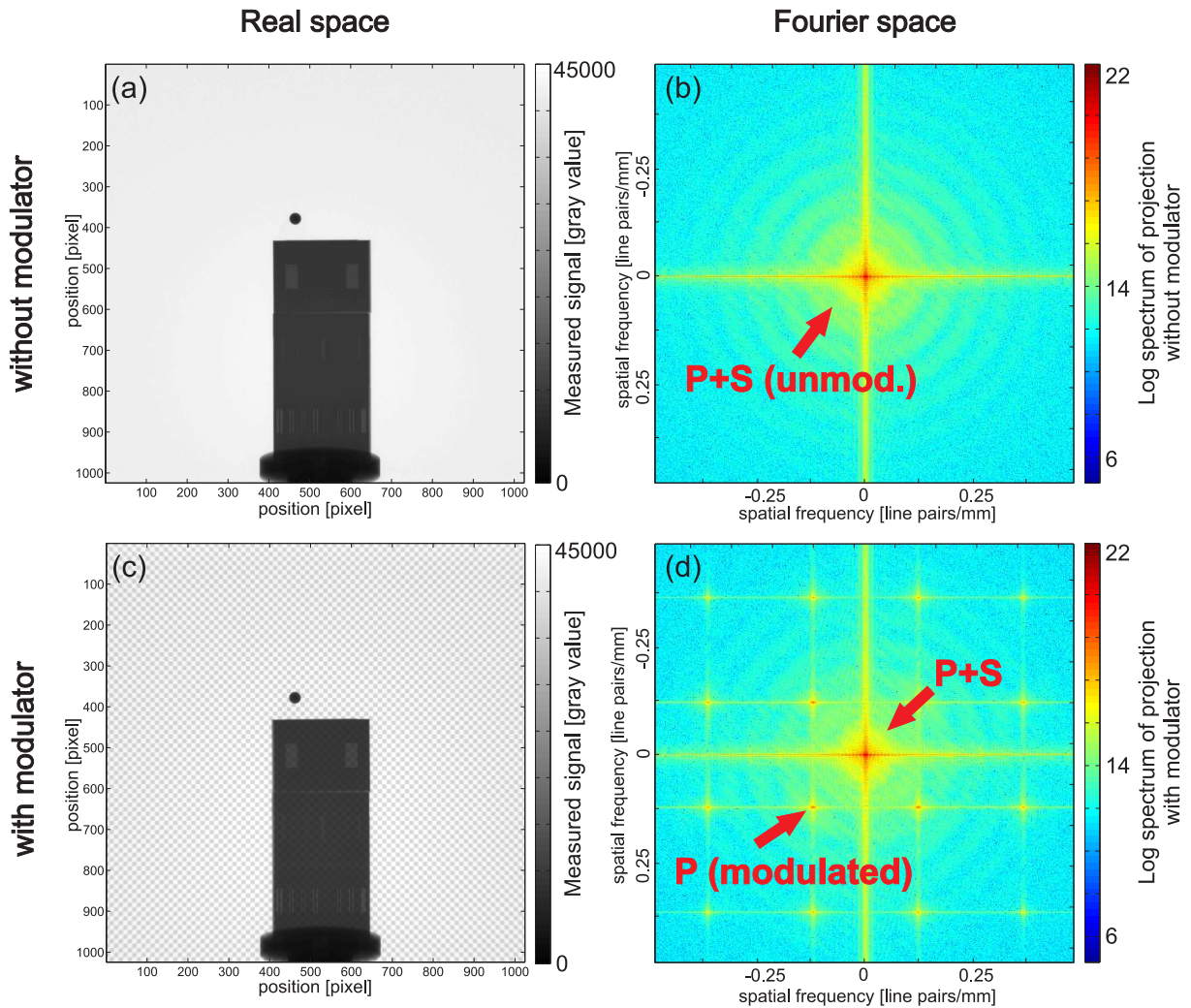
Figure 5.23: Conceptual illustration of spatial primary modulation. (a) In a normal CT projection, without primary modulator, total signals are composed of primary and scatter signals, $T = P + S$. (b) Fourier-transform of this projection yields the 2D log power spectrum where primary and scatter signals overlap, particularly near the center where scatter signals are concentrated. (c) The same CT projection as in (a), but with primary modulator placed in front of object. The spatially repetitive pattern of the primary modulator is imprinted onto the primary fluence. (d) In Fourier space, this leads to spectral copies of only primary signals around modulation frequencies f_{mod} and higher harmonics.
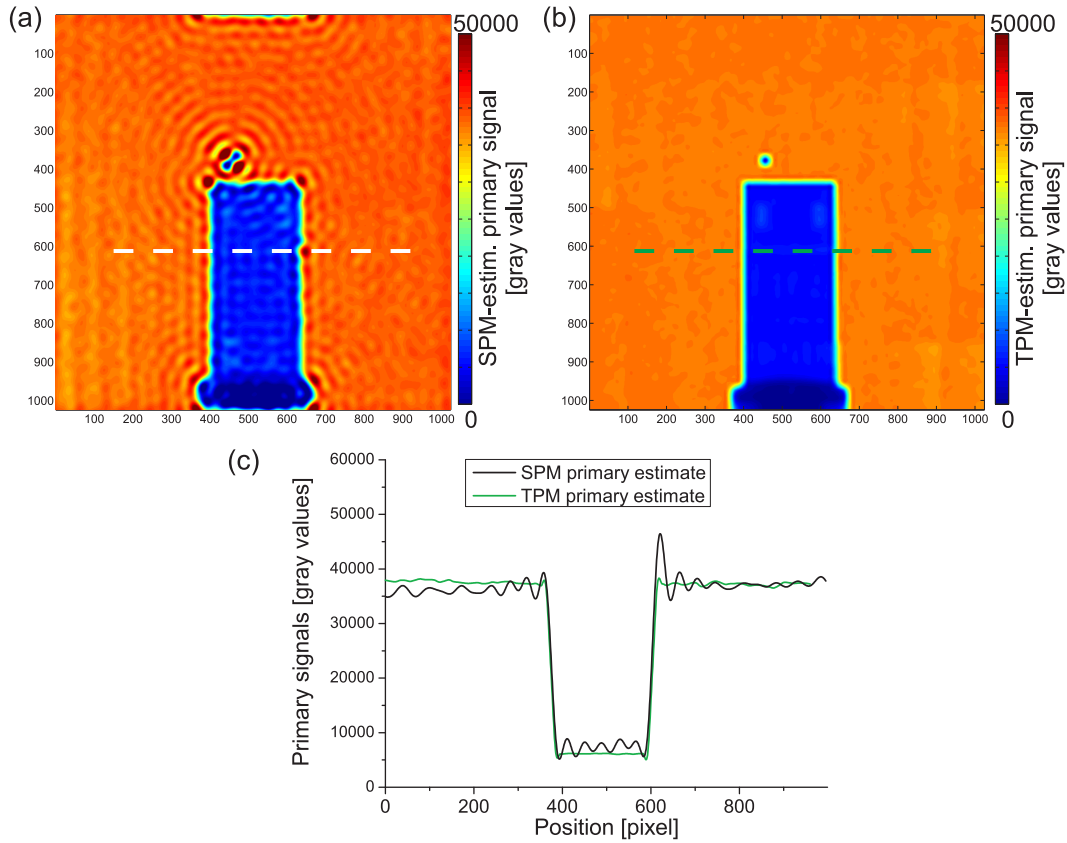
Figure 5.24: Primary estimate calculated by (a) the method of spatial primary modulation (SPM), and (b) by the method of temporal primary modulation (TPM). (c) Corresponding line profiles.

clearly exhibits ringing artifacts close to high contrast details such as sample edges, corners, etc. Ringing artifacts also spill into the object-covered projection regions, as can be deduced from the corresponding line profile in Fig. 5.24(c) (black curve). For SPM calculation of the primary estimate, we have used a modulated projection from the TPM scan (with discrete stepping primary modulator) and the procedure described in Ref. [ZBF06], except the border detection routine. This routine attempts to suppress high frequencies in the projection image by smoothing projected sample edges, etc. However, conflicts may arise in distinguishing between sample edges and edges originating from the spatial modulation pattern. The intrinsic issue of spectral overlapping remains unresolved in the SPM method.

Errors in SPM primary estimation directly affect scatter estimation. While this is a known problem with SPM and may be partly suppressed by the mentioned algorithm, the issue of spectral overlap does not exist in the TPM method at all. Therefore, the corresponding primary estimate calculated by TPM that is shown in Fig. 5.24(b) does not suffer from ringing artifacts. This represents a major advantage of TPM over SPM.

Second, in SPM, the maximum frequency which can be restored in the scatter image is given by half of the spatial frequency of the primary modulation pattern as explained above. By contrast, for TPM, the maximum frequency is theoretically only limited by the detector resolution. Practically, due to high noise levels in the experimental investi-

gations described in this chapter, we employ spatial averaging and thereby decrease the spatial resolution (downsampling). The averaging process is adaptable in terms of target downsampling size: here, we have downsampled to a frequency given by the primary modulator's spatial modulation frequency. This implies that the spatial resolution of the TPM method is greater by a factor of two (at least) than the SPM method.

Third, a stationary primary modulator as used in SPM may lead to pronounced ring artifacts due to modulation patterns still remaining in the final projections used for CT reconstruction. A possible reason for modulation patterns remaining in the projections is insufficient correction of scatter fluence and of beam-hardening effects. However, a stepping or continuous sliding modulator as it is used with TPM and the subsequent averaging over the two modulated projections leads to a balanced spatial distribution of modulation patterns such as bright and dark squares. Hereby, ring artifacts are greatly suppressed in the TPM method.

Chapter 6

Conclusion and Outlook

In this work, we have developed and studied two methods for correction of scatter-related artifacts in X-ray cone-beam CT (CBCT): the beam-hole array (BHA) technique and a different approach that is based on temporal primary modulation (TPM). When developing these methods, we have focused on industrial applications.

Motivating our work, we have demonstrated the formation of scatter artifacts in CBCT and how they impair tasks in nondestructive testing such as flaw detection and dimensional measurements (chapter 3). For basic demonstration purposes, we have added a constant scatter background to simulated, otherwise ideal CT projections. The typical appearance of scatter artifacts occurring in the reconstructed CT volume has been discussed, comprising the cupping artifact, streaks and loss of contrast.

Furthermore, we have identified and investigated different sources of scatter contributing to the total scatter background: the irradiated sample, the lab environment, and detector-internal effects. While scattered radiation from the sample is unavoidable, we have proposed basic measures to reduce the scatter contribution from the lab environment. Appropriate collimation of the beam and an elevated position for acquisition above the CT scanner base are the most fertile measures. Detector-internal scatter includes X-ray scattering at structures within the detector as well as non X-ray spread and diffusion mechanisms such as light spread in indirect-conversion detectors. We do not further distinguish between these two components but summarize them as detector-internal scatter contribution. Referring to basic investigations in chapter 3, we have determined that detector-internal scatter already amounts to 22% of the total detected signal in a fully irradiated flat-field projection with typical parameters for industrial CT (220 kVp X-ray spectrum).

In chapter 4, two experimental methods for scatter correction in CBCT have been presented and compared to each other: the beam-stop array (BSA) and its complementary, above mentioned technique, the beam-hole array (BHA). While the BSA is a long established method for scatter correction in CT, the BHA method has only been employed in a different kind of measurement (densitometric) in the medical field so far. From a theoretical point of view, both methods should yield the same scatter estimates.

However, in our experimental investigations comparing the two methods, a few prominent differences between BSA and BHA scatter measurements have been revealed. The most important difference concerns an additional scatter contribution caused by the acrylic support plate that is only – but unavoidably – present in the BSA method. Thus, in typical acquisition scenarios, the scatter-to-total ratio measured with the BSA is about 1−2%-points larger than in the corresponding BHA measurement. Based on this comparison

measurement, we conclude that the BHA represents an alternative to the BSA technique for specific application scenarios. The BHA method particularly seems to be suited for industrial series measurements. Here, an initially greater effort in measuring scatter contributions with the BHA is worthwhile since scattered radiation is reduced (by not having to insert a scattering acrylic plate) in the series measurement itself. This decreases scatter-to-primary ratios and increases signal-to-noise ratios in the CT projections.

An example for such series measurements, which we have studied, are CTs of an industrial part used in power generation technology that is to be inspected for inner cracks and dimensional tolerances. Exemplary, we have applied the BHA scatter correction method to the CT of such a specimen and successfully demonstrated elimination of scatter-related artifacts.

When we calculated the scatter images with the BHA method, we observed an important characteristic: high spatial frequencies are contained within the measured scatter images. In contrast to common expectations about the scatter distribution to be mainly of low frequency content [BS88; NTC04; ZBF06], we noticed a steep signal drop/rise in scatter image regions close to projected sample edges. Our observations are in good agreement with experimental results published by Peterzol *et al.* [PLB08]. From our former results, we conclude that detector-internal scatter causes the high frequencies that are present in the obtained scatter images.

Since both the BSA and BHA method belong to the class of blocker-based techniques, a certain amount of primary signals gets blocked within the projections, and hence, an additional scan is required in order to obtain the missing primary data. Consequentially, additional scan time and/or additional dose are necessary with BSA/BHA methods. In industrial applications, particularly the first represents a serious drawback of these two methods and was the reason for us to develop a new scatter correction method.

In chapter 5, we have presented this novel scatter correction method which is based on temporal primary modulation (TPM). With the TPM method, the scatter distribution is measured simultaneously within the normal CT scan by temporal modulation of the primary fluence while the total scatter fluence is assumed to be temporally constant. Thus, a separation is possible afterwards by demodulation of the primary signals. In addition to its time-efficiency, the TPM method – in principle – offers maximum spatial resolution in the estimation process of the scatter distribution and only is limited by the fixed resolution of the detector.

We have presented the basic concept and variants of experimental realization of TPM. Furthermore, Monte-Carlo simulations and a theoretical analysis have shown that errors in the scatter estimation will occur if scatter contributions from equi- and paraphase modulated regions within the sample are not balanced. Hence, the more the spatial frequencies of the projected sample resemble the spatial modulation frequency that is imprinted on the primary fluence, the larger the systematic error in the scatter estimation will become. In experimental practice, it is thus advisable to use a primary modulator with a very fine spatial modulation pattern.

When comparing the proposed TPM method and the established BSA technique in an experimental investigation with respect to the accuracy of measured scatter contributions, we observed the following: At sampling points where the BSA directly measures scatter signals, both methods are in good agreement, i.e. deviations are 6% or less. This

represents a verification of the novel method.

Additionally, we have successfully demonstrated the application of the proposed TPM method for correction of scatter-related artifacts in a CT of an aluminum test phantom. Scatter artifacts could be eliminated – or at least greatly suppressed. For example, contrast values of specific slits cut into the test phantom have been enhanced whereby the deviations of contrast values to ideal contrast values of a simulated CT could be reduced from about $30 - 35\%$ to 10% and even less. In nondestructive testing, this improves detectability of flaws, such as tiny cracks etc.

Here, we have proven the feasibility and accuracy of the novel TPM method. In general, this method presents the greatest potential for future developments. It offers advantages over other scatter correction methods since, without extending scan times, it directly measures scatter contributions within the specific experimental setup and ultimately provides high spatial resolutions in the scatter estimation process.

Further experiments should investigate whether the TPM scatter correction method can also be used in situations where samples consisting of multiple materials are tomographed. In this work, we have limited our considerations and investigations to single-material samples where we could apply a beam-hardening correction based on the linearization approach. The latter is theoretically exact only for single materials. However, more complex methods for beam-hardening correction including iterative schemes are available [JS78; MMS90; Hsi+00].

A further goal could be to resolve whether the TPM method can be successfully applied in medical applications also. A critical issue for medical applications lies in the fact that primary signals change temporally due to patient movement. However, if it is possible to implement TPM with the modulation of the primary fluence being on a different time scale (i.e. faster) than the change in primary signals due to patient movement, a migration of the TPM method to the medical field seems feasible.

Returning to the *gedankenexperiment* from the beginning of chapter 5, which aims at individual pixel modulation with different modulation frequencies, advanced forms of primary modulators should be investigated. For example, instead of a checkerboard pattern, multiple rows with horizontal, sinusoidal attenuation patterns featuring different spatial frequencies could be used for a line-wise varying modulation of the primary photon fluence when the primary modulator is moved horizontally (Fig. 6.1(a)). The combination of two of these line modulators – whereas the second is aligned vertically, i.e. with sinusoidal columns, and is moved vertically – would even enable a pixel-wise modulation as suggested by the gedankenexperiment (Fig. 6.1(b)). In this situation, one could infer the origins of the detected scatter contributions and use this information for advanced reconstructions incorporating spatially resolved scatter data.
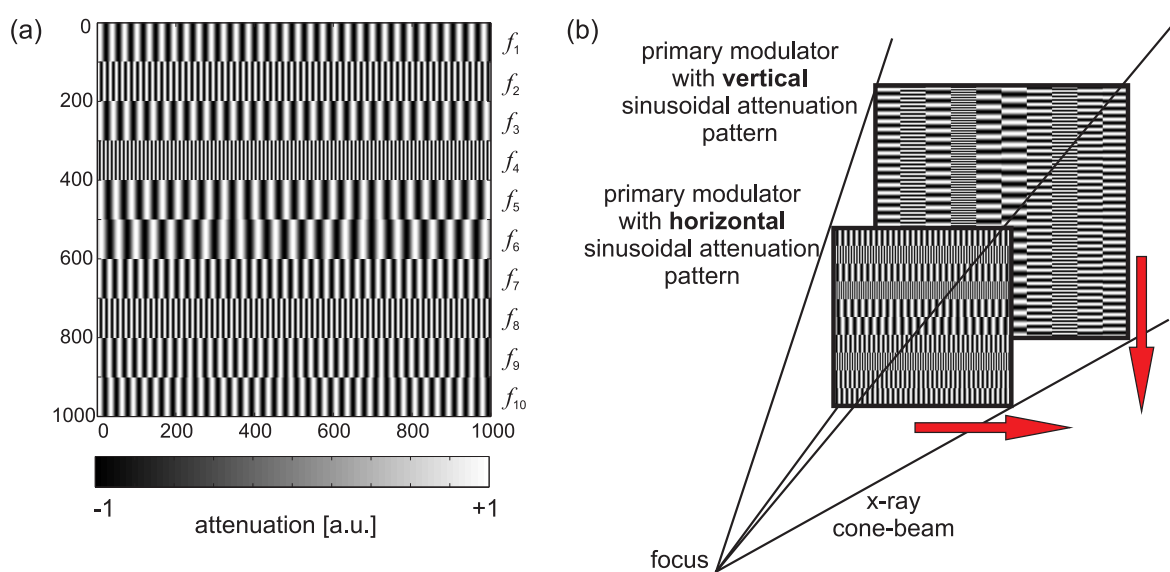
Figure 6.1: (a) Primary modulator with 10 rows of sinusoidal attenuation patterns, each row featuring a different spatial frequency f_i. This line modulator allows a line-wise varying modulation. (b) Combination of two line modulators, the first aligned and moved horizontally, the second aligned and moved vertically. The combination of two line modulators enables a pixel-wise modulation.

Appendix A

AM Coherent Demodulation for TPM

In the following, we are going to prove that

$$P_{0,\text{est.}} = \frac{4}{A \cdot N_{\text{mod}}} \sum_{j=1}^{N_{\text{mod}}} T(t_j) \cdot \cos(\omega_{\text{mod}} \cdot t_j) \tag{A.1}$$

is a correct estimation of the primary signal P_0.

As described in section 5.1, the total signal is the sum of modulated primary $P(t_j)$ and unmodulated, i.e. constant, scatter signal $S(t_j) = S = \text{const.}$:

$$\begin{aligned} T(t_j) &= P(t_j) + S(t_j) \tag{A.2} \\ &= P_0 \cdot f_{\text{mod}}(t_j) + S , \tag{A.3} \end{aligned}$$

where, in the last step, the undisturbed primary signal P_0 is modulated by the modulation function

$$f_{\text{mod}}(t_j) = 1 + \frac{A}{2} \left(\cos(\omega_{\text{mod}} \cdot t_j) - 1 \right) , \tag{A.4}$$

with ω_{mod} being the modulation frequency and A the modulation strength.

Given the total signal in Eq. (A.3), we can extract the modulated primary signal by AM coherent demodulation. Therefore, we (i) multiply the total signal with the time-dependent term of the modulation function, i.e. $\frac{A}{2} \cos(\omega_{\text{mod}} \cdot t_j)$, and (ii), we apply low-pass filtering which is realized by averaging over the N_{mod} modulated projections. Thereby,

we obtain the demodulated primary signal P_demod as

$$P_\text{demod} = \frac{1}{N_\text{mod}} \sum_{j=1}^{N_\text{mod}} T(t_j) \cdot \frac{A}{2} \cos(\omega_\text{mod} \cdot t_j) \tag{A.5}$$

$$= \frac{1}{N_\text{mod}} \sum_{j=1}^{N_\text{mod}} \left[P_0 \left(1 + \frac{A}{2} (\cos(\omega_\text{mod} \cdot t_j) - 1) \right) + S \right] \cdot \frac{A}{2} \cos(\omega_\text{mod} \cdot t_j) \tag{A.6}$$

$$= \frac{1}{N_\text{mod}} \sum_{j=1}^{N_\text{mod}} \left[P_0 \frac{A}{2} \cos(\omega_\text{mod} \cdot t_j) + P_0 \frac{A^2}{4} \cos^2(\omega_\text{mod} \cdot t_j) - \dots \right.$$
$$\left. P_0 \frac{A^2}{4} \cos(\omega_\text{mod} \cdot t_j) + S \frac{A}{2} \cos(\omega_\text{mod} \cdot t_j) \right] \tag{A.7}$$

$$= \frac{1}{N_\text{mod}} \sum_{j=1}^{N_\text{mod}} \cos(\omega_\text{mod} \cdot t_j) \left[P_0 \frac{A}{2} - P_0 \frac{A^2}{4} + S \frac{A}{2} \right] + \dots$$
$$\frac{1}{N_\text{mod}} \sum_{j=1}^{N_\text{mod}} \cos^2(\omega_\text{mod} \cdot t_j) P_0 \frac{A^2}{4} . \tag{A.8}$$

In the last equation, the first sum vanishes due to cosine oscillations, and in the second sum, we apply $\cos^2(\dots) = \frac{1}{2} + \frac{1}{2} \cos(2 \cdot \dots)$, hence:

$$P_\text{demod} = \frac{1}{N_\text{mod}} \sum_{j=1}^{N_\text{mod}} P_0 \frac{A^2}{4} \left(\frac{1}{2} + \frac{1}{2} \cos(2 \cdot \omega_\text{mod} t_j) \right) \tag{A.9}$$

$$= \frac{1}{N_\text{mod}} \sum_{j=1}^{N_\text{mod}} P_0 \frac{A^2}{8} + \frac{1}{N_\text{mod}} \sum_{j=1}^{N_\text{mod}} P_0 \frac{A^2}{8} \cos(2 \cdot \omega_\text{mod} t_j) . \tag{A.10}$$

Again, the sum over the cosine term vanishes, and we obtain

$$P_\text{demod} = \frac{1}{N_\text{mod}} \sum_{j=1}^{N_\text{mod}} P_0 \frac{A^2}{8} \tag{A.11}$$

$$= P_0 \frac{A^2}{8} . \tag{A.12}$$

Thus, the result of the demodulation process is $P_0 \frac{A^2}{8}$. We obtain the original, undisturbed primary signal P_0 by multiplication with the inverse of the prefactor. Thus, the primary estimate $P_{0,\text{est.}}$ reads as follows:

$$P_{0,\text{est.}} = \left(\frac{A^2}{8} \right)^{-1} \cdot P_\text{demod} = P_0 . \tag{A.13}$$

If we insert P_demod from Eq. (A.5) here, we obtain

$$P_{0,\text{est.}} = \frac{4}{A \cdot N_\text{mod}} \sum_{j=1}^{N_\text{mod}} T(t_j) \cdot \cos(\omega_\text{mod} \cdot t_j) \overset{\text{(A.13)}}{=} P_0 . \tag{A.14}$$

which was to be shown.

Appendix B

TPM Scatter Correction with Discrete Stepped Primary Modulator

Analogously to the experimental investigations presented in section 5.6, we have also performed TPM scatter correction with a discrete stepped primary modulator (cf. section 5.4.2). In contrast to the TPM scatter correction with continuous sliding primary modulator, here we obtain a modulation map that is nearly homogeneous (Fig. 5.16(a)). On the other hand, scanning times are also extended due to motor shifting times in between the two modulated projections.

Two scans are performed: a first scan with TPM scatter correction implemented by discrete stepping primary modulator, and the second as a normal CT scan without scatter correction. Scan parameters are given in Table 5.1. However, here frame times amount to 2 s per modulated projection. Hence, the total integration time for projections is 72 min. Due to rotation of the object and synchronization with the frame grabber, the total scan time is 104 min for the normal CT scan. In case of the TPM scan with discrete stepping primary modulator, it is 144 min since motor shifting times ($1080 \cdot 0.4\,\mathrm{s} \approx 7$ min) are added and cause, for technical reasons, even longer synchronization times.

In both scans, the tomographed sample is the test phantom specifically designed for demonstration of scatter artifacts that is described in more detail in section 5.5.1. It is positioned centrally on the rotation table, i.e. aligned with the axis of rotation.

Scatter images are calculated using the TPM method correspondingly to the procedure described in section 5.6.1. Here, we average calculated scatter signals over pixel clusters which correspond to the spatial modulation grid, i.e. with 94×94 squares in the region of interest. As discussed in section 5.4.2, the modulation map is nearly homogeneous and we can perform averaging over a larger region than in the case of the sawtooth-like modulation pattern (Fig. 5.16(b)) used in the TPM variant of the continuous sliding primary modulator. Hereby, noise is reduced in the scatter estimate.

Figure B.1 shows a comparison of TPM scatter-corrected CT slices (top row) to the corresponding slices from the uncorrected, normal CT (middle row). Line profiles as indicated in the CT slices are given in the bottom row. Note the different scatter artifacts discussed in section 3.2 within the uncorrected CT slices: streaks are marked by black and white arrows, and the cupping artifact as well as loss of contrast for slits and the central hole can be inferred from the corresponding line profiles. These artifacts are greatly suppressed in case of the TPM scatter-corrected CT (Fig. B.1(a)-(c)). The performance of the TPM scatter correction in respect to eliminating scatter artifacts is highly comparable to the results we obtain for the TPM variant with continuous sliding primary modulator,
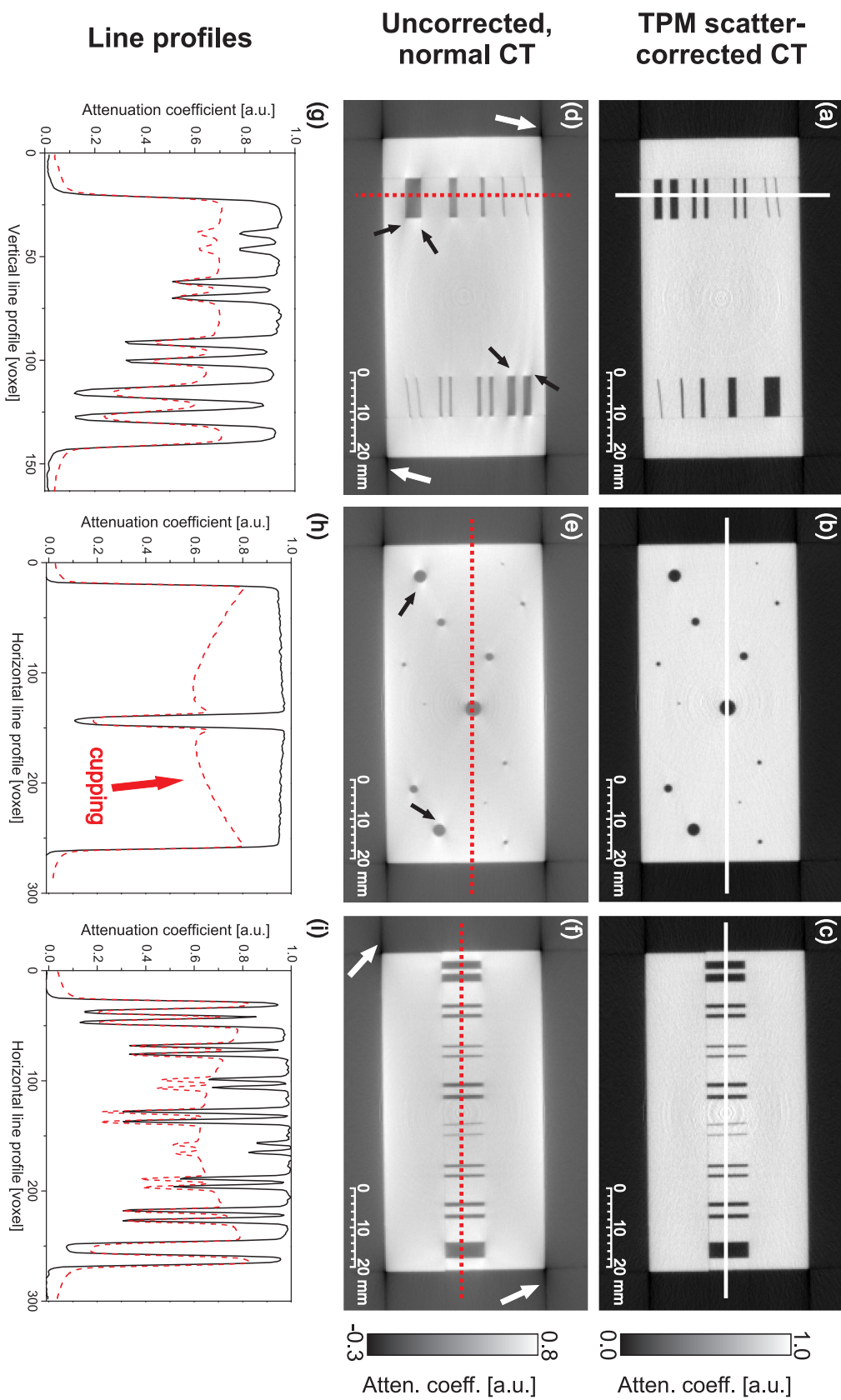
Figure B.1: (a)–(c) TPM scatter-corrected axial CT slices ('TPM variant employing a discrete stepped primary modulator'). (d)–(f) show the corresponding CT slices from a normal CT without scatter correction. (g)–(i) Corresponding line profiles. Voxel size is 335 μm. For details see text.

cf. Fig. 5.22. Thus, for a more detailed discussion and interpretation of the experimental results, refer to section 5.6.2.

Acknowledgements

Bibliography

[AM76]   R.E. Alvarez and A. Macovski. *Energy-selective reconstructions in x-ray computerised tomography.* Phys. Med. Biol. 21 (1976), 733–744.

[Ank00]   U. Ankerhold. *Catalogue of X-ray spectra and their characteristic data.* Physikalisch-Technische Bundesanstalt, Braunschweig. 2000.

[Bad03]   A. Badano. *Optical blur and collection efficiency in columnar phosphors for x-ray imaging.* Nucl. Instr. Meth. A 508 (2003), 467–479.

[Bar91]   G.T. Barnes. *Contrast and scatter in x-ray imaging.* Radiographics 11 (1991), 307–323.

[Ber+10] M.J. Berger, J.H. Hubbell, S.M. Seltzer, J. Chang, J.S. Coursey, R. Sukumar, D.S. Zucker, and K. Olsen. *XCOM: Photon Cross Sections Database.* National Institute of Standards and Technology, Gaithersburg, MD, USA. 2010. URL: http://physics.nist.gov/xcom.

[Beu00]   J. Beutel. *Handbook of medical imaging: Physics and psychophysics.* 1st edition. SPIE Press, Bellingham, 2000.

[Boo+99] J.M. Boone, J.A. Seibert, J.M. Sabol, and M. Tecotzky. *A Monte Carlo study of x-ray fluorescence in x-ray detectors.* Med. Phys. 26 (1999), 905–916.

[BS88]   J.M. Boone and J.A. Seibert. *An analytical model of the scattered radiation distribution in diagnostic radiology.* Med. Phys. 15 (1988), 721–725.

[Bub+07] A. Bub, S. Gondrom, M. Maisl, N. Uhlmann, and W. Arnold. *Image blur in a flat-panel detector due to Compton scattering at its internal mountings.* Meas. Sci. Technol. 18 (2007), 1270–1277.

[Buz08]   T.M. Buzug. *Computed tomography: from photon statistics to modern cone-beam CT.* 1st edition. Springer, Berlin, 2008.

[CB04]   A.P. Colijn and F.J. Beekman. *Accelerated simulation of cone beam X-ray scatter projections.* IEEE Trans. Med. Imaging 23 (2004), 584–590.

[CD83]   H.P. Chan and K. Doi. *The validity of Monte Carlo simulation in studies of scattered radiation in diagnostic radiology.* Phys. Med. Biol. 28 (1983), 109–129.

[CHD85]   H.P. Chan, Y. Higashida, and K. Doi. *Performance of antiscatter grids in diagnostic radiology: experimental measurements and Monte Carlo simulation studies.* Med. Phys. 12 (1985), 449–454.

[CHK97]   D.E. Cullen, J.H. Hubbell, and L. Kissel. *EPDL97: The evaluated photon data library, '97 version.* Lawrence Livermore National Laboratory, Livermore, CA, USA. 1997. URL: http://www-nds.iaea.org/epdl97/.

[CLW90]   H.P. Chan, K.L. Lam, and Y. Wu. *Studies of performance of antiscatter grids in digital radiography: effect on signal-to-noise ratio.* Med. Phys. 17 (1990), 655–664.

[Com23]   A.H. Compton. *A quantum theory of the scattering of X-rays by light elements.* Phys. Rev. 21 (1923), 483–502.

[End+01]   M. Endo, T. Tsunoo, N. Nakamori, and K. Yoshida. *Effect of scattered radiation on image noise in cone beam CT.* Med. Phys. 28 (2001), 469–474.

[Eva55]   R.D. Evans. *The atomic nucleus.* 1st edition. McGraw-Hill, New York, 1955.

[FDK84]   L.A. Feldkamp, L.C. Davis, and J.W. Kress. *Practical cone-beam algorithm.* J. Opt. Soc. Am. A 1 (1984), 612–619.

[Gao+10]   H. Gao, R. Fahrig, N.R. Bennett, M. Sun, J. Star-Lack, and L. Zhu. *Scatter correction method for x-ray CT using primary modulation: Phantom studies.* Med. Phys. 37 (2010), 934–946.

[GBH70]   R. Gordon, R. Bender, and G.T. Herman. *Algebraic Reconstruction Techniques (ART) for three-dimensional electron microscopy and X-ray photography.* J. Theor. Biol. 29 (1970), 471–481.

[GG02]   A. Greaves and M. Geso. *Measurement and modeling of x-ray scatter using lead discs in digital fluoroscopy.* In: Proc. SPIE Vol. 4682. 2002, 491–494.

[Glo82]   G.H. Glover. *Compton scatter effects in CT reconstructions.* Med. Phys. 9 (1982), 860–867.

[Gra+07]   S.A. Graham, D.J. Moseley, J.H. Siewerdsen, and D.A. Jaffray. *Compensators for dose and scatter management in cone-beam computed tomography.* Med. Phys. 34 (2007), 2691–2703.

[Gui94]   A. Guinier. *X-ray diffraction in crystals, imperfect crystals, and amorphous bodies.* Dover Publications, New York, 1994.

[GZF10]   H. Gao, L. Zhu, and R. Fahrig. *Modulator design for x-ray scatter correction using primary modulation: Material selection.* Med. Phys. 37 (2010), 4029–4037.

[Hau92]   H.G. Haubold. *Röntgenkleinwinkelstreuung an Synchrotronstrahlungsquellen.* In: Synchrotronstrahlung zur Erforschung kondensierter Materie, 23. IFF-Ferienkurs. Forschungszentrum Jülich, 1992, 29.1–29.31.

[Her79]   G.T. Herman. *Correction for beam hardening in computed tomography.* Phys. Med. Biol. 24 (1979), 81–106.

[HKG05]   M. Hoheisel, A. Korn, and J. Giersch. *Influence of backscattering on the spatial resolution of semiconductor X-ray detectors.* Nucl. Instr. Meth. A 546 (2005), 252–257.

[HKK91]   M. Honda, K. Kikuchi, and K. Komatsu. *Method for estimating the intensity of scattered radiation using a scatter generation model.* Med. Phys. 18 (1991), 219–226.

[HM98]   P. Hammersberg and M. Mangard. *Correction for beam hardening artefacts in computerised tomography.* J. X-Ray Sci. Technol. 8 (1998), 75–93.

[Hsi+00] J. Hsieh, R.C. Molthen, C.A. Dawson, and R.H. Johnson. *An iterative approach to the beam hardening correction in cone beam CT.* Med. Phys. 27 (2000), 23–29.

[Hsi03] J. Hsieh. *Computed tomography: principles, design, artifacts, and recent advances.* 1st edition. SPIE Press, Bellingham, 2003.

[Hub+75] J.H. Hubbell, W.J. Veigele, E.A. Briggs, R.T. Brown, D.T. Cromer, and R.J. Howerton. *Atomic form factors, incoherent scattering functions, and photon scattering cross sections.* J. Phys. Chem. Ref. Data 4 (1975), 471–538.

[JS78] P.M. Joseph and R.D. Spital. *A method for correcting bone induced artifacts in computed tomography scanners.* J. Comput. Assist. Tomo. 2 (1978), 100–108.

[JS82] P.M. Joseph and R.D. Spital. *The effects of scatter in x-ray computed tomography.* Med. Phys. 9 (1982), 464–472.

[JY82] P.C. Johns and M. Yaffe. *Scattered radiation in fan beam imaging systems.* Med. Phys. 9 (1982), 231–239.

[Kac37] S. Kaczmarz. *Angenäherte Auflösung von Systemen linearer Gleichungen.* Bull. Acad. Polon. Sci. Lett. A 35 (1937), 355–357.

[Kal81] W. Kalender. *Monte Carlo calculations of x-ray scatter data for diagnostic radiology.* Phys. Med. Biol. 26 (1981), 835–849.

[Kan+85] H. Kanamori, N. Nakamori, K. Inoue, and E. Takenaka. *Effects of scattered X-rays on CT images.* Phys. Med. Biol. 30 (1985), 239–249.

[Kat03] A. Katsevich. *A general scheme for constructing inversion algorithms for cone beam CT.* Int. J. Math. Math. Sci. 2003 (2003), 1305–1321.

[Kat04] A. Katsevich. *Image reconstruction for the circle and line trajectory.* Phys. Med. Biol. 49 (2004), 5059–5072.

[Kat05] A. Katsevich. *Image reconstruction for the circle-and-arc trajectory.* Phys. Med. Biol. 50 (2005), 2249–2265.

[KK07] Y. Kyriakou and W. Kalender. *Efficiency of antiscatter grids for flat-detector CT.* Phys. Med. Biol. 52 (2007), 6275–6293.

[Kno89] G.F. Knoll. *Radiation detection and measurement.* 2nd edition. John Wiley & Sons, New York, 1989.

[KPK09] Y. Kyriakou, D. Prell, and W.A. Kalender. *Ring artifact correction for high-resolution micro CT.* Phys. Med. Biol. 54 (2009), N385–N391.

[KRK06] Y. Kyriakou, T. Riedel, and W.A. Kalender. *Combining deterministic and Monte Carlo calculations for fast estimation of scatter intensities in CT.* Phys. Med. Biol. 51 (2006), 4567–4586.

[KS88] A.C. Kak and M. Slaney. *Principles of computerized tomographic imaging.* 1st edition. IEEE Press, New York, 1988.

[Mal+05]   J.S. Maltz, W.E. Blanz, D. Hristov, and A. Bani-Hashemi. *Cone beam X-ray scatter removal via image frequency modulation and filtering.* In: Conference Proceedings of the International Conference of IEEE Engineering in Medicine and Biology Society. 2005, 1854–1857.

[Mic+07]   A. Miceli, R. Thierry, A. Flisch, U. Sennhauser, F. Casali, and M. Simon. *Monte Carlo simulations of a high-resolution X-ray CT system for industrial applications.* Nucl. Instr. Meth. A 583 (2007), 313–323.

[MM98]   K.P. Maher and J.F. Malone. *Examination of aperture signals in digital radiography.* Phys. Med. Biol. 43 (1998), 609–617.

[MMS90]   J.M. Meagher, C.D. Mote, and H.B. Skinner. *CT image correction for beam hardening using simulated projection data.* IEEE Trans. Nucl. Sci. 37 (1990), 1520–1524.

[Nei92]   U. Neitzel. *Grids or air gaps for scatter reduction in digital radiography: a model calculation.* Med. Phys. 19 (1992), 475–481.

[NTC04]   R. Ning, X. Tang, and D. Conover. *X-ray scatter correction algorithm for cone beam CT imaging.* Med. Phys. 31 (2004), 1195–1202.

[OFKR99]   B. Ohnesorge, T. Flohr, and K. Klingenbeck-Regn. *Efficient object scatter correction algorithm for third and fourth generation CT scanners.* Eur. Radiol. 9 (1999), 563–569.

[PLB08]   A. Peterzol, J.M. Létang, and D. Babot. *A beam stop based correction procedure for high spatial frequency scatter in industrial cone-beam X-ray CT.* Nucl. Instr. Meth. B 266 (2008), 4042–4054.

[Pod10]   E.B. Podgoršak. *Radiation physics for medical physicists.* 2nd edition. Springer, Berlin, 2010.

[RGP11]   C. Reinhart, T. Günther, and C. Poliwoda. *VGStudio Max 2.1.* Volume Graphics GmbH, Heidelberg. 2011. URL: www.volumegraphics.com.

[SB88]   J.A. Seibert and J.M. Boone. *X-ray scatter removal by deconvolution.* Med. Phys. 15 (1988), 567–575.

[Sch+83]   D. Schaupp, M. Schumacher, F. Smend, P. Rullhusen, and J.H. Hubbell. *Small-Angle Rayleigh Scattering of Photons at High Energies: Tabulations of Relativistic HFS Modified Atomic Form Factors.* J. Phys. Chem. Ref. Data 12 (1983), 467–512.

[SF85]   J.A. Sorenson and J. Floch. *Scatter rejection by air gaps: an empirical model.* Med. Phys. 12 (1985), 308–316.

[Shm06]   Y. Shmaliy. *Continuous-time signals.* 1st edition. Springer, Dordrecht, 2006.

[Sie+04]   J.H. Siewerdsen, D.J. Moseley, B. Bakhtiar, S. Richard, and D.A. Jaffray. *The influence of antiscatter grids on soft-tissue detectability in cone-beam computed tomography with flat-panel detectors.* Med. Phys. 31 (2004), 3506–3520.

[SJ01]   J.H. Siewerdsen and D.A. Jaffray. *Cone-beam computed tomography with a flat-panel imager: magnitude and effects of x-ray scatter.* Med. Phys. 28 (2001), 220–231.

[SP04]   J. Sijbers and A. Postnov. *Reduction of ring artefacts in high resolution micro-CT reconstructions.* Phys. Med. Biol. 49 (2004), N247–N253.

[Sti93]   K. Stierstorfer. *Mocassim: A Monte Carlo scatter simulation tool.* Siemens Medical Engineering Internal Report, Erlangen. 1993.

[SV82]   L.A. Shepp and Y. Vardi. *Maximum likelihood reconstruction for emission tomography.* IEEE Trans. Med. Imaging 1 (1982), 113–122.

[Tit+09]   S. Titarenko, V. Titarenko, A. Kyrieleis, and P.J. Withers. *A ring artifact suppression algorithm based on a priori information.* Appl. Phys. Lett. 95 (2009), 071113 1–3.

[Tur01]   H. Turbell. "Cone-beam reconstruction using filtered backprojection." PhD thesis. Linköpings universitet, Sweden, 2001.

[Tuy83]   H.K. Tuy. *An inversion formula for cone-beam reconstruction.* SIAM J. Appl. Math. 43 (1983), 546–552.

[Wie07]   J. Wiegert. "Scattered radiation in cone-beam computed tomography: analysis, quantification and compensation." PhD thesis. RWTH Aachen, Germany, 2007.

[WMS10]   J. Wang, W. Mao, and T. Solberg. *Scatter correction for cone-beam computed tomography using moving blocker strips: A preliminary study.* Med. Phys. 37 (2010), 5792–5800.

[Yan+10]   H. Yan, X. Mou, S. Tang, Q. Xu, and M. Zankl. *Projection correlation based view interpolation for cone beam CT: primary fluence restoration in scatter measurement with a moving beam stop array.* Phys. Med. Biol. 55 (2010), 6353–6375.

[ZB06]   W. Zbijewski and F.J. Beekman. *Efficient Monte Carlo based scatter artifact reduction in cone-beam micro-CT.* IEEE Trans. Med. Imaging 25 (2006), 817–827.

[ZBF06]   L. Zhu, N.R. Bennett, and R. Fahrig. *Scatter correction method for x-ray CT using primary modulation: Theory and preliminary results.* IEEE Trans. Med. Imaging 25 (2006), 1573–1587.

[Zhu+09]   L. Zhu, H. Gao, N.R. Bennett, L. Xing, and R. Fahrig. *Scatter correction for x-ray conebeam CT using one-dimensional primary modulation.* In: Proc. SPIE Vol. 7258. 2009, 201–208.

[ZMM99]   Y. Zhou, T. Mathur, and S. Molloi. *Scatter and veiling glare estimation based on sampled primary intensity.* Med. Phys. 26 (1999), 2301–2310.

[ZOE03]   U. Zscherpel, K. Osterloh, and U. Ewert. *Unschärfeprobleme beim Einsatz digitaler Detektoren in der Durchstrahlungsprüfung.* DGZfP Annual Meeting. 2003. URL: http://www.ndt.net/article/dgzfp03/papers/v22/v22.htm.

[ZSF05]   L. Zhu, N. Strobel, and R. Fahrig. *X-ray scatter correction for cone-beam CT using moving blocker array.* In: Proc. SPIE Vol. 5745. 2005, 251–258.

[ZWX09]   L. Zhu, J. Wang, and L. Xing. *Noise suppression in scatter correction for cone-beam CT.* Med. Phys. 36 (2009), 741–752.

List of publications

- K. Schörner, M. Goldammer, and J. Stephan, *Comparison between beam-stop and beam-hole array scatter correction techniques for industrial X-ray cone-beam CT*, Nucl. Instr. Meth. B 269, 292–299 (2011).

- K. Schörner, M. Goldammer, J. Stephan, and P. Böni, *Scatter correction method by temporal primary modulation in X-ray CT*, IEEE Trans. Nucl. Sci. submitted (2011).

- K. Schörner, M. Goldammer, and J. Stephan, *Experimental scatter correction methods in industrial X-ray cone-beam CT*, in Proceedings 'Review of progress in quantitative nondestructive evaluation 30', San Diego, USA, AIP Conf. Proc. 1335, 485–492 (2011).

- K. Schörner, M. Goldammer, and J. Stephan, *Scatter Correction by Modulation of Primary Radiation in Industrial X-ray CT: Beam-hardening Effects and their Correction*, in Proceedings 'International Symposium on Digital Industrial Radiology and Computed Tomography 2011', Berlin, Germany (2011).

- K. Schörner, M. Goldammer, and J. Stephan, *Streustrahlenmessung und -korrektur mittels räumlicher Primärmodulation in der CT*, in Proceedings 'DGZfP Jahrestagung 2011', Bremen, Germany (2011).

- K. Schörner, M. Goldammer, and J. Stephan, *Streustrahlenmessung und -korrektur durch Beamhole-Array und Beamstop-Array*, in Proceedings 'Industrielle Computertomografie Fachtagung 2010', Wels, Austria, 235–241 (2010).

- K. Schörner and M. Goldammer, *Streustrahlenkorrektur in der Röntgen-CT und digitalen Radiografie mittels zeitlicher Modulation des Primärsignals*, patent application, DE102011006662.4, PCT/EP 2012/055202 (2011).

- K. Schörner and M. Goldammer, *Streustrahlenkorrektur in der industriellen CT mit bewegtem Primärmodulator und Beamhardeningkorrektur*, patent application, DE102011006660.8, PCT/EP 2012/055203 (2011).

- M. Goldammer, K. Schörner, and J. Stephan, *Streustrahlenkorrektur in der Computertomografie mittels eines doppelten, einem Objekt nachgeordneten Beam-Hole Arrays*, patent application, DE102010020150, WO2011/141223 (2010).